Department of Physics and Astronomy

University of Heidelberg
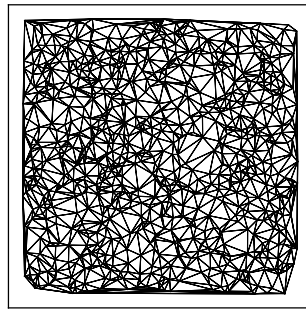
A thesis in fulfillment of the requirements
for the degree of Master of Science,

submitted by

Daniel Spitz,
born in Blaubeuren

December, 2019

Universal structures far from equilibrium in alpha complexes and persistent homology

This Master thesis, put forward by

Daniel Spitz,

has been carried out at the

Department of Physics and Astronomy
Institute for Theoretical Physics

under the supervision of
Prof. Dr. Jürgen Berges

Universelle Strukturen fern des Gleichgewichts in Alpha-Komplexen und persistenter Homologie

Inspiriert durch Techniken der topologischen Datenanalyse werden Observablen, die mittels persistenter Homologie konstruiert sind, eingeführt, um Zusammenhangs- und Clusterstrukturen in Quantenfeldtheorien zu erkennen. Als eine Prototyp-Anwendung wird das Konzept der Selbstähnlichkeit in der Umgebung von nichtthermischen Fixpunkten in Quantensystemen fern des Gleichgewichts auf diese Klasse von Observablen erweitert. Zentrales Ergebnis ist die Beobachtung eines kontinuierlichen Spektrums an Skalierungsexponenten in klassisch-statistischen Simulationen des zwei-dimensionalen, nichtrelativistischen Bose-Gases. Eine mögliche Erklärung hierfür stellt die Mischung dynamischer Komponenten in Punktwolken dar, die teils starker Wellenturbulenz und teils anomaler Vortex-Kinetik zugeordnet werden können. Skalierungsexponenten extrahiert aus persistenter Homologie sind eng verknüpft mit der Geometrie des physikalischen Systems, wie die Herleitung einer Packungsrelation zwischen selbigen darlegt. Die im Rahmen dieser Arbeit gewonnenen Ergebnisse zeigen auf, dass persistente Homologie und mit dieser verwandte Techniken vielseitige und mächtige Methoden sind, um Quantensysteme über die Sprache von Korrelationsfunktionen hinausgehend zu verstehen.

Universal structures far from equilibrium in alpha complexes and persistent homology

Inspired by topological data analysis techniques, persistent homology observables are introduced in order to geometrically detect connectivity and clustering structures in quantum field theories. Serving as a prototype application, the concept of self-similarity in the vicinity of nonthermal fixed points in far-from-equilibrium quantum systems is extended to persistent homology observables. Crucially, in classical-statistical simulations of the two-dimensional nonrelativistic Bose gas we discover a continuous scaling exponent spectrum. A possible explanation is provided in terms of mixing strong wave turbulence and anomalous vortex kinetics components in point clouds. Persistent homology scaling exponents are inherently linked to the geometry of the physical system, as the derivation of a packing relation reveals. The results given in this work demonstrate that the persistent homology machinery offers powerful and versatile methods to understand quantum systems beyond the language of correlation functions.

Contents

Chapter 1

Introduction

Since its early days, the extraordinarily powerful machinery of quantum field theory (QFT) led to exceptionally accurate physical predictions on both tiniest and largest energy scales amenable to physical experiments. A tremendous range of physical scenarios has been successfully explained using QFT, ranging from high-energy to condensed matter physics, from thermal equilibrium properties to the vivid dynamics of ultracold quantum gases or quantum fields in the early universe. Typically, quantum field-theoretic techniques are applied to observables formulated in the language of correlation functions. With the work described in this thesis we seek to commence the introduction of a novel class of observables to QFT, persistent homology observables. As a proof of principle, we focus on promoting a geometric understanding of dynamical quantum phenomena.

Ubiquitous in nature, comprehending far-from-equilibrium situations and the process of thermalization has been a topic of intense debate for decades. Focussing on quantum many-body systems, this field of research recently saw eminent scientific progress [1]. Through complex dynamical collective processes quantum many-body systems generically display an effective loss of sensitivity to details of initial states [2]. It has been demonstrated that on their path towards equilibrium these systems can show self-similar dynamics based on the existence of a nonthermal fixed point [2, 3]. Nonthermal fixed points represent nonequilibrium attractor solutions with self-similar scaling dynamics less sensitive to microscopic system parameters and initial conditions.

Owing to their universality, nonthermal fixed points provide a link between vastly different energy scales and physical systems. Both from a conceptual and a research perspective fascinating, this opens up the possibility to learn from table-top experiments with ultracold atoms aspects about the dynamics that the early universe underwent [2]. The scope of corresponding far-from-equilibrium universality classes can be surprisingly large, covering both relativistic and nonrelativistic scalars in one [4] or, in an expanding geometry, non-Abelian gauge theories and self-interacting scalar field theories in another [5, 6]. Important links between nonthermal fixed points and the dynamics of strong and

weak wave turbulence have been established, enhancing the understanding of relevant collective mechanisms [7–9]. Associated to the transport of conserved quantities such as energy, systems with a number of conserved quantities can simultaneously realize multiple nonthermal fixed points in different momentum regimes [4, 8, 10]. Focussing for instance on $O(N)$-symmetric scalar field theories, both a direct energy cascade towards the ultraviolet [11] and an inverse particle cascade towards the infrared [4, 12] have been observed in corresponding occupation number spectra.

With recent progress in handling ultracold quantum gases, the experimental study of emergent universal dynamics in isolated quantum many-body systems became feasible [13–15]. Key to the extraction of scaling properties of unitary Bose gases in far-from-equilibrium table-top experiments is that the setups designed over the past years offer particularly clean settings and can be well isolated from the environment.

Thus far, in far-from-equilibrium studies two-point correlation functions have been of primary research interest [2, 12, 16]. In recent years, additionally, there has been a growing interest in studying fourth- and even higher-order correlation functions in nonequilibrium situations [15, 17–21], encompassing evidence for universal behavior of these. Outpacing this trend via fully global observables, we extend the notion of universality far from equilibrium to persistent homology observables in order to provide a prototype application.

Emanating from algebraic topology and Morse theory, the applied mathematics branch of topological data analysis has gained considerable attention over the past two decades, accompanied by far-reaching theoretical and computational developments [22, 23]. Using tools from abstract algebra, algebraic topology offers powerful and versatile methods to globally study the structure of topological spaces by means of homology groups. Derived from the latter, quantities such as Betti numbers prominently appear in this context [24]. Resolving homological structure on different scales, hierarchically, in topological data analysis an adaptation of the notion of homology called persistent homology arose [25–27]. Notably, persistent homology makes a multi-scale description of topological structure contained in point cloud data possible. To accomplish this, simplicial complexes such as so-called Čech complexes, Vietoris-Rips complexes or alpha complexes, which are also known as alpha shapes [28, 29], are regularly employed.

Besides mathematical investigations, the field of topological data analysis applications to the natural sciences turned very vivid in recent years. Physical studies include, inter alia, applications to astrophysics and cosmology [30–33], to physical chemistry [34], to amorphous materials [35], to quantum algorithms [36–40] and to the theory of quantum phase space [41]. We will exploit the multi-scale topological information encoded in a family of alpha complexes and in associated persistent homology groups in order to rediscover self-similar scaling properties in position space variables.

Serving as a numerical testbed, we apply persistent homology techniques to the dy-

namics of the single-component nonrelativistic Bose gas in two spatial dimensions, described by the time-dependent Gross-Pitaevskii equation. The latter exhibits a rich phenomenology far from equilibrium, including various nonthermal fixed points associated to the effects of weak, strong and superfluid turbulence [42–44]. Focussing on the nonperturbative strong wave turbulence regime, a vertex-resummed two particle-irreducible expansion scheme has been successfully employed to obtain analytical predictions for relevant scaling exponents [4, 45]. The existence of corresponding nonthermal fixed points has been confirmed by means of numerical lattice simulations [46]. In addition, the infrared nonthermal fixed point can be dominated by vorticial excitations interacting anomalously with each other via 3-vortex interactions [46, 47], that is, altering the universal scaling behavior. It has been conjectured that the anomalous vortex dynamics is associated to the formation of so-called Onsager vortex clusters out of equilibrium via evaporative heating [48, 49].

In the present work we for the first time apply persistent homology in a quantum field-theoretic framework, focussing on the regime of validity of the classical-statistical approximation. Guided by numerical results for the two-dimensional Bose gas, we reveal that far from equilibrium persistent homology observables can show self-similar scaling characteristic for observables in the vicinity of a nonthermal fixed point. Astonishingly, a continuous spectrum of scaling exponents appears, depending on a filtration parameter to construct point clouds. We conjecture that the existence of such a scaling exponent spectrum indicates scaling species mixing, in our case between the strong wave turbulence and the anomalous vortex kinetics nonthermal fixed points present in the infrared of the particular Bose gas. The analysis is supplemented by a thorough investigation of accompanying subtleties of the chosen persistent homology approach such as amplitude redistribution-induced exponent shifts.

On the theoretical side, we define persistent homology observables in the classical-statistical framework. We introduce the notion of a persistence pair distribution and its statistical asymptotics in order to infer self-similar behavior of the latter. We reveal that the appearing scaling exponents probe the geometry at hand, as indicated by a packing relation derived in this work.

This thesis is structured as follows. Chapter 2 provides in reasonable depth an introduction to established notions of universal structures which appear in far-from-equilibrium quantum systems, in particular in the nonrelativistic Bose gas. This includes a description of the classical-statistical approximation and of the arising topological defect structures.

Focussing on the approach employed in the present work, in Chapter 3 we introduce point clouds, alpha complexes, persistent homology groups and the persistence diagram. In addition, we discuss known stability results for the family of persistent homology

groups and define functional summaries, which describe properties of persistence diagrams in a statistically well-behaving fashion and which we later put at the center of our embedding of persistent homology into the field-theoretic setting.

In Chapter 4 we provide information on how to numerically compute persistent homology groups, including a description of two example point processes to generate point clouds, corresponding numerical results and a discussion of the indications of relevant properties in persistence diagrams and derived quantities.

Then, in Chapter 5 we carry out the construction of persistent homology observables in the classical-statistical framework. Moreover, we introduce the asymptotic persistence pair distribution and related geometric quantities, leading to a thorough theoretical investigation of manifestations of a corresponding self-similar scaling ansatz. In particular, we derive a packing relation between the occurring scaling exponents both heuristically and put on mathematical grounds.

With the Bose gas simulations at hand, in Chapter 6 we rediscover self-similarity far from equilibrium in persistent homology observables. Crucially, this exploration culminates in the existence of a scaling exponent spectrum. We provide a possible route of explanation by means of scaling species mixing in point clouds. Additionally, we describe subtleties of our approach such as amplitude redistribution-induced exponent shifts.

Exceeding these results, in Chapter 7 we preliminarily discuss further persistent homology approaches such as the construction of point clouds as amplitude interlevel sets and relative homology groups, tailored to provide further evidence for the scaling species mixing conjecture.

Finally, in Chapter 8 we summarize, draw conclusions and issue an extensive outlook, providing proposals for various future research paths possibly worth to follow.

Throughout this thesis we use units in which $\hbar = c = k_B = 1$.

If appropriate, in this thesis argumentations are provided in mathematical language.

Chapter 2

Revisiting universal dynamics in the Bose gas

In recent years, the field of quantum dynamics far from equilibrium saw extensive progress, both theoretically and experimentally. In this realm, universal phenomena based on the existence of nonthermal fixed points, conjectured to emerge generically far from equilibrium and forming a particularly interesting and accessible phenomenon, have gained considerable attention. For these reasons, as a prototype application of persistent homology in QFT we consider the nonequilibrium QFT universal behavior.

In Sec. 2.1 we begin with a more general introduction to the notion of universality far from equilibrium. The nonrelativistic Bose gas serves as our prototype model for the persistent homology analysis undertaken in later chapters, fundamental physical phenomena of which we describe hereafter in Sec. 2.2. Often, such phenomena are numerically investigated in the classical-statistical regime as described in Sec. 2.3, allowing for a classical-statistical treatment. Correlation functions, in particular the occupation number spectrum, provide clear indications for nonequilibrium phenomena. Finally, in Sec. 2.4 we discuss known universal results for the infrared and the ultraviolet cascades which appear in the model's dynamics.

2.1   Universality far from equilibrium

Focussing on isolated quantum systems, their dynamics is governed by unitary time evolution. Additionally, they offer the possibility to study fundamental aspects of quantum statistical mechanics, such as nonequilibrium instabilities at early times and late-time thermalization from first principles.

Thermal equilibrium is characterized by a few conserved quantities only and independent of its history in time. Thus, any evolution towards thermal equilibrium that starts, initially, from a nonequilibrium state, requires an effective loss of details of the initial
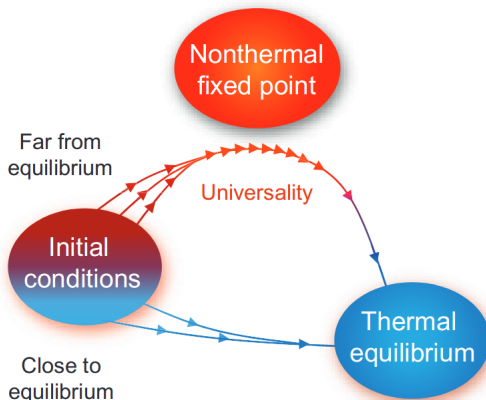
Figure 2.1: Schematic evolution towards thermal equilibrium. Reprinted from Ref. [2].

conditions at correspondingly long times. In fact, already at comparably early times an effective partial memory loss can be observed. An intriguing physical situation occurring in this context is that of self-similar scaling, which amounts to an enormous reduction of the sensitivity to details of the underlying theory and initial conditions. Based on the existence of nonthermal fixed points, the time evolution in a self-similar regime is described in terms of a few universal scaling exponents and scaling functions, similar in spirit to the notion of thermal fixed points which describe classes of thermal equilibrium systems.

Schematically, in Fig. 2.1 generic time evolution situations are displayed. While systems which, initially, are close to equilibrium directly approach thermal equilibrium in an approximate sense, far-from-equilibrium quantum systems generically show a universal, self-similar interlude including a critical slowing-down before thermalizing.

For example, in N-component relativistic scalar field theories both a direct energy cascade towards the ultraviolet [11] and an inverse cascade in occupation numbers towards the infrared [4] have been observed. This is indicated schematically in Fig. 2.2, where a typical distribution function $f(t, \mathbf{p})$ near a nonthermal fixed point is displayed for two subsequent times $t_1 < t_2$. Different momentum regimes are distinguished by means of their occupancies, $f(t, \mathbf{p})$, in terms of a small parameter $\lambda \ll 1$, which we later identify to correspond to the interaction strength or 'diluteness' of the system. The inverse cascade associated to particle number transport towards the infrared via strong wave turbulence occurs in the highly occupied regime, $f(t, \mathbf{p}) \gtrsim 1/\lambda$ [8, 50]. It is accompanied by Bose condensation far from equilibrium. Simultaneously to particles being transported to lower momenta, energy is transported in a direct cascade towards higher momenta via weak wave turbulence, leading to a direct cascade [8]. This occurs in the range $1/\lambda \gg f(t, \mathbf{p}) \gg 1$. The direct cascade evolves until a high-momentum scale is reached, where the characteristic mode occupancy becomes of the order of the 'quantum-half'.
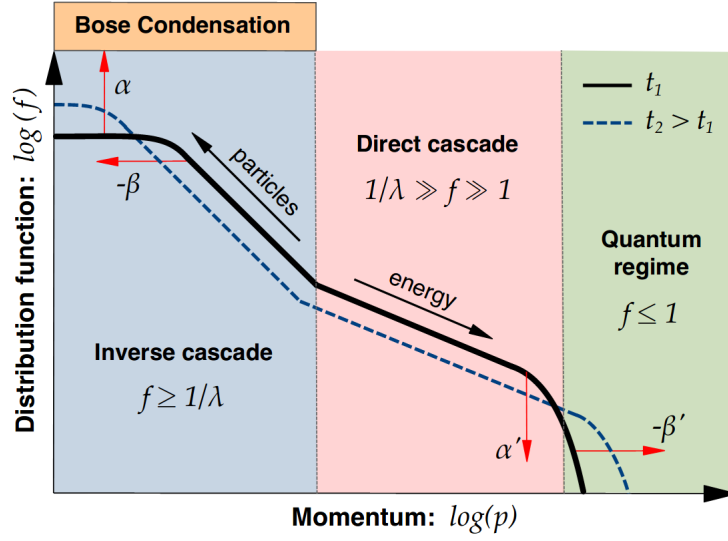
Figure 2.2: Schematic evolution towards thermal equilibrium. Reprinted from Ref. [4].

Both the inverse and the direct cascade exhibit a self-similarly scaling evolution in time in corresponding characteristic momentum regimes. To this end, for isotropic systems the distribution function obeys

$$f(t, \mathbf{p}) = t^\alpha f_S(\xi \equiv t^\beta |\mathbf{p}|) \tag{2.1}$$

within a scaling regime. The same such behavior can appear for completely different initial conditions [51]. It corresponds to a drastic reduction of dynamical degrees of freedom. In such a scaling form, the scaling exponents α and β, as well as the overall form of the nonthermal fixed point distribution $f_S(\xi)$ are universal, meaning that all models in the same universality class can be related by a multiplicative rescaling of t and $\mathbf{p}$. Any system- or initial condition-dependent property of the distribution function is contained in two nonuniversal amplitudes denoted A and B, which may be defined as

$$f_S(\xi = B) = A, \qquad \frac{df_S}{d\xi}\bigg|_{\xi=B} = -\frac{2A}{B}, \tag{2.2}$$

such that A characterizes the amplitude of the scaling function at momentum $\xi = B$, at which occupation numbers receive dominant contributions.

We can use α/β to learn about which conserved quantity is transported across momentum scales in the inertial regime in which a certain nonthermal fixed point manifests itself. From particle number conservation we can, for example, easily deduce $\alpha = d\beta$ in

a d-dimensional system. For this we compute

$$n = \int \frac{d^d\mathbf{p}}{(2\pi)^d} f(t, \mathbf{p}) = t^{\alpha - d\beta} \int \frac{d^d\mathbf{q}}{(2\pi)^d} f_S(|\mathbf{q}|). \tag{2.3}$$

Indeed, requiring that n is time-independent, we find $\alpha = d\beta$. Assuming that the dispersion scales with a dynamic exponent z as

$$\omega(\mathbf{p}) = s^{-z}\omega(s\mathbf{p}), \tag{2.4}$$

the energy can be computed as

$$\epsilon = \int \frac{d^d\mathbf{p}}{(2\pi)^d} \omega(\mathbf{p}) f(t, \mathbf{p}) = t^{\alpha - \beta(d+z)} \int \frac{d^d\mathbf{q}}{(2\pi)^d} \omega(\mathbf{q}) f_S(|\mathbf{q}|). \tag{2.5}$$

Thus, energy conservation, on the other hand, requires $\alpha = \beta(d + z)$.

We mentioned already that different cascades and correspondingly different universal dynamical behavior can appear in different inertial ranges. While particles are transported towards lower momenta in the infrared, energy is transported towards higher momenta in the ultraviolet. The corresponding nonthermal fixed points, in whose vicinity the system resides for relatively long times, are different, as indicated by different scaling exponents α and β as well as a different scaling function, $f_S(\xi)$. This includes the possibility that two models can display the same universal behavior in the infrared, while having completely different behavior in the ultraviolet. This has been observed for relativistic and nonrelativistic scalar field theories [4].

2.2 The nonrelativistic Bose gas

The prototype physical model of interest to us is the two-dimensional Bose gas, to which persistent homology techniques will be applied. Described by the time-dependent Gross-Pitaevskii equation, it exhibits a rich phenomenology, in thermal equilibrium including a Berezinskii-Kosterlitz-Thouless transition [52] and the formation of negative-temperature vortex cluster states [48]. On universal aspects far from equilibrium we will elaborate in Sec. 2.4 in more detail.

First discussing the Gross-Pitaevskii equation, we deduce from it the corresponding spectrum of elementary excitations. We find clear evidence for sound waves propagating through the condensate. Subsequently, we show that vortices exist in two spatial dimensions and go into detail in their structure. The discussion relies mainly on material presented in Ref. [53], though adapted for general dimension d, if not specified differently.

2.2.1   The Gross-Pitaevskii equation

In an ultracold Bose gas, the effective interaction between two particles at low energies is a constant in their momentum space representation, $U_0 = 4\pi a/m$, a being the s-wave scattering length, m specifying the mass. In position space, this corresponds to a contact interaction $U_0\delta(\mathbf{x} - \mathbf{x}')$, $\mathbf{x}$ and $\mathbf{x}'$ being the positions of the two particles. The effective Hamiltonian for N particles may thus be written as

$$H = \sum_{i=1}^{N} \left(\frac{\mathbf{p}_i^2}{2m} + V(\mathbf{x}_i) \right) + U_0 \sum_{i<j} \delta(\mathbf{x}_i - \mathbf{x}_j), \tag{2.6}$$

the $\mathbf{x}_i$ specifying positions of the N particles. Here, $V(\mathbf{x})$ is the external potential.

In the fully condensed state all bosons are in the same single-particle state, $\phi(\mathbf{x})$, such that the full wave function of the system reads

$$\Psi(\mathbf{x}_1, \ldots, \mathbf{x}_N) = \prod_{i=1}^{N} \phi(\mathbf{x}_i). \tag{2.7}$$

Inserting into Eq. (2.6), the energy of this state reads

$$E[\Psi] = N \int d^d\mathbf{x} \left[\frac{1}{2m} |\nabla\phi(\mathbf{x})|^2 + V(\mathbf{x}) |\phi(\mathbf{x})|^2 + \frac{(N-1)}{2} U_0 |\phi(\mathbf{x})|^4 \right]. \tag{2.8}$$

Introducing the wave function of the condensed state as

$$\psi(\mathbf{x}) = \sqrt{N}\phi(\mathbf{x}), \tag{2.9}$$

we find the total number of particles as

$$N = \int d^d\mathbf{x} \, |\psi(\mathbf{x})|^2 \tag{2.10}$$

and the energy of the system reads upon neglecting terms of order $1/N$

$$E[\psi] = \int d^d\mathbf{x} \left[\frac{1}{2m} |\nabla\psi(\mathbf{x})|^2 + V(\mathbf{x}) |\psi(\mathbf{x})|^2 + \frac{U_0}{2} |\psi(\mathbf{x})|^4 \right]. \tag{2.11}$$

The wave function ψ is subject to an overall constraint in the form of Eq. (2.10). In looking for the optimal ψ with respect to energy minimization, Lagrange multipliers may account for this. To this end, the optimal ψ fulfills the equation $\delta E - \mu \, \delta N = 0$, the chemical potential μ acting as an appropriate Lagrange multiplier here. This is equivalent to minimizing $E - \mu N$ at fixed μ. Minimization with respect to $\psi^*(\mathbf{x})$, for example, results

in

$$\left[-\frac{\nabla^2}{2m} + V(\mathbf{x}) + U_0\,|\psi(\mathbf{x})|^2\right]\psi(\mathbf{x}) = \mu\psi(\mathbf{x}). \tag{2.12}$$

This is the *time-independent Gross-Pitaevskii equation*, describing the equilibrium structure of a condensate. The non-linear term $U_0\,|\psi(\mathbf{x})|^2$ takes into account the mean field produced by the other bosons.

To render Eq. (2.10) time-dependent, we generalize it by means of replacing the chemical potential term by a temporal derivative term,

$$\left[-\frac{\nabla^2}{2m} + V(\mathbf{x}) + U_0\,|\psi(t,\mathbf{x})|^2\right]\psi(t,\mathbf{x}) = i\partial_t\psi(t,\mathbf{x}). \tag{2.13}$$

This is the *time-dependent Gross-Pitaevskii equation*. Under stationarity conditions, solutions $\psi(t,\mathbf{x})$ evolve in time as $\exp(-i\mu t)$, in accordance with its time-independent variant [53].

2.2.2   The elementary excitation spectrum

In order to study the excitation spectrum of the time-dependent Gross-Pitaevskii equation, Eq. (2.13), we linearize it, denoting the change in ψ by $\delta\psi$. This way we obtain

$$\left[-\frac{\nabla^2}{2m} + V(\mathbf{x}) + 2U_0\,|\psi(t,\mathbf{x})|^2\right]\delta\psi(t,\mathbf{x}) + U_0\,\psi(t,\mathbf{x})^2\,\delta\psi^*(t,\mathbf{x}) = i\partial_t\,\delta\psi(t,\mathbf{x}), \tag{2.14}$$

and

$$\left[-\frac{\nabla^2}{2m} + V(\mathbf{x}) + 2U_0\,|\psi(t,\mathbf{x})|^2\right]\delta\psi^*(t,\mathbf{x}) + U_0\,\psi^*(t,\mathbf{x})^2\,\delta\psi(t,\mathbf{x}) = -i\partial_t\,\delta\psi^*(t,\mathbf{x}). \tag{2.15}$$

Here, $\psi(t,\mathbf{x})$ is understood to be the condensate wave function in the unperturbed state, which we may write as $\psi(t,\mathbf{x}) = \sqrt{n(\mathbf{x})}\exp(-i\mu t)$, $n(\mathbf{x})$ being the equilibrium density of particles and μ being the chemical potential of the unperturbed system. We look for solutions to this set of equations which are periodic in time, apart from the overall phase factor $\exp(-i\mu t)$ present in the unperturbed state. To this end, we look for solutions

$$\delta\psi(t,\mathbf{x}) = e^{-i\mu t}\big(u(\mathbf{x})e^{-i\omega t} - v^*(\mathbf{x})e^{i\omega t}\big), \tag{2.16}$$

u and v being functions to be determined. Inserting this ansatz into Eqs. (2.14) and (2.15), we find the *Bogoliubov equations*,

$$\left[-\frac{\nabla^2}{2m} + V(\mathbf{x}) + 2\,U_0 n(\mathbf{x}) - \mu - \omega\right]u(\mathbf{x}) - U_0 n(\mathbf{x})\,v(\mathbf{x}) = 0, \tag{2.17}$$

and

$$\left[-\frac{\nabla^2}{2m} + V(\mathbf{x}) + 2\,U_0 n(\mathbf{x}) - \mu + \omega\right] v(\mathbf{x}) - U_0 n(\mathbf{x})\,u(\mathbf{x}) = 0. \qquad (2.18)$$

We apply this formalism to the uniform Bose gas, $V(\mathbf{x}) = 0$. By translational invariance, solutions are required to be of the form

$$u(\mathbf{x}) = u_q \frac{e^{i\mathbf{q}\mathbf{x}}}{\sqrt{V}}, \qquad v(\mathbf{x}) = v_q \frac{e^{i\mathbf{q}\mathbf{x}}}{\sqrt{V}}, \qquad (2.19)$$

V being the system's volume. The chemical potential of the system being given by $U_0\,n$, we obtain

$$\left[\frac{\mathbf{q}^2}{2m} + U_0\,n - \omega\right] u_q - U_0\,n\,v_q = 0, \qquad \left[\frac{\mathbf{q}^2}{2m} + U_0\,n + \omega\right] v_q - U_0\,n\,u_q = 0. \qquad (2.20)$$

These equations only have solutions u_q, v_q, if the determinant of the matrix of corresponding coefficients has zero-determinant, that is,

$$(\epsilon_{\mathbf{q}}^0 + U_0\,n + \omega)(\epsilon_{\mathbf{q}}^0 + U_0\,n - \omega) - U_0^2 n^2 = 0, \qquad (2.21)$$

with $\epsilon_{\mathbf{q}}^0 = \mathbf{q}^2/2m$. From this equation we obtain the dispersion relation

$$\omega(\mathbf{q}) = \sqrt{\epsilon_{\mathbf{q}}^0(\epsilon_{\mathbf{q}}^0 + 2\,U_0\,n)}. \qquad (2.22)$$

This spectrum was first derived by Bogoliubov from a microscopic theory.

In the following brief discussion of this dispersion relation we restrict to the positive branch of the square root. For small $|\mathbf{q}|$, ω is a linear function in $|\mathbf{q}|$: $\omega \simeq s|\mathbf{q}|$ with $s = \sqrt{U_0\,n/m}$. In the deep infrared, the spectrum is thus sound-like, with the sound wave velocity being s. This provides the key to superfluid behavior in ultracold Bose gases. At short wavelengths, the leading contributions to the spectrum are $\omega \simeq \epsilon_{\mathbf{q}}^0 + U_0\,n$, corresponding to the free-particle spectrum with a mean-field contribution added.

The transition between the linear dispersion and the quadratic one occurs when the kinetic energy, $\epsilon_{\mathbf{q}}^0$, becomes large compared to the potential energy of a particle, $U_0\,n$. This happens at a wave number $\sim \sqrt{2\,m\,n\,U_0}$, which is the inverse of the coherence length, ξ. The latter, in addition, is related to the sound velocity via $\xi = m\,s/\sqrt{2}$. On length scales longer than ξ, atoms in the Bose gas move collectively, while on shorted length scales they behave as free particles.

2.2.3   Vortices

The previous derivation of the nature of elementary excitations described by the Gross-Pitaevskii equation heavily relied upon the linearization process and smallness of corre-

sponding 'motions'. However, the time-dependent Gross-Pitaevskii equation has exactly known analytical solutions also in the non-linear regime, which have the form of solitary waves, solitons in brevity, which are localized disturbances that propagate without changing their shape. The latter is due to the effects of non-linearity compensating those of dispersion.

Let us investigate the structure of a single such vortex, following the lines of reasoning of Ref. [53]. We restrict to the case of two spatial dimensions, $d = 2$, and assume that the wave function varies as $e^{il\varphi}$. In polar coordinates we may write

$$\psi(\mathbf{x}) = f(r)e^{il\varphi}, \tag{2.23}$$

f being real. Inserting this ansatz into the time-independent Gross-Pitaevskii equation, Eq. (2.12), we obtain

$$-\frac{1}{2m}\frac{1}{r}\frac{d}{dr}\left(r\frac{df}{dr}\right) + \frac{1}{2mr^2}l^2f + V(r)f + U_0f^3 = \mu f. \tag{2.24}$$

We consider an infinite medium with a uniform potential taken to be zero, that is, $V(r) = 0$. At a large distance from the vortex center at $r = 0$, the radial derivative term and the centrifugal barrier term $\propto 1/r^2$ become subdominant, such that the magnitude of the condensate wave function becomes $f = f_0 \equiv \sqrt{\mu/U_0}$. Close to the center the derivative and centrifugal terms dominate and the solution scales as r, as it does for a free particle with unit angular momentum in two dimensions. A crossover distance from the vortex center between the two behavior regimes exists, which is of the order of the coherence length in matter, ξ, far from the center,

$$\frac{1}{2m\xi^2} = nU_0 = \mu, \tag{2.25}$$

$n = f_0^2$ being the density far from the vortex. We introduce the variables $x = r/\xi$ and $\chi = f/f_0$. To obtain the precise radial shape of the vortex, one may thus solve the following equation numerically,

$$-\frac{1}{x}\frac{d}{dx}\left(x\frac{d\chi}{dx}\right) + \frac{\chi}{x^2} + \chi^3 - \chi = 0. \tag{2.26}$$

The energy content of a single vortex can be approximated by subtracting the energy of a system without a vortex from the energy of a system with a vortex, both taken within a circle of radius $R \gg \xi$. The resulting estimate for the energy of a vortex reads

$$E_v \approx l^2\pi\frac{n}{m}\ln\left(\frac{R}{\xi}\right), \tag{2.27}$$

which has been confirmed approximately by means of numerical solutions. In particular, it scales with the square of the winding number l, which indicates that the system will actually prefer to be in a state with several well-separated vortices with $l = 1$ instead of one highly charged vortex. Additionally, we notice that in a vortex the energy is stored highly nonlocally, spreading throughout the gases' entire volume.

2.3 Computing nonrelativistic Bose gas dynamics

This section discusses crucial aspects of numerical simulations of the nonrelativistic Bose gas dynamics. Beginning with an introduction to the most important correlation function, the distribution function, we move on to introduce an important set of parameters, in order to conclude this section with discussing the classical-statistical approximation, making numerical simulations feasible in the first place.

2.3.1 Correlation functions and occupation numbers

Typically, in quantum field theories one is interested in the behavior of correlation functions, most generally of the type

$$\langle \mathcal{O}_1(x_1)\mathcal{O}_2(x_2)\cdots\mathcal{O}_n(x_n)\rangle, \tag{2.28}$$

the $\mathcal{O}_i$ being operator-valued distributions, or simply quantum field-theoretical operators, evaluated in this expression at space-time positions $x_1, \ldots, x_n$. Given an initial density matrix ϱ_0 and the operators in the Heisenberg picture, the expectation value is computed as

$$\langle \mathcal{O}_1(x_1)\mathcal{O}_2(x_2)\cdots\mathcal{O}_n(x_n)\rangle := \mathrm{Tr}(\varrho_0\,\mathcal{O}_1(x_1)\mathcal{O}_2(x_2)\cdots\mathcal{O}_n(x_n)). \tag{2.29}$$

Physically, time-ordered correlation functions are among the most usual ones in corresponding investigations, encoding a tremendous variety of physical quantities.

In this work, we will deviate from this path, studying persistent homology observables which by construction do not depend on a fixed number of space-time positions. For comparison reasons, we nevertheless investigate the time-dependent occupation number spectrum, $f(t, \mathbf{p})$, and its scaling properties. Let ψ be a complex-valued bosonic quantum field operator. As in Ref. [4] we first define the statistical two-point correlation function

$$F(t, t', \mathbf{x} - \mathbf{x}') = \frac{1}{2}\langle \psi(t, \mathbf{x})\psi^*(t', \mathbf{x}') + \psi(t', \mathbf{x}')\psi^*(t, \mathbf{x})\rangle. \tag{2.30}$$

Generally speaking, the statistical two-point correlation function encodes the occupation of given quantum states with (quasi-) particles. Subsequently, in d spatial dimensions we

define

$$f(t, \mathbf{p}) + (2\pi)^d \delta^{(d)}(\mathbf{p}) \, |\psi_0|^2(t) \equiv \int d^d\mathbf{x} \, e^{-i\mathbf{p}\mathbf{x}} F(t, t, \mathbf{x}). \tag{2.31}$$

Due to spatial isotropy of expectation values in the system, the distribution function or, equivalently termed, the occupation number spectrum actually only depends on the modulus of momenta, $f(t, |\mathbf{p}|)$. The term $\propto |\psi_0|^2(t)$ represents the condensate contribution to the spectrum, if present in the system at a given time t.

For completeness, the spectral function is defined in position space as follows,

$$\rho(x, y) := i\langle[\psi(x), \psi^*(y)]\rangle. \tag{2.32}$$

Assuming homogeneity and Fourier-transforming this expression, subsequently, yields

$$\tilde{\rho}(p^0, \mathbf{p}) = \int dt \, d^d\mathbf{x} \, e^{ip^0 t - i\mathbf{p}\mathbf{x}} \, \rho((t, \mathbf{x}), 0). \tag{2.33}$$

2.3.2 Parametrical considerations

From the s-wave scattering length, a, of a Bose gas and its density, n, we define a diluteness parameter [4],

$$\zeta = \sqrt{na^3}. \tag{2.34}$$

A characteristic coherence length may be defined inversely via the momentum scale

$$Q = \sqrt{16\pi a n}. \tag{2.35}$$

The average density, $n(t)$, can be computed from the distribution function, $f(|\mathbf{p}|)$, $\mathbf{p}$ being the momentum, via

$$n(t) = \int \frac{d^d\mathbf{p}}{(2\pi)^d} f(t, |\mathbf{p}|). \tag{2.36}$$

The average density, $n(t)$ is due to particle number conservation in the nonrelativistic Bose gas time-independent, $n(t) = n$.

2.3.3 The classical-statistical approximation

In the large field occupancy limit, the nonequilibrium quantum field dynamics is accurately described by its classical-statistical evolution with Monte Carlo sampling of quantum initial conditions [54–58],

$$\langle\{\psi(x), \psi^*(y)\}\rangle \gg \langle[\psi(x), \psi^*(y)]\rangle, \tag{2.37}$$

which corresponds indeed to $f \gg 1$ for typical momenta and, for the example of a nonrelativistic Bose gas, to the diluteness parameter ζ being sufficiently small. Classical-

statistical simulations proceed as follows. One samples initial conditions of the field degrees of freedom, typically with Gaussian fluctuations implemented. Each such realization is evolved according to the classical equation of motion. Again, for the example of a nonrelativistic Bose gas this may be the time-dependent Gross-Pitaevskii equation, Eq. (2.13), treating the wave function as a classical field. Any observable is then computed by averaging over classical field trajectories. In the language of path integrals, this corresponds for an observable $\mathcal{O}$ to

$$\langle \mathcal{O} \rangle_{\mathrm{cl}} = \int \mathcal{D}\psi_0 \mathcal{D}\psi_0^* \, \mathcal{D}\pi_0 \mathcal{D}\pi_0^* \, W[\psi_0, \psi_0^*, \pi_0, \pi_0^*] \mathcal{O}_{\mathrm{cl}}[\psi_0, \psi_0^*, \pi_0, \pi_0^*], \qquad (2.38)$$

with $W[\psi_0, \psi_0^*, \pi_0, \pi_0^*]$ a phase-space density functional, typically being a Gaussian functional in all ψ_0, ψ_0^*, π_0 and π_0^*. For initial canonical field variables $\psi_0 = \langle \Psi|_{t=0} \rangle, \pi_0$, etc., the classically-evolved observable reads

$$\mathcal{O}_{\mathrm{cl}}[\psi_0, \psi_0^*, \pi_0, \pi_0^*] = \int \mathcal{D}\psi \mathcal{D}\psi^* \, \mathcal{O}[\psi, \psi^*] \, \delta(\psi - \psi_{\mathrm{cl}}[\psi_0, \psi_0^*, \pi_0, \pi_0^*]) \, \delta(\psi^* - \psi_{\mathrm{cl}}^*[\psi_0, \psi_0^*, \pi_0, \pi_0^*]),$$
$$(2.39)$$

$\psi_{\mathrm{cl}}[\psi_0, \psi_0^*, \pi_0, \pi_0^*]$ indicating the solution to the classical equation of motion of ψ, starting from $(\psi_0, \psi_0^*, \pi_0, \pi_0^*)$, analogously for ψ_{cl}^*.

2.4   Nonthermal fixed points in the two-dimensional Bose gas

Within various studies the universal behavior in the two-dimensional nonrelativistic Bose gas and nearby models has been investigated both via analytical and numerical methods. In this section, we discuss corresponding results of interest in this work, starting with the infrared regime and moving on to the ultraviolet regime, subsequently. Primarily, we focus on universal scaling exponents.

2.4.1   The infrared cascade

Our literature discussion begins with the infrared cascade. All of the studies to be discussed reveal that it is particles being transported to lower and lower momenta that drives the turbulent cascade in this inertial regime, indicated by the fulfilled relation

$$\alpha/\beta = d \qquad (2.40)$$

between scaling exponents α and β as defined in Eq. (2.1), deduced from Eq. (2.3). This holds generally for any β if particles are transported across momentum scales.

The central analytic result is derived in Ref. [4]. Using a two particle-irreducible (2PI)

$1/N$ expansion of nonrelativistic scalar field theory in d spatial dimensions, the authors find that in the overoccupied infrared regime nonrelativistic transport of particles results in $\beta = 1/2$. By a nonequilibrium "anomalous dimension" η, we refer to the spectral function as given in Eq. (2.33) scaling as

$$\tilde{\rho}(p^0, \mathbf{p}) = s^{2-\eta}\tilde{\rho}(s^z p^0, s\mathbf{p}), \tag{2.41}$$

s being a real scaling parameter. Here, z describes the scaling of the dispersion, $\omega(\mathbf{p})$, via

$$\omega(\mathbf{p}) = s^{-z}\omega(s\mathbf{p}). \tag{2.42}$$

An anomalous dimensions manifests itself also in scaling exponents, altering β in the following way [4],

$$\beta = \frac{1}{2 - \eta}. \tag{2.43}$$

In Ref. [4] Orioli *et al.* also provide numerical evidence for their analytic considerations in the form of classical-statistical simulation results in the limit of a large characteristic mode occupancy in the relevant inertial regime, that is, $f(Q) \gg 1$ with f and Q as in Sec. 2.3. In particular, simulating the time-dependent Gross-Pitaevskii equation, Eq. (2.13), they obtain in three spatial dimensions $\alpha = 1.66 \pm 0.12$ and $\beta = 0.55 \pm 0.03$, rather well confirming $\beta = 1/2$ for a vanishing anomalous dimension, η. Indeed, it is particles being transported towards lower momenta since $\alpha/\beta = 3$ is fulfilled to very good accuracy.

In Ref. [59] these numerical results are confirmed, additionally highlighting the role of the dispersive scaling exponent, z, for unequal-time correlation functions far from equilibrium.

While previous numerical results have been obtained for box-initial conditions, the authors of Ref. [46] follow a different route to prepare initial states in the $N = 1$, $d = 2$ Gross-Pitaevskii model. Initial states are generated by phase-imprinting vortex defects into a fully phase-coherent Bose gas, offering parameters such as the vortex density, their winding numbers and the distribution statistics to vary initial conditions. Yet, they emphasize that for the universal scaling behavior far from equilibrium details of the initial state preparation are irrelevant. In fact, for a uniform random distribution of elementary defects with winding number $w = \pm 1$ the authors find scaling exponents of $\alpha = 1.10 \pm 0.08$, $\beta = 0.56 \pm 0.08$, confirming the 2PI $1/N$ prediction of Ref. [4] for particle transport. On the other hand, for a slightly displaced regular lattice of non-elementary defects with winding numbers $w = \pm 6$, the authors obtain $\alpha = 0.402 \pm 0.05$, $\beta = 0.193 \pm 0.05$, which is significantly different from the 2PI $1/N$ result if the anomalous dimension vanishes. However, if $\eta \approx -3$ in Eq. (2.43), then this result is consistent with the corresponding derivation, which, nevertheless, has been obtained for the large N-

limit. A rather heuristic argument in Ref. [46] traces the result of $\beta \approx 1/5$ back to anomalous vortex kinetics. In addition, there are conjectures across the literature, which associate this nonthermal fixed point to the formation of Onsager vortex clusters out of equilibrium via evaporative heating [48, 49].

In Ref. [47] Deng *et al.* study a relativistic single-component interacting scalar field theory in $d = 2$ with its infrared dynamics mapped to that of nonrelativistic scalar fields. Universal scaling of infrared modes, vortex-antivortex superfluid dynamics and the off-equilibrium formation of a Bose-Einstein condensate are observed. Their exponent of by value $\beta = 0.24 \pm 0.08$ confirms the strongly anomalous scaling exponent found in Ref. [46]. The authors show that in the nonrelativistic field modes vortex structures are present even for the box-initial conditions investigated in their work.

In the nonperturbative infrared regime, the relevant mechanism for particle transport towards lower momenta has been identified as strong wave-turbulence by Berges and Sexty in Ref. [8] and as superfluid turbulence by Nowak *et al.* in Ref. [60] by means of characteristic power-laws with momentum in the low-momentum regime of the occupation number spectrum.

2.4.2   The ultraviolet cascade

In the ultraviolet regime, there is a consensus across the literature that energy is transported to higher and higher momenta in the direct cascade, as indicated upon by means of the relation

$$\alpha/\beta = d + z \tag{2.44}$$

between scaling exponents α and β as defined in Eq. (2.1), z being the dispersive scaling exponent as given in Eq. (2.42). This has been deduced in Eq. (2.5) of this work.

Given l-vertex scatterings dominating the dynamics in the ultraviolet and a particle-like dispersion relation as in Eq. (2.22) for the nonrelativistic Bose gas at large momenta, $\omega(\mathbf{p}) = \mathbf{p}^2/2m$, the authors of Ref. [4] deduce that nonrelativistic energy transport analytically yields via perturbative kinetic theory

$$\alpha = -\frac{d+2}{2(l-1)}, \qquad \beta = -\frac{1}{2(l-1)}. \tag{2.45}$$

To the best of our knowledge, to date no numerical study exists, which includes a thorough analysis of self-similar scaling in the nonrelativistic Bose gas at high momenta in any number of dimensions.

The mechanism by means of which energy gets redistributed across momentum scales in the perturbative ultraviolet regime is weak wave-turbulence, as revealed by a Kolmogorov power-law exponent in momentum-space occupation numbers [8].

Chapter 3

An invitation to persistent homology

Aiming for an intuitive, but nonetheless reasonably rigorous treatment, in this chapter we review relevant notions from algebraic and computational topology, constantly accompanied by examples. We first provide necessary background on simplicial complexes in Sec. 3.1, both in full generality and in the form later employed in this work. We move on by defining homology groups and their persistent variants in Sec. 3.2. Persistent homology groups come with an interesting and surprisingly simple classification scheme: barcodes or, equivalently, persistence diagrams. Under fairly general conditions they are stable against perturbations of the point clouds from which, initially, simplicial complexes are constructed, which makes them useful mathematical objects for topological data analysis, cf. Sec. 3.3. Finally, in Sec. 3.4 we describe the notion of functional summaries, which are suitable objects to statistically analyze and capture features of persistence diagrams.

For a general introduction to algebraic topology we refer to Ref. [24]; for a thorough introduction to computational topology the reader may consult Ref. [27], which also constitutes a major resource for this chapter.

3.1 Complexes

Simplicial complexes play a pivotal role in topological data analysis. This section is devoted to their introduction — first in full generality, in order to then move on to a particular type of complex that can be defined from a point cloud: the Delaunay complex. Key to the computational efficiency of our approach is that simplices in the Delaunay complex have at most the dimension of the ambient space, in contrast to other types of simplicial complexes such as the Čech complex [23]. The size of its simplices can be captured by means of the so-called Delaunay radius function. Its sublevel sets specify a nested sequence of subcomplexes, the alpha complexes.
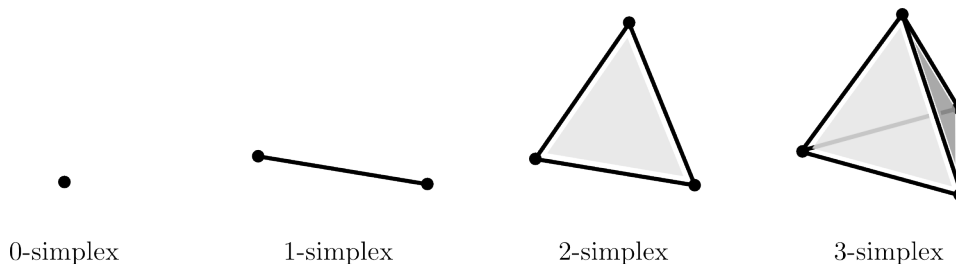
0-simplex   1-simplex   2-simplex   3-simplex

Figure 3.1: Examples of low-dimensional simplices.

Let $d \in \mathbb{N}$ be an arbitrary integer, specifying the dimension of ambient space.

3.1.1 Simplicial complexes

Definition 1. An *abstract simplicial complex* is a finite collection of sets A such that $\alpha \in A$ and $\beta \subseteq \alpha$ implies $\beta \in A$.

The sets in A are its simplices. The dimension of a simplex is $\dim(\alpha) = |\alpha| - 1$ and the dimension of the complex is the maximum dimension of any of its simplices. A face of α is a non-empty subset $\beta \subseteq \alpha$, which is proper if $\beta \neq \alpha$. The vertex set is the union of all simplices, $\operatorname{Vert} A = \bigcup A$. Two abstract simplicial complexes are isomorphic if there exists a bijection $b : \operatorname{Vert} A \to \operatorname{Vert} B$ such that $\alpha \in A$ if and only if $b(\alpha) \in B$.

Definition 2. F be a finite collection of sets. Without assuming convexity of the sets, we define the *nerve* of F to consist of all non-empty subcollections whose sets have a non-empty common intersection,

$$\operatorname{Nrv}(F) = \left\{ G \subseteq F \;\middle|\; \bigcap_{x \in G} x \neq \emptyset \right\}. \tag{3.1}$$

No matter what sets form the elements of F, $\operatorname{Nrv}(F)$ is always an abstract simplicial complex. Indeed, if $\bigcap H \neq \emptyset$ and $G \subseteq H$ then $\bigcap G \neq \emptyset$. We can realize the nerve geometrically in some Euclidean space. It thus makes sense to talk about its topology type and its homotopy type.

So far, we did not have to worry about how to embed an abstract simplicial complex into Euclidean space. The definition of a simplicial complex, however, requires this.

Let $p_0, p_1, \ldots, p_n$ be points in $\mathbb{R}^d$. A point $x = \sum_{i=0}^{n} \lambda_i p_i$ is an affine combination of the p_i if the λ_i sum to 1. The affine hull is the set of affine combinations. It is an n-plane if the $n+1$ points are affinely independent, that is, any two affine combinations $x = \sum \lambda_i p_i$ and $y = \sum \mu_i p_i$ are the same if and only if $\lambda_i = \mu_i \; \forall i$. In other words, the $n+1$ points are affinely independent if and only if the n vectors $p_i - p_0$, for $1 \leq i \leq n$,

are linearly independent.

An affine combination $x = \sum \lambda_i p_i$ is a convex combination if all λ_i are non-negative. The convex hull is the set of convex combinations. An ℓ-simplex is the convex hull of $\ell+1$ affinely independent points, $\sigma = \mathrm{conv}(p_{j_0}, p_{j_1}, \dots, p_{j_\ell})$, $j_i \in \{p_0, \dots, p_n\}$. Its dimension reads $\dim \sigma = \ell$. A vertex is a 0-simplex, an edge a 1-simplex, a triangle a 2-simplex and a tetrahedron a 3-simplex, see Fig. 3.1. A face of σ is the convex hull of a non-empty subset of $\{p_i \mid i = 0, \dots, n\}$ and it is proper if the subset is not the entire set. We write $\tau \leq \sigma$ if τ is a face and $\tau < \sigma$ if it is a proper face of σ. If τ is a (proper) face of σ we call σ a (proper) coface of τ.

Definition 3. A *simplicial complex* is a finite collection of simplices K such that $\sigma \in K$ and $\tau \leq \sigma$ implies $\tau \in K$, and $\sigma, \sigma_0 \in K$ implies $\sigma \cap \sigma_0$ is either empty of a face of both.

Thus, the key property of a simplicial complex is that it is closed under taking faces. The dimension of K is the maximum dimension of any of its simplices. The underlying space, denoted $|K|$, is the union of its simplices together with the topology inherited from the ambient Euclidean space in which the simplices live. A subcomplex of K is a simplicial complex $L \subseteq K$. A particular subcomplex is the j-skeleton consisting of all simplices of dimension j or less, $K^{(j)} = \{\sigma \in K \mid \dim \sigma \leq j\}$. The 0-skeleton is also referred to as the vertex set.

The orientation of an ℓ-simplex $\sigma = \{p_0, \dots, p_\ell\}$ is an equivalence class of permutations of its vertices, $(p_0, \dots, p_\ell) \sim (p_{\pi(0)}, \dots, p_{\pi(\ell)})$ if $\mathrm{sign}(\pi) = 1$. An oriented simplex is denoted by $[\sigma]$.

3.1.2 The Delaunay complex

Following Refs. [27, 61], we introduce a particular type of complex, constructed from an input point cloud $X \subset \mathbb{R}^d$, that is, a finite subset of points in Euclidean space: the Delaunay complex. We first provide a construction as the dual of the Voronoi diagram and subsequently give a second, equivalent way to construct it.

The *Voronoi cell* of an arbitrary point $p_i \in X$ consists of all points in $\mathbb{R}^d$ for which p_i is the closest,

$$\mathrm{Vor}(p_i) = \{x \in \mathbb{R}^d \mid ||x - p_i|| \leq ||x - p_j|| \, \forall j\}. \tag{3.2}$$

The *Voronoi diagram* of P is the set of Voronoi cells,

$$\mathrm{Vor}(P) = \{\mathrm{Vor}(p_i) \mid 0 \leq i \leq n\}. \tag{3.3}$$

Throughout, the $\mathrm{Vor}(p_i)$ are closed convex polyhedrons. By construction, any two Voronoi cells have disjoint interiors but they may intersect along shared pieces of their boundaries. By definition, the *Delaunay complex*, $\mathrm{Del}(P)$, is dual to the Voronoi diagram:

Whenever two Voronoi cells share a common side, then the edge connecting the two corresponding points belongs to the Delaunay complex. Whenever three Voronoi cells share a common corner, the triangle spanned by the three corresponding points belongs to the Delaunay complex. The construction proceeds analogously to tetrahedrons and higher dimensional simplices. More formally,

$$\mathrm{Del}(P) = \mathrm{Nrv}(\mathrm{Vor}(P)) = \left\{ X \subseteq \mathrm{Vor}\, P \,\Big|\, \bigcap X \neq \emptyset \right\}. \tag{3.4}$$

An important property of a point cloud X is to be in general position, which, for example, excludes the possibility that three or more points are collinear or that four or more points lie on a single circle.

Definition 4. We say that a finite subset $X \subset \mathbb{R}^d$ is in *general position*, if for every $0 \leq k \leq d$,

  (i) no $k+2$ points belong to a common k-plane,

 (ii) no $k+3$ points belong to a common k-sphere,

(iii) considering the unique k-sphere that passes through $k+2$ points, no $k+1$ of these points belong to a k-plane that passes through the center of the k-sphere.

The Delaunay complex is a simplicial complex if and only if the Voronoi diagram is primitive, that is, if the intersection of any $1 \leq k+1 \leq d+2$ Voronoi cells is either empty or $(d-k)$-dimensional. Assuming general position of the input point cloud X, the Voronoi diagram, $\mathrm{Vor}(X)$, is primitive, and the Delaunay complex makes up a simplicial complex, a posteriori justifying its nomenclature.

By construction, every point $q \in \mathrm{Vor}(Y)$, $Y \subseteq X$ being the vertex set of a simplex in $\mathrm{Del}(X)$, is equally far away from all points in Y and at least as far away from all points in $X \setminus Y$. We call the sphere with center q and radius $||q - p_i||$, $p_i \in Y$, a *circumsphere* because all points of Y lie on the sphere. We additionally call it *empty* because all points of X lie on or outside the sphere.

Equivalently to before, the Delaunay complex, $\mathrm{Del}(X)$, can be defined as consisting of all those simplices whose circumspheres are empty [62], assuming general position of X.

We define a function on $\mathrm{Del}(P)$, the *Delaunay radius function* $\mathrm{Rad} : \mathrm{Del}(P) \to \mathbb{R}$, mapping any simplex to the smallest radius of all its empty circumspheres [61]. The function Rad is well-defined, since every simplex $Y \subset X$ has a unique smallest circumsphere, namely the unique circumsphere whose center, q lies in the affine hull of $Y = \{p_{j_0}, \ldots, p_{j_k}\}$. Mathematically speaking, Rad specifies a generalized discrete Morse function [61, 63]. Intuitively, it provides a measure for the size of a simplex.
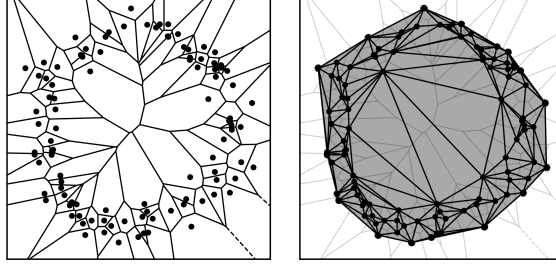
Figure 3.2: Left: The Voronoi diagram of the example point cloud consisting of 100 points sampled from a unit circle with Gaussian noise added to their positions. Right: Its dual, the Delaunay complex. Computations via SciPy and GUDHI.

In Fig. 3.2 the Voronoi diagram and the Delaunay complex of an example point cloud are displayed, the point cloud consisting of 100 points sampled from a unit circle with Gaussian noise added to their positions. Note that simplices of different Delaunay radii are visually of distinct dominance, typically. Smaller simplices appear foremost around noisy accumulations of points, while simplices of larger radii mainly make up the interior of the circular structure of the point cloud.

3.1.3 Alpha complexes

Let $r > 0$. $B_r(x) \subset \mathbb{R}^d$ be the ball with radius r around $x \in \mathbb{R}^d$. We define the union of balls around the point cloud $X = \{p_0, \ldots, p_n\}$:

$$U_X(r) = \bigcup_{i=0}^{n} B_r(p_i). \tag{3.5}$$

Alternatively, we may view $U_X(r)$ as a sublevel set of the Euclidean distance function $\varrho_X : \mathbb{R}^d \to [0, \infty)$, $\varrho_X(x) = \min_{0 \leq i \leq n} ||x - p_i||$:

$$U_X(r) = \varrho_X^{-1}([0, r]). \tag{3.6}$$

If $x \in U_X(r)$ belongs to the Voronoi cell $\text{Vor}(p_i)$, then $x \in B_r(p_i)$. Thus, $\text{Vor}(p_i) \cap U_X(r) = \text{Vor}(p_i) \cap B_r(p_i) =: R_r(p_i)$, which is convex. Denote

$$\text{Reg}(X, r) := \bigcup_{i=0}^{n} R_r(p_i). \tag{3.7}$$

We note that if a collection of sets $R_r(p_i)$ has a non-empty common intersection, then so do the corresponding Voronoi cells. Hence, the nerve of $\text{Reg}(X, r)$ is isomorphic to a subsystem of the nerve of $\text{Vor}(X)$. We use the same canonical geometric realization as
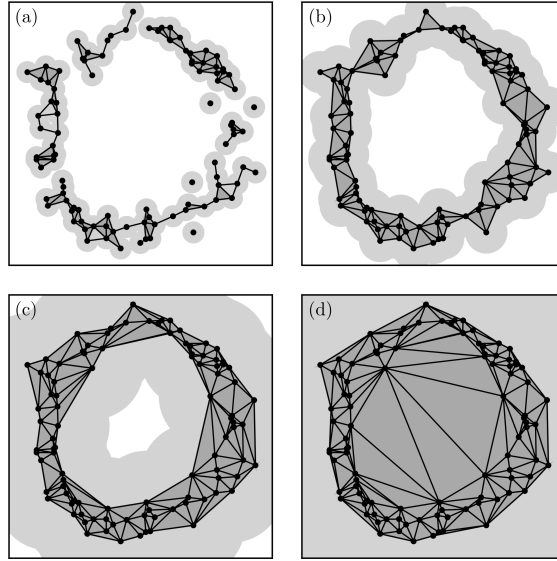
Figure 3.3: Alpha complexes of the example point cloud, with successively increasing radii from (a) to (d). Light gray: balls of the respective radius around the point cloud. Dark gray: corresponding alpha complexes. Computations via GUDHI.

for Delaunay complexes and call the result the alpha complex of P, denoting it by $\alpha_r(X)$. Specifically, $\alpha_r(X)$ is the realization of the nerve of $\mathrm{Reg}(X, r)$ obtained by mapping $R_r(p_i)$ to p_i for each i. By construction, the alpha complex is a subcomplex of the Delaunay complex.

Though uncountably many unions of balls $U_X(r)$ exist, only finitely many alpha complexes exist for a given point cloud $X \subset \mathbb{R}^d$. Additionally, for all $0 \leq r \leq s$ we find $\alpha_r(X) \subseteq \alpha_s(X)$. To this end, we obtain a filtration of alpha complexes, that is, a nested sequence,

$$\emptyset \subseteq \alpha_{r_1}(X) \subseteq \cdots \subseteq \alpha_{r_n}(X) = \mathrm{Del}(X), \tag{3.8}$$

with $r_i \leq r_j$ for all $i < j$.

As *alpha shape* we define the union of all simplices in the alpha complex, which is a notion also regularly appearing in the literature [27–29]. Formally, the underlying space $|\alpha_r(X)|$ is what we consider the alpha shape of X, that is, the set of points contained in the simplices of $\alpha_r(X)$ together with the subset topology inherited from the Euclidean space.

Again referring to the example point cloud, in Fig. 3.3 corresponding alpha complexes of different radii are displayed. Note that at intermediate radii the approximately circular structure is visible, while for small radii the alpha complex mainly reflects noisyness in the data. At large radii, the full Delaunay complex is recovered. Leading to the notion of persistent homology, it is a crucial insight that independent cycles such as the circular

structure in the given data appear in alpha complexes of a certain radius and disappear again at a higher radius.

3.2 Persistent homology

Given a simplicial complex, we introduce the chain complex and homology groups in order to move on to relative homology groups and to the additional structure emerging from filtered simplicial complexes: persistence. Persistent homology groups then provide multi-scale information on the topological structure of the input data, making them the fundamental mathematical objects of interest in this work.

In what follows we restrict to the ground field $\mathbb{Z}_2$.

3.2.1 Homology groups

We call the free Abelian group on the set of oriented ℓ-simplices of a simplicial complex K the ℓ-th chain group C_ℓ, where $[\sigma] = -[\tau]$ if $\sigma = \tau$ and σ and τ are oriented differently. An element $c \in C_\ell$ is an ℓ-chain, $c = \sum_i m_i [\sigma_i]$ with $\sigma_i \in K$ and $m_i \in \mathbb{Z}_2$. In what follows we omit orientation from notations and assume that all simplices are oriented. Working with $\mathbb{Z}_2$-coefficients, we can think of an ℓ-chain as a set of ℓ-simplices, namely those σ_i with $m_i = 1$. We define the boundary operator $\partial_\ell : C_\ell \to C_{\ell-1}$ to be the linear map defined by its action on a simplex $\sigma = [p_0, \ldots, p_\ell] \in c$,

$$\partial_\ell \sigma = \sum_j (-1)^j [p_0, p_1, \ldots, \hat{p}_j, \ldots, p_\ell], \tag{3.9}$$

$\hat{p}_j$ indicating that p_j is deleted from the denoted sequence. Intuitively, the boundary operator maps an ℓ-chain to its boundary, validating its nomenclature. In particular, since the boundary of a boundary is empty, $\partial_\ell \circ \partial_{\ell+1} = 0$. The boundary operator connects the chain groups into an exact sequence, the chain complex C_*,

$$\cdots \to C_{\ell+1} \xrightarrow{\partial_{\ell+1}} C_\ell \xrightarrow{\partial_\ell} C_{\ell-1} \to \ldots. \tag{3.10}$$

To this end, the boundary group $B_\ell := \mathrm{im}(\partial_{\ell+1})$ and the cycle group $Z_\ell := \ker(\partial_\ell)$ are nested, $B_\ell \subseteq Z_\ell \subseteq C_\ell$.

The ℓ-*th homology group* is then defined as

$$H_\ell := Z_\ell / B_\ell. \tag{3.11}$$

Its elements are equivalence classes of cycles, $c + B_\ell$ with $c \in Z_\ell$. Two cycles, $c, c' \in Z_\ell$, are called *homologous*, $c \sim c'$, if $[c] = [c']$. Z_ℓ being a group with respect to the addition of elements, this structure is inherited to H_ℓ. Defined over a ring $\mathbb{Z}$, homology groups are

$\mathbb{Z}$-modules. If defined over a field such as $\mathbb{Z}_2$, homology groups become vector spaces.

In any case, we define the *ℓ-th Betti number* as the rank of the ℓ-th homology group,

$$\beta_\ell := \dim_{\mathbb{Z}_2}(H_\ell). \tag{3.12}$$

Betti numbers count the number of independent ℓ-dimensional cycles (in the sense of not being homologous). For example, β_0 counts the number of connection components of the topological space minus one (in reduced homology as described below), β_1 counts the number of loops enclosing independent tunnels, β_2 counts the number of shells enclosing separate voids.

If K is to describe a topological space homotopic to a single-point space, then $H_0(K) = \mathbb{Z}_2$, while for any $i \geq 1$ we find $H_i(K) = 0$. The idea of *reduced homology groups* is to replace $H_0(K)$ by a variant $\tilde{H}_0(K)$ which has dimension zero. To accomplish this, we define the augmented chain complex

$$\cdots \to C_{\ell+1} \xrightarrow{\partial_{\ell+1}} C_\ell \xrightarrow{\partial_\ell} C_{\ell-1} \to \ldots \xrightarrow{\partial_1} C_0 \xrightarrow{\epsilon} \mathbb{Z}_2 \to 0, \tag{3.13}$$

where

$$\epsilon \left(\sum_i m_i \sigma_i \right) = \sum_i m_i. \tag{3.14}$$

We define *reduced* homology groups as

$$\tilde{H}_\ell(K) := \begin{cases} \ker(\partial_\ell)/\mathrm{im}(\partial_{\ell+1}) & \text{for } \ell \geq 1, \\ \ker(\epsilon)/\mathrm{im}(\partial_1) & \text{for } \ell = 0. \end{cases} \tag{3.15}$$

It is not difficult to show that

$$H_0(K) = \tilde{H}_0(K) \oplus \mathbb{Z}_2, \qquad H_\ell(K) = \tilde{H}_\ell(K) \; \forall k \geq 1. \tag{3.16}$$

Indeed, defining reduced Betti numbers as the dimension of reduced homology groups, $\tilde{\beta}_\ell := \dim_{\mathbb{Z}_2}(\tilde{H}_\ell(K))$, we find that $\tilde{\beta}_0$ counts the number of connection components of *K minus one*. All higher-order Betti numbers remain unchanged from the reduction process. In everything that follows we work solely in reduced homology, omitting it from notations for this reason.

As an example of a topologically nontrivial space consider the two-dimensional torus as displayed in Fig. 3.4. We find that the three cycles a, b and c cannot be continuously deformed into each other. Notably, cycles a and b cannot be shrunk to a point. For c, however, this is the case, making it homologous to zero. In reduced homology, the
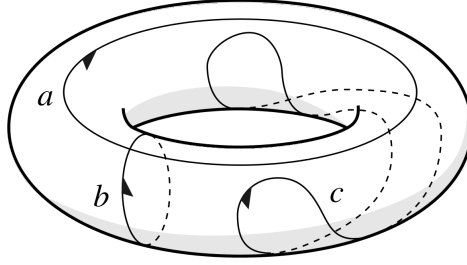
Figure 3.4: Cycles on a 2-torus. Reprinted from Wikipedia.

homology groups of the 2-torus read

$$H_0(T^2) = 0, \qquad H_1(T^2) = \mathbb{Z}_2 \oplus \mathbb{Z}_2, \qquad H_2(T^2) = \mathbb{Z}_2. \tag{3.17}$$

Intuitively, this resembles the fact that it is made up from a single connection component, that the two independent 1-cycles a and b are present and that T^2 encloses a single void. From its homology groups we can also read off, that a and b represent the only two independent 1-dimensional homology classes. Any other 1-cycle is homologous to either zero, a or b.

Let $f : K \to L$ be a map between simplicial complexes which is a *simplicial map*, that is, $f(\sigma)$ is a simplex in L for all $\sigma \in K$. A simplicial map induces a linear map from the chains of K to the chains of the same dimension of L: if $c = \sum m_i \sigma_i$ is an ℓ-chain in K, then $f_\#(c) := \sum m_i \tau_i$ with $\tau_i = f(\sigma_i)$ if it has dimension ℓ and $\tau_i = 0$ if $f(\sigma_i)$ has dimension less than ℓ. In particular, we find that $f_\# \circ \partial_K = \partial_L \circ f_\#$ with ∂_K and ∂_L being the boundary maps of the two complexes, respectively. $f_\#$ thus takes cycles to cycles, $f_\#(Z_\ell(K)) \subseteq f_\#(Z_\ell(L))$, and boundaries to boundaries, $f_\#(B_\ell(K)) \subseteq f_\#(B_\ell(L))$. For this reason it induces a homomorphism on homology groups, $f_* : H_\ell(K) \to H_\ell(L)$. We will regularly make use of this, in particular with inclusion maps between complexes.

3.2.2 Relative homology groups

We extend homology beyond single simplicial complexes by considering nested pairs of such and studying their difference.

Let $A \subseteq K$ be a simplicial subcomplex of a simplicial complex K. Then we find for ℓ-th chain groups, $C_\ell(A) \subseteq C_\ell(K)$, ι labeling the corresponding inclusion map. Being vector spaces, this makes $C_\ell(K, A) := C_\ell(X)/C_\ell(A)$ a well-defined vector space. In addition, we obtain $\partial_K \circ \iota = \iota \circ \partial_A$. Thus, the boundary map on $C_*(K)$ leaves $C_*(A)$ invariant and therefore descends to a map ∂ on the quotient $C_*(K, A)$, $\partial_\ell : C_\ell(K, A) \to C_{\ell-1}(K, A)$. By construction, we obtain $\partial_{\ell-1} \circ \partial_\ell = 0$. To this end, as before we can
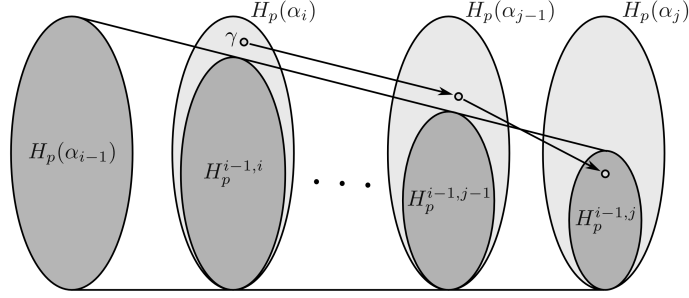
Figure 3.5: An illustration of the definitions of birth and death of homology classes. Picture inspired by Ref. [27].

define *relative homology groups of* (K, A),

$$H_\ell(K, A) := \frac{\ker(\partial_\ell : C_\ell(K, A) \to C_{\ell-1}(K, A))}{\operatorname{im}(\partial_{\ell+1} : C_{\ell+1}(K, A) \to C_\ell(K, A))}. \tag{3.18}$$

Relative homology classes are represented by relative cycles, that is, chains whose boundaries are chains on A: $c \in C_\ell(K)$ such that $\partial c \in C_{\ell-1}(A)$ [64].

3.2.3   Persistent homology groups

Additional structure arises, if one considers homology groups of a *filtered* simplicial complex. To this end, we consider the alpha complexes constructed in Sec. 3.1.3, defining $\alpha_i := \alpha_{r_i}(X)$, $X \subset \mathbb{R}^d$ being a point cloud. We recall that $\alpha_i \subset \alpha_j$ and find an inclusion map $\iota^{i,j} : \alpha_i \to \alpha_j$ for all $i \leq j$, resulting in a filtration of the Delaunay complex, $\mathrm{Del}(X)$.

For all $i \leq j$, the inclusion map $\iota^{i,j} : \alpha_i \to \alpha_j$ induces a homomorphism between homology groups, $\iota_\ell^{i,j} : H_\ell(\alpha_i) \to H_\ell(\alpha_j)$, for each dimension $\ell = 0, \ldots, d$. To this end, the filtration of alpha complexes yields a sequence of homology groups,

$$0 \to H_\ell(\alpha_1) \to \cdots \to H_\ell(\alpha_n) = H_\ell(\mathrm{Del}(X)). \tag{3.19}$$

Within this sequence, homology classes are born and later die again, when they become trivial or merge with other classes. With this intuition in mind, we define *ℓ-th persistent homology groups* as follows,

$$H_\ell^{i,j} := \operatorname{im}(\iota_\ell^{i,j}), \qquad \forall \, 0 \leq i \leq j \leq n. \tag{3.20}$$

The ℓ-th persistent Betti numbers are defined as

$$\beta_\ell^{i,j} = \dim(H_\ell^{i,j}), \tag{3.21}$$

counting the number of homology classes that are born at or before r_i and die after r_j.
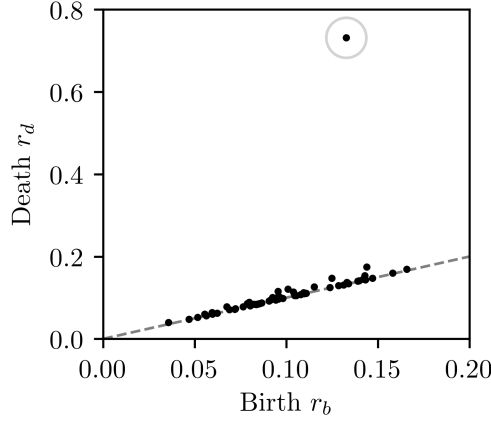
Figure 3.6: The persistence diagram of 1-dimensional persistent homology classes of the example point cloud, $\text{Dgm}_1(X)$. The highlighted homology class reflects the dominant circular structure present in the example point cloud. Computations via GUDHI.

To make the notions of birth and death of a simplex rigorous, let $\gamma \in H_\ell(\alpha_i)$. We say that γ is born at α_i if $\gamma \notin H_\ell(\alpha_{i-1})$. If γ is born at α_i, then it dies entering α_j, if it merges with an older class as going from α_{j-1} to α_j, that is, $\iota_\ell^{i,j-1}(\gamma) \notin H_\ell^{i-1,j-1}$, but $\iota_\ell^{i,j}(\gamma) \in H_\ell^{i-1,j}$. The persistence of γ is defined as $\text{pers}(\gamma) := r_j - r_i$, if γ is born at α_i and dies entering α_j. For an illustration of this definition we refer to Fig. 3.5.

Let $\mu_\ell^{i,j}$ be the number of ℓ-dimensional classes born at α_i and dying entering α_j. We define the *persistence diagram*, $\text{Dgm}_\ell(X)$, to consist of all $(r_i, r_j) \in \overline{\mathbb{R}}_+^2$ corresponding to ℓ-dimensional persistent homology classes, taking respective multiplicities $\mu_\ell^{i,j}$ into account. Throughout this work, zero-persistence homology classes are not taken into account.

We find an interesting identity including the $\mu_\ell^{i,j}$ and the Betti numbers, namely

$$\mu_\ell^{i,j} = (\beta_\ell^{i,j-1} - \beta_\ell^{i,j}) - (\beta_\ell^{i-1,j-1} - \beta_\ell^{i-1,j}), \tag{3.22}$$

for all $i < j$ and all ℓ. The first term on the right hand side of this equation counts those classes that are born at or before α_i and die entering α_j, while the second term counts those classes that are born at or before α_{i-1} and die entering α_j. It follows that for every pair of indices $0 \leq i, j \leq n$ and every dimension ℓ, the ℓ-th persistent Betti number can be computed via

$$\beta_\ell^{i,j} = \sum_{p \leq i} \sum_{q > j} \mu_\ell^{p,q}. \tag{3.23}$$

This important property, intuitively, describes that persistence diagrams encode the entire information about persistent homology groups up to isomorphism.

Returning to the example point cloud, in Fig. 3.6 we display its persistence diagram of

one-dimensional homology classes. At its bottom an accumulation of persistent homology classes occurs, which are born at small radii and rapidly die again. These classes may be interpreted as reflecting the noise in the data. Take note of the persistence pair at the top with comparably high persistence. The corresponding persistent homology class represents the overall circular structure of the point cloud. This way, persistent homology provides us with a multi-scale topological summary of point cloud data.

Actually, the intuitive definition of the birth and death of homology classes provided above has a conceptual drawback [23]. Any two homology classes that are born at the same birth radius r_b, one of them merging with the other one at a radius $r > r_b$, only die jointly at the death radius of the resulting homology class with highest death radius. A circumvention of this is provided by what is called the structure theorem of persistence modules [25, 26]. It states that up to isomorphism the family $\mathcal{M}_\ell := ((H_\ell(\alpha_i))_i, (\iota_\ell^{i,j})_{i \leq j})$ can be described by its persistence diagram. Thus, the latter forms a complete invariant of the persistence module $\mathcal{M}_\ell$.

3.3   The stability of persistence diagrams

Given a point cloud X, it is a natural question to ask for the stability of the persistence diagram of the filtration of alpha complexes of X against perturbations of the latter. This is precisely what persistence theorems accomplish, making persistent homology a useful notion in the analysis of potentially noisy data.

In this section we describe two of the first such stability results, for two different types of metrics on persistence diagrams: the Bottleneck and the Wasserstein distance. Actually, both do not describe persistence diagrams of alpha complexes but, instead, those of the filtration of sublevel sets of functions with preimage a triangulable topological space.

Throughout this section, a persistence diagram can be regarded as a multiset of points in the plane $\bar{\mathbb{R}}^2 = ([0, \infty) \cup \{\infty\})^2$, all laying above the diagonal. We may add arbitrarily many points with zero persistence on the diagonal in order to simplify definitions. Again, we work with homology groups having $\mathbb{Z}_2$-coefficients.

3.3.1   Bottleneck distance stability

Let X, Y be two persistence diagrams and $\eta : X \to Y$ a bijection between them, possibly adding points to the diagonal to be able to define a bijection. Measuring the distance between two points $x = (x_1, x_2)$ and $y = (y_1, y_2)$ as $||x - y||_\infty = \max\{|x_1 - y_1|, |x_2 - y_2|\}$ and taking the infimum over all bijections, we define the *bottleneck distance* between X and Y as

$$W_\infty(X, Y) = \inf_{\eta : X \to Y} \sup_{x \in X} ||x - \eta(x)||_\infty. \tag{3.24}$$

Indeed, with $W_\infty(X,Y) = 0$ if and only if $X = Y$, $W_\infty(X,Y) = W_\infty(Y,X)$ and $W(X,Z) \leq W_\infty(X,Y) + W_\infty(Y,Z)$ we find that W_∞ is a metric on the space of persistence diagrams.

We note that homology groups can be defined not only from simplicial complexes, but also from any topological space, for example via singular homology. For details on this we refer to Refs. [24, 64].

Definition 5. Let T be a topological space and f a real function on T. A *homological critical value* of f is a real number a for which there exists an integer ℓ such that for all sufficiently small $\epsilon > 0$ the map $H_\ell(f^{-1}(-\infty, a - \epsilon]) \to H_\ell(f^{-1}(-\infty, a + \epsilon])$ induced by inclusion is not an isomorphism.

Definition 6. A function $f : T \to \mathbb{R}$ is *tame* if it has a finite number of homological critical values and the homology groups $H_\ell(f^{-1}(-\infty, a])$ are finite-dimensional for all $\ell \in \mathbb{N}$ and $a \in \mathbb{R}$.

Let $f : T \to \mathbb{R}$ be such a tame function and set $X_a := f^{-1}((-\infty, a])$. Noting that $X_a \subseteq X_b$ whenever $a \leq b$, we obtain the filtration of sublevel sets. To this end, for any $a \leq b$ there exists a map $\iota_\ell^{a,b} : H_\ell(X_a) \to H_\ell(X_b)$ induced by the inclusion. Similarly to before, we say that a class $\alpha \in H_\ell(X_a)$ is born at X_a if $\alpha \notin \mathrm{im}(\iota_\ell^{a-\delta,a})$ for any $\delta > 0$, setting $b(\alpha) = a$. A class α born at X_a dies entering X_b if $\iota_\ell^{a,b-\delta}(\alpha) \notin \mathrm{im}(\iota_\ell^{a-\delta,b-\delta})$ for all $\delta > 0$ but $\iota_\ell^{a,b}(\alpha) \in \mathrm{im}(\iota_\ell^{a-\delta,b})$, setting $d(\alpha) = b$. We define its persistence as $\mathrm{pers}(\alpha) = d(\alpha) - b(\alpha)$. By $\mathrm{Dgm}_\ell(f)$ we denote the corresponding persistence diagram, consisting of all points $(b(\alpha), d(\alpha))$ for ℓ-dimensional persistent homology classes α.

We recall that a topological space is triangulable if there is a (finite) simplicial complex with homeomorphic underlying space.

Following Ref. [65], the Bottleneck stability theorem finally reads as follows.

Theorem 1 (Bottleneck stability theorem)**.** *Let T be a triangulable space with continuous tame functions $f, g : T \to \mathbb{R}$. Then, the persistence diagrams satisfy for all $\ell \in \mathbb{N}$*

$$W_\infty(\mathrm{Dgm}_\ell(f), \mathrm{Dgm}_\ell(g)) \leq ||f - g||_\infty = \sup_x |f(x) - g(x)|. \tag{3.25}$$

To this extend, under mild assumptions on the function, the persistence diagram is stable. Small changes in the function imply only small changes in the diagram. The proof of the theorem proceeds via diagram chasing and an intermediate upper bound on the Hausdorff distance between the persistence diagrams.

3.3.2 Wasserstein distance stability

The Wasserstein stability theorem we deduce in somewhat more detail than the Bottleneck stability theorem, since we will use intermediate and final results in later deductions.

Derivations proceed along the lines of Ref. [66]. We begin by stating preliminary technicalities.

Let X be a triangulable, compact n-dimensional metric space, $d : X \times X \to \mathbb{R}$ its metric. As stated previously, a triangulation of X is a finite simplicial complex K with homeomorphism $\vartheta : |K| \to X$. We define the diameter of a simplex $\sigma \in K$ as $\mathrm{diam}(\sigma) := \max_{x,y \in \sigma} d(\vartheta(x), \vartheta(y))$ and the mesh of a triangulation K as $\mathrm{mesh}(K) := \max_{\sigma \in K} \mathrm{diam}(\sigma)$. For all $0 \leq \ell \leq n$ we denote the ℓ-skeleton of K by $K^{(\ell)}$. We are interested in the smallest triangulation with mesh at most r,

$$N(r) := \min_{\mathrm{mesh}(K) \leq r} \mathrm{card}(K), \qquad N_\ell(r) := \min_{\mathrm{mesh}(K) \leq r} (\mathrm{card}(K^{(\ell)}) - \mathrm{card}(K^{\ell-1})). \quad (3.26)$$

As an example consider X a compact Riemannian manifold. Then, for sufficiently small r there exist $c, C > 0$, such that $c/r^n \leq N(r) \leq C/r^n$.

Additionally, for any subset $z \subseteq X$, we define

$$z^r := \{x \in X \,|\, \exists\, y \in z : d(x,y) \leq r\}. \quad (3.27)$$

A series of lemmas brings us to the main results.

Lemma 1 (Snapping Lemma)**.** Let K be a triangulation of a compact metric space X with $\mathrm{mesh}(K) = r$. Then for each cycle z of dimension ℓ in X there is a cycle $\bar{z}$ in the ℓ-skeleton of K that is homologous to z inside z^r.

A crucial ingredient of Wasserstein stability is the involved functions being Lipschitz. A function $f : X \to \mathbb{R}$ is Lipschitz on X, if there exists a positive constant c, such that $|f(x) - f(y)| \leq c\, d(x,y)$ for any $x, y \in X$. The infimum of such c is called Lipschitz constant and denoted by $\mathrm{Lip}(f)$.

A useful lemma follows, including persistent homology notions.

Lemma 2 (Persistent Cycle Lemma)**.** Let X be a triangulable, compact metric space, $f : X \to \mathbb{R}$ a tame Lipschitz function. Then the number of points in the persistence diagrams of f whose persistence exceeds ϵ is at most $N(\epsilon/\mathrm{Lip}(f))$.

We define the *degree-k total persistence*,

$$\mathrm{Pers}_k(f,t) := \sum_{\mathrm{pers}(x) > t} \mathrm{pers}(x)^k, \qquad \mathrm{Pers}_k(f) := \mathrm{Pers}_k(f,0). \quad (3.28)$$

Lemma 3 (Moment Lemma)**.** Let X be a triangulable, compact metric space, $f : X \to \mathbb{R}$ a tame Lipschitz function. Then,

$$\mathrm{Pers}_k(f,t) \leq t^k N\left(\frac{t}{\mathrm{Lip}(f)}\right) + k \int_{\epsilon=t}^{\mathrm{Amp}(f)} N\left(\frac{\epsilon}{\mathrm{Lip}(f)}\right) \epsilon^{k-1}\, d\epsilon, \quad (3.29)$$

setting $\text{Amp}(f) = \max_{x \in X} f(x) - \min_{y \in X} f(y)$.

The first term on the right-hand side of Eq. (3.29) is denoted by A, the second by B.

We define the notion of polynomial growth and bounded total persistence as follows. Assume that the size of the smallest triangulation *grows polynomially* with one over the mesh, that is, there exist $C_0, M > 0$, such that $N(r) \leq C_0/r^M$ for all $r > 0$. Let $\delta > 0$ and $k = M + \delta$. We then find upper bounds for A and B:

$$A \leq C_0 \text{Lip}(f)^M \text{Amp}(f)^\delta, \qquad B \leq C_0 \text{Lip}(f)^M \text{Amp}(f)^\delta \frac{M + \delta}{\delta}, \qquad (3.30)$$

which motivates the introduction of the following concept.

Definition 7. A metric space X *implies bounded degree-k total persistence*, if there exists a constant $C_X > 0$ depending only on X, such that $\text{Pers}_k(f) \leq C_X$ for every tame function $f : X \to \mathbb{R}$ with $\text{Lip}(f) \leq 1$.

As an example consider $X = S^n$. One finds a $C_0 > 0$, such that $N(r) \leq C_0/r^n$. Thus, a $C > 0$ exists with $\text{Pers}_k(f) \leq C$ for some C and every $k = n + \delta$, $\delta > 0$.

Let $f, g : X \to \mathbb{R}$ be two tame functions with persistence diagrams $\text{Dgm}_\ell(f)$ and $\text{Dgm}_\ell(g)$, respectively, $\ell \in \mathbb{N}$. The *degree-p Wasserstein distance* between the persistence diagrams of f and g is defined as

$$W_p(f, g) = \left[\sum_\ell \inf_{\gamma_\ell} \sum_x ||x - \gamma_\ell(x)||_\infty^p \right]^{1/p}, \qquad (3.31)$$

where the first sum runs of all dimensions ℓ, the infimum is taken over all bijections $\gamma_\ell : \text{Dgm}_\ell(f) \to \text{Dgm}_\ell(g)$, adding zero-persistence points to render this well-defined, and the second sum runs over all $x \in \text{Dgm}_\ell(f)$.

Theorem 2 (Wasserstein Stability Theorem)**.** *Let X be a triangulable, compact metric space that implies bounded degree-k total persistence for $k \geq 1$, and let $f, g : X \to \mathbb{R}$ be two tame Lipschitz functions. Then,*

$$W_p(f, g) \leq C_k^{1/p} \cdot ||f - g||_\infty^{1 - k/p} \qquad (3.32)$$

for all $p \geq k$ and $C_k = C_X \max\{\text{Lip}(f)^k, \text{Lip}(g)^k\}$.

Another result follows quickly.

Theorem 3 (Total Persistence Stability Theorem)**.** *Let X be a triangulable, compact metric space that implies bounded degree-k total persistence for $k \geq 0$, and let $f, g : X \to \mathbb{R}$ be two tame Lipschitz functions. Then,*

$$|\text{Pers}_p(f) - \text{Pers}_p(g)| \leq 4p \, w^{p-1-k} C_k \cdot ||f - g||_\infty, \qquad (3.33)$$

for every real $p \geq k + 1$, $C_k := C_X \max\{\mathrm{Lip}(f)^k, \mathrm{Lip}(g)^k\}$ and w is bounded from above by $\max\{\mathrm{Amp}(f), \mathrm{Amp}(g)\}$.

As the notation suggests, the Bottleneck distance, W_∞, arises indeed as the limit of the Wasserstein distance, W_p, for $p \to \infty$ [27]. To this end, under the assumptions of the Wasserstein stability theorem the Bottleneck stability theorem follows.

In Sec. 5.6 we will deduce from the Wasserstein stability theorem and intermediate notions such as bounded total persistence for the sequence of alpha complexes a bound on the number of persistent homology classes of a given size.

3.4   Statistics via functional summaries

Persistence diagrams do not naturally lead themselves to statistical goals, because their complicated structure makes common algebraic operations such as addition, division and multiplication challenging. To bypass these issues, functional summaries of persistence diagrams have been proposed in the literature [67, 68].

Let $\mathscr{D}$ be the space of persistence diagrams, that is, the space of finite multisets of points within $\bar{\mathbb{R}}^2$. Let $\mathscr{F}$ be a collection of functions, $f : \Omega \to \mathbb{R}$ for all $f \in \mathscr{F}$, Ω being a compact space. A functional summary is in full generality any map from the space of persistence diagrams to a collection of functions, $F : \mathscr{D} \to \mathscr{F}$. In this work, $\mathscr{F}$ is the space of distributions on $\Omega = [0, c]$ for some $c > 0$, the space of simple functions on $\Omega = [0, c]$, or, trivially, $\mathbb{R}$.

By means of a functional summary F, random diagrams $D_1, \ldots, D_n$ become random functions, $F_i := F(D_i)$, $i = 1, \ldots, n$. If these random diagrams are sampled from a single distribution, then the corresponding functional summaries also origin from a single distribution (of functions), $\mathcal{P}_F$.

The population mean functional summary is a function

$$\bar{F}(s) = \mathbb{E}[F_i(s)] \qquad \forall\, s \in \Omega, \tag{3.34}$$

the expectation being with respect to $\mathcal{P}_F$. The sample estimator may be the pointwise estimator

$$\hat{F}_n(s) = \frac{1}{n} \sum_{i=1}^{n} F_i(s) \qquad \forall\, s \in \Omega. \tag{3.35}$$

Let $\mathcal{B}_F$ be the set of functions formed by a given functional summary. Let T be a compact set, such that we are interested in the population mean functional summary $\bar{F}(s)$ within $s \in T$. For every $F \in \mathcal{B}_F$ we define $F(s) = 0$ for all $s \notin T$. Throughout this manuscript, functional summaries shall be uniformly bounded from above by a constant $U < \infty$, that is,

$$\sup_{F \in \mathcal{B}_F} \sup_{s \in T} |F(s)| \leq U. \tag{3.36}$$

In Ref. [68] the following proposition on pointwise convergence of the estimator $\hat{F}_n$ towards $\bar{F}$ has been proven.

Proposition 1 (Pointwise Convergence). *Let F be a uniformly bounded functional summary. If $\mathcal{B}_F$ is equicontinuous, then*

$$\sup_{s \in T} |\hat{F}_n(s) - \bar{F}(s)| \xrightarrow{a.s.} 0. \qquad (3.37)$$

As a special case consider only L-Lipschitz functions constituting $\mathcal{B}_F$. Then the assumptions of this proposition are fulfilled and pointwise convergence follows.

Furthermore, a whole variety of statistically useful properties of functional summaries has been derived in Ref. [68] including, inter alia, a central limit theorem, statements about confidence bands and statistical tests.

Examples for functional summaries include, for example, persistence landscapes as introduced in Ref. [67], which are an equivalent description to barcodes and persistence diagrams, containing all their information.

Chapter 4

Persistent homology on a computer

This chapter serves as an introduction to numerically computing persistent homology properties on a computer. We first describe the basic algorithm based on matrix reduction in Sec. 4.1, more sophisticated variants of which are used throughout numerical libraries. Subsequently, the henceforth employed numerical implementation is illustrated and discussed in Sec. 4.2, followed by example results for both the Poisson point process and the Soneira-Peebles model. Both of these point cloud generation processes will be described in sufficient detail in Secs. 4.3 and 4.4.

4.1 Algorithmic basics

In this section we describe the basic, efficient algorithm to compute persistent homology on a computer, following the lines of Ref. [27]. It basically is a variant of matrix reduction. We restrict our discussion to alpha complexes of a point cloud $X \subset \mathbb{R}^d$. Let Rad : $\mathrm{Del}(X) \to [0, \infty)$ be the Delaunay radius function, having the property that $\mathrm{Rad}(\sigma_i) \leq \mathrm{Rad}(\sigma_j)$ if σ_i is a face of σ_j.

We use a compatible ordering of the simplices in $\mathrm{Del}(X)$, that is, a sequence $\sigma_1, \ldots, \sigma_m$ such that $\mathrm{Rad}(\sigma_i) \leq \mathrm{Rad}(\sigma_j)$ implies $i \leq j$ and so does σ_i being a face of σ_j. Such an ordering exists because Rad is monotonic. It is important to note that every initial subsequence of simplices forms a subcomplex of $\mathrm{Del}(X)$. The sequence of simplices is used to set up the boundary matrix, ∂, storing the simplices of all dimensions in one object with the (i, j)-th entry defined as

$$\partial[i,j] := \begin{cases} 1 & \text{if } \sigma_i \text{ is a co-dimension one face of } \sigma_j, \\ 0 & \text{else.} \end{cases} \tag{4.1}$$

Intuitively, rows and columns of this matrix are ordered like the simplices in the total ordering and the boundary of a simplex is stored in its column.

Column operations are employed by the matrix reduction algorithm in order to reduce ∂ to another matrix R, which, similarly, contains only zeros and ones. Let $\text{low}(j)$ be the row index of the lowest one in column j. If the entire column is zero, then $\text{low}(j)$ is undefined. R is called *reduced*, if $\text{low}(j) \neq \text{low}(j_0)$ for all $j \neq j_0$ specifying two non-zero columns. The algorithm proceeds by adding columns from left to right, in order to reduce the matrix ∂.

```
R = ∂;
for  j = 1 to  m  do
    while there exists  j₀ < j  with  low(j₀) = low(j)  do
      add column  j₀  to column  j
    endwhile
  endfor.
```

Worst, the running time is cubic in the number of simplices present in $\text{Del}(X)$. To obtain the ranks of homology groups of $\text{Del}(X)$, let $\#\text{Zero}_p(R)$ be the number of zero-columns corresponding to p-simplices and $\#\text{Low}_p(R)$ the number of lowest ones in rows that correspond to p-simplices. Then, $\beta_p = \#\text{Zero}_p(R) - \#\text{Low}_p(R)$.

In addition, we can retrieve information on persistent homology groups of the alpha complexes of X from R. We first note that even though R is not unique the lowest ones are unique in the following sense. Define

$$r_R(i,j) = \text{rank}(R_i^j) - \text{rank}(R_{i+1}^j) + \text{rank}(R_{i+1}^{j-1}) - \text{rank}(R_i^{j-1}), \tag{4.2}$$

wherein R_i^j is the lower-left submatrix of R whose corner element is $R[i,j]$. Note that $\text{rank}(R_i^j) = \text{rank}(\partial_i^j)$. If $R[i,j]$ is a lowest one, then $r_R(i,j) = 1$. If $R[i,j]$ is not a lowest one, then $r_R(i,j) = 0$ as deduced in Ref. [27]. Since the ranks of the submatrices of R are the same as those of ∂, r_R is a characterization of the lowest ones which does not depend on the reduction process. To this end, the lowest ones of R are unique. On top, $i = \text{low}(j)$ if and only if $r_\partial(i,j) = 1$.

The previous discussion revealed that the lowest ones are not an artifact of the protocol employed for reduction. We can assert a clear meaning to them and begin by noting that column j reaches its final form at the end of the j-th iteration of the outer loop in the previously mentioned algorithm. Then, the reduced matrix for the complex consists of the first j simplices in the total ordering. Two cases are to be distinguished: the case with column j ending up zero and the case in which it has a lowest one. Let us assume that column j of R is zero. Then we may call σ_j positive, since its addition creates a new cycle, giving birth to a new homology class. Assuming that column j of R is non-zero,

we find that it stores the boundary of the chain accumulated in column j of matrix V, thus being a cycle. We call σ_j negative, because its addition results in the death of the homology class represented by column j. Following an argument given again in Ref. [27], it is born at the time the simplex of its lowest one, which is σ_i with $i = \text{low}(j)$, is added.

Summarizing, we find that (a_i, a_j) is a finite point in $\text{Dgm}_p(\text{Rad})$ if and only if $i = \text{low}(j)$ and σ_i is a simplex of dimension p. Then, σ_j is of dimension $p + 1$. We find $(a_i, \infty) \in \text{Dgm}_p(\text{Rad})$ if and only if column i is zero but row i does not contain a lowest one. To this end, the reduced matrix R can be used to compute persistent homology groups.

In practical applications, boundary matrices may become very large. To this end, efficient algorithmic representations of sparse boundary matrices are necessary and implemented in optimized algorithms and libraries such as GUDHI [23, 27, 69].

4.2   Numerical implementation

A variety of software exists designed to provide user-friendly and fast routines for the generation of simplicial complexes and the computation of persistent homology [23]. We employ the GUDHI library, which is a generic open source C++ library tailored to TDA and higher dimensional geometry understanding [69]. In particular, with the simplex tree structure [70] it offers a handy data structure to store simplicial complexes. GUDHI employs the extensive CGAL library [71] to compute alpha complexes and uses a sophisticated variant of the algorithm described in Sec. 4.1 to compute persistent homology groups.

Given a point cloud X, our routine to compute homology groups of the full filtration of alpha complexes of X proceeds as follows.

1. Compute the alpha complexes, stored as the Delaunay complex of X together with the radii of the simplices and additional information among them.

2. Initialize the filtration of alpha complexes.

3. Compute the persistence diagram of the filtration.

4. Compute various persistent homology descriptors such as Betti numbers.

To give a rough indication of the speed of this routine, on a standard laptop alpha complexes of point clouds with approximately 100,000 data points can be analyzed in a few minutes, including the computation of persistent homology groups of all dimensions. For an overview of the computational cost of different TDA implementations across software solutions we refer to Ref. [23].

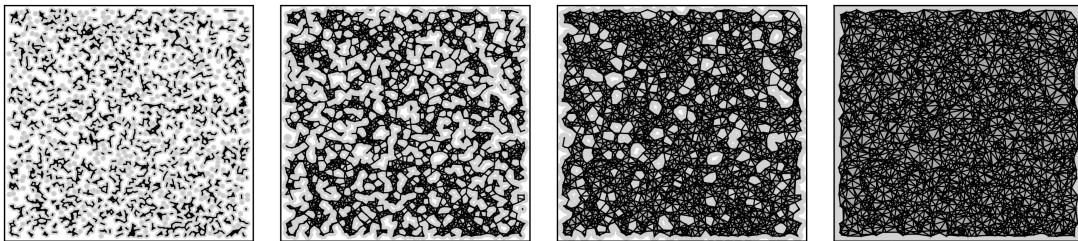## 4.3   Benchmarking via the Poisson point process

Figure 4.1: Alpha complexes of increasing radii from left to right, computed from a point cloud generated according to the Poisson point process with density $\rho = 0.05$ within a square of site-length 250 in arbitrary units. Analysis carried out using GUDHI.

As a first test of the aforementioned numerical implementation to compute persistent homology groups, we investigate the Poisson point process and corresponding alpha complexes. A finite point set $P \subset \mathbb{R}^d$ sampled from a *Poisson point process* with density $\rho > 0$ can be characterized by the following two properties:

1. the numbers of points sampled within a finite collection of pairwise disjoint Borel sets are independent random variables,

2. the expected number of points sampled within a Borel set $B \subset \mathbb{R}^d$ is ρ times the Lebesgue measure of the set, $\mathbb{E}[|P \cap B|] = \rho||B||$.

The two conditions imply that the number of points sampled in a Borel set B has a Poisson distribution with parameter $\rho||B||$. In particular, the probability of having no point in B is $\mathbb{P}[P \cap B = \emptyset] = \exp(-\rho||B||)$. P being sampled from a Poisson point process, it is with probability 1 in general position [61].

In Fig. 4.1 we display alpha complexes of different radii computed for an example point cloud generated from the Poisson point process. One may notice that all simplices are visually randomly distributed, in addition to holes present in the complex. The corresponding persistence diagram and Betti number distributions are displayed in Fig. 4.2. Comparing with numerical experiments carried out for Poisson point process samples in Ref. [72], we find qualitative agreement between our results and their.

4.4   Fractality in the Soneira-Peebles model

Another interesting point cloud generation process is provided by the Soneira-Peebles model, originally introduced in Ref. [73] in order to simulate galaxy distributions and mimic the occurring random fractality.
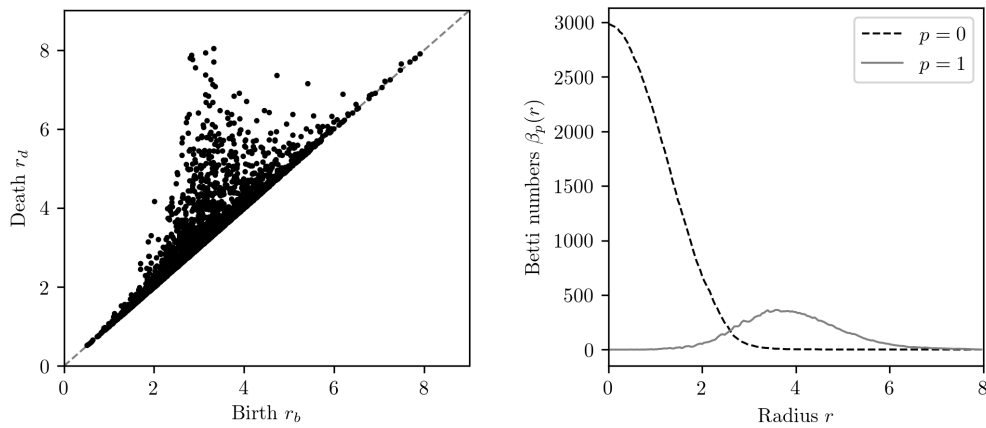
Figure 4.2: Left: Persistence diagram of one-dimensional homology classes computed from the sequence of alpha complexes of the example point cloud as in Fig. 4.1. Right: The corresponding Betti number distributions in dimensions zero and one. Analysis carried out using GUDHI.

Point clouds are inductively constructed in the Soneira-Peebles model. Specify a number γ of clusters. For each cluster, at a random position specify a unit sphere. These we call level-0 spheres. In each such sphere, randomly place a number ψ of spheres, each having a radius $1/\zeta$. These spheres we call level-1 spheres. Inductively, in any level-n sphere place ψ spheres of radius $1/\psi^{n+1}$, forming level $n+1$. This procedure is carried out until a given level η is reached.
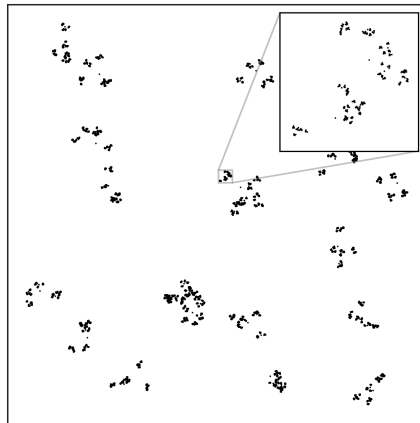

Figure 4.3: An example point cloud generated according to the Soneira-Peebles model with $\gamma = 20$ clusters and parameters $\eta = 4$, $\zeta = 5$ and $\psi = 5$.

In Fig. 4.3 we display an example point cloud generated according to the Soneira-Peebles model. Notice that already at the level of the single point cloud a clear indication
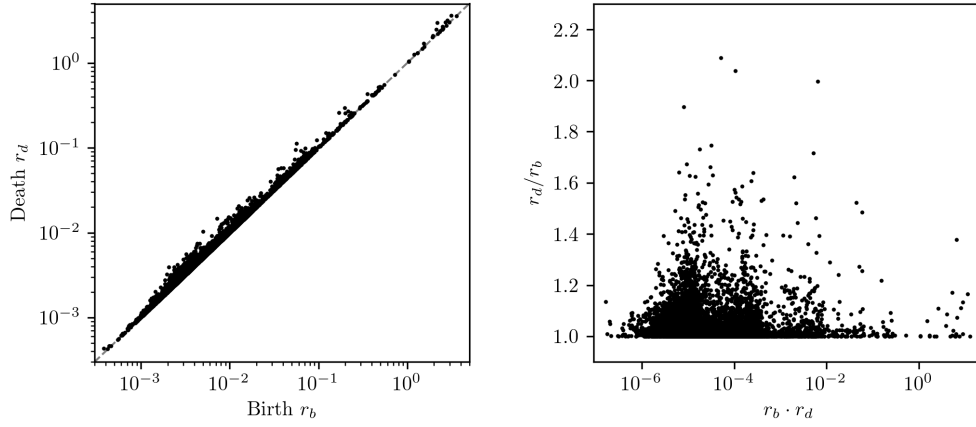
Figure 4.4: Left: Persistence diagram of one-dimensional homology classes computed from the sequence of alpha complexes of the example point cloud as in Fig. 4.3. Right: The same persistence diagram displayed in different coordinates. Analysis carried out using GUDHI.

of random fractality is visible. Zooming-in, we see that the point cloud structurally looks similar on comparably small length scales as compared to larger scales. Persistent homology as displayed in Fig. 4.4 clearly unveils this fractality. Multiple populations of persistent homology classes on different are visible length scales, in particular in $(r_b r_d, r_d/r_b)$-coordinates. By construction, on smaller scales there are more homology classes present than at larger length scales. Via the parameter ζ one can separate individual levels in the model further, providing a higher distinguishability of the populations on different length scales and controlling the random fractality in the model.
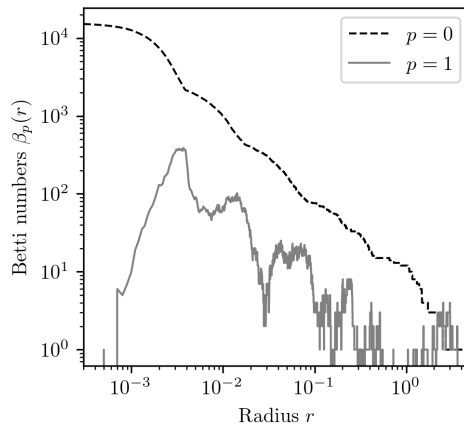

Figure 4.5: Betti numbers computed from the sequence of alpha complexes of the example point cloud as in Fig. 4.3. Analysis carried out using GUDHI.

As expected, corresponding Betti numbers as displayed in Fig. 4.5 reflect this effect, too. The Betti number distribution of zero-dimensional homology classes is already for the point cloud displayed in Fig. 4.3 quite smooth, displaying kink-like behavior between the occurring populations periodic in the radius r. The statistics of one-dimensional homology classes is worse, resulting in comparably large fluctuations. However, a clear pattern of peaks is visible, which reflect the model's fractality.

Chapter 5

Persistent homology observables

In this chapter we define a novel class of quantum field-theoretical observables, which for obvious reasons we call persistent homology observables. We focus on the classical-statistical approximation. To this end, we embed alpha complexes and their persistent homology into the classical-statistical approximation, in order to provide us with a quantitative means of connectivity and clustering structures beyond n-point correlation functions.

First, in Sec. 5.1 we describe a way of generating point clouds from individual field configurations in order to, subsequently, construct persistent homology observables by means of functional summaries, cf. Sec. 5.2. An interesting quantity to arise in a certain class of functional summaries is that of the asymptotic persistence pair distribution as defined in Sec. 5.3. We describe the prototype application of interest to us in Sec. 5.4: self-similar scaling as a manifestation of universality far from equilibrium, previously described in Chap. 2. A section on the lattice framework and its implications for persistent homology observables follows, cf. Sec. 5.5. Finally, we show that in the scaling ansatz to the asymptotic persistence pair distribution the occurring scaling exponents are linked to each other via a relation that stems from packing homology classes of finite size into a compact volume, cf. Sec. 5.6.

5.1 Point clouds in the classical-statistical framework via filtration functions

In the classical-statistical approximation we are given an ensemble of classical field configurations, each evolved in time according to the classical equation of motion as described in Sec. 2.3.3. An immense freedom of choice exists in constructing point clouds from individual field configurations, suitably by means of sub- or interlevel sets of a *filtration function*, that is, a map from a field configuration to $\mathbb{R}$. In this work, point clouds are generated as sublevel sets of the field amplitude on a finite spatial lattice Λ. Through

this, the lattice is crucial, rendering point clouds finite. For all filtration parameters, $\nu \in \mathbb{R}_+ = [0, \infty)$, we define

$$X_\nu(t) := |\psi(t, \cdot)|^{-1}[0, \nu] = \{\mathbf{x} \in \Lambda \,|\, |\psi(t, \mathbf{x})| \leq \nu\}, \qquad (5.1)$$

$\psi : \mathbb{R} \times \Lambda \to \mathbb{C}$ being a single field configuration as it appears, for example, in simulations of the nonrelativistic Bose gas, cf. Sec. 2.2.

Note that in the given approach, point clouds are constructed at each instance of time, t, individually. They do not incorporate field configurations at multiple instances of time, simultaneously. We want to emphasize, that this is nothing fundamental to the construction of persistent homology observables as carried out here. Various different paths to construct point clouds are amenable and the one presented is not the most general one. It is a mere choice that we make, providing a solid means of comparison with known results for example for occupation number spectra.

Simulating on a spatial square lattice with constant lattice spacing, we want to stress that to obtain point clouds by means of Eq. (5.1), to compute alpha complexes and to evaluate persistent homology groups only the finiteness of the lattice is crucial. Else, $X_\nu(t)$ might consist of infinitely many points. The construction of persistent homology groups is robust against perturbations of the lattice points due to stability theorems, cf. Sec. 3.3. This implies, that if points in $X_\nu(t)$ are altered slightly, then persistence diagrams of the sequence of alpha complexes of $X_\nu(t)$ change only slightly, too. This renders the microscopic form of the lattice irrelevant for later numerical persistent homology results. The constant lattice spacing and finite lattice volume solely amount to a smallest and a largest length scale amenable to the investigated real-time dynamics.

5.2   Observables via functional summaries

Inspired by Ref. [68], an important notion to play a role in this work is that of a functional summary, which is in full generality any map from the space of persistence diagrams to a collection of functions with domain Ω, $F : \mathscr{D} \to \mathscr{F}$, as described in Sec. 3.4.

As described in Sec. 2.3.3, in the classical-statistical approximation expectation values of quantum observables are computed as ensemble-averages of an observable's values computed from individual classical field configurations. We propose to proceed analogously for functional summaries of persistence diagrams computed from the sequence of alpha complexes of point clouds generated from individual field configurations. To this end, any functional summary may be evaluated on the level of individual field configurations and its expectation value computed as the ensemble-average. We assume that the range of validity of this approach coincides with the well-known classical-statistical regime. To motivate this, we infer the existence of a corresponding quantum operator $\mathcal{F}$,

such that in the classical-statistical approximation for all $s \in \Omega$,

$$\langle \mathcal{F}(\Lambda; \nu, p)(s) \rangle = \int \mathcal{D}\psi_0 \mathcal{D}\psi_0^* \, \mathcal{D}\pi_0 \mathcal{D}\pi_0^* \, W[\psi_0, \psi_0^*, \pi_0, \pi_0^*] \, F(\mathrm{Dgm}_p(|\psi_{\mathrm{cl}}(t, \cdot)|^{-1}[0, \nu]))(s),$$
(5.2)

where Λ specifies the employed spatial lattice and we use notation of Secs. 2.3.3 and 3.4. Nevertheless, we want to stress that the existence of such an operator is a priori not clear.

Key reason for dealing with functional summaries instead of persistence diagrams directly is that no unambiguous notion of the average of persistence diagrams exists [74]. This, however, would be a crucial ingredient of an evaluation scheme for persistent homology quantities in the classical-statistical approximation and, possibly, even in the context of general path-integral expressions.

In light of this, we need to assure that in the limit of averaging infinitely many individual functional summaries of field configurations the statistical mean of the functional summary is recovered. This is guaranteed for by Prop. 1 on the pointwise convergence of equicontinuous and uniformly bounded functional summaries, given in Sec. 3.4 of this work. For the sake of this statement we restrict our proposal to functional summaries of persistence diagrams with these two fairly general conditions and only consider functional summaries fulfilling these. Moreover, for such functional summaries a strong law of large numbers and a central limit theorem have been established [68].

In the classical-statistical framework, by means of the described evaluation scheme for expectation values of functional summaries in QFT, we refer to them as *persistent homology observables.*

5.3 The asymptotic persistence pair distribution

In this section we introduce the notion of a persistence pair distribution and its asymptotics, which we later use to introduce self-similarity of persistence diagrams.

Let $F : \mathscr{D} \to \mathscr{F}$ be a functional summary in the above sense. We say that F is *additive*, if $F(D + E) = F(D) + F(E)$ for any two persistence diagrams $D, E \in \mathscr{D}$. Here, $D + E$ denotes the sum of multisets, that is, the union of D and E with multiplicities of elements in both D and E added.

Let $D \in \mathscr{D}$ be a persistence diagram and F an additive functional summary. We then find for all $s \in \Omega$,

$$
\begin{aligned}
F(D)(s) &= \sum_{(r_b, r_d) \in D} F(\{(r_b, r_d)\})(s) \\
&= \int_0^\infty dr_b' \int_0^\infty dr_d' \, F(\{(r_b', r_d')\})(s) \, \mathcal{P}(r_b', r_d'),
\end{aligned}
$$
(5.3)

with the *persistence pair distribution*

$$\mathcal{P}(r_b', r_d') := \sum_{(r_b, r_d) \in D} \delta(r_b' - r_b)\, \delta(r_d' - r_d), \tag{5.4}$$

δ denoting the Dirac delta function.

Let $(D_i)_{i\in\mathbb{N}} \subset \mathscr{D}$ be an ensemble of persistence diagrams describing p-dimensional persistent homology classes. We denote the persistence pair distribution of D_i by $\mathcal{P}_i$. We define the *asymptotic persistence pair distribution* implicitly, requiring that for any functional summary F,

$$\int_0^\infty dr_b' \int_0^\infty dr_d'\, F(\{(r_b', r_d')\})(s)\, \bar{\mathcal{P}}(r_b', r_d')$$
$$:= \lim_{n\to\infty} \frac{1}{n} \sum_{i=1}^n \int_0^\infty dr_b' \int_0^\infty dr_d'\, F(\{(r_b', r_d')\})(s)\, \mathcal{P}_i(r_b', r_d'), \qquad \forall\, s \in \Omega. \tag{5.5}$$

Functional summaries of relevance in this work include the distribution of birth and death radii. Both can be computed as marginal distributions of $\bar{\mathcal{P}}$, respectively,

$$\bar{\mathcal{B}}(r_b) := \int_0^\infty dr_d\, \bar{\mathcal{P}}(r_b, r_d), \tag{5.6a}$$

$$\bar{\mathcal{D}}(r_d) := \int_0^\infty dr_b\, \bar{\mathcal{P}}(r_b, r_d). \tag{5.6b}$$

In addition, we define the persistence distribution, that is, the distribution of $r_d - r_b$, as

$$\bar{\Pi}(r) := \int_0^\infty dr_d\, \bar{\mathcal{P}}(r_d - r, r_d). \tag{5.7}$$

If $\bar{\mathcal{P}}(r_b, r_d)$ is the asymptotic persistence pair distribution of ℓ-dimensional homology classes, then the distribution of ℓ-th Betti numbers can be defined as

$$\bar{\beta}_\ell(r) := \int_0^r dr_b \int_r^\infty dr_d\, \bar{\mathcal{P}}(r_b, r_d). \tag{5.8}$$

A priori, the sets of functions $\bar{\mathcal{B}}(r_b)$, of $\bar{\mathcal{D}}(r_d)$, of $\bar{\Pi}(r)$ and of $\bar{\beta}_\ell(r)$ are not equicontinuous. For all $\sigma > 0$, define a Gaussian mollifier $\zeta_\sigma : \mathbb{R} \to \mathbb{R}_+$,

$$\zeta_\sigma(s) := \frac{1}{\sqrt{2\pi\sigma^2}} e^{-s^2/2\sigma^2}. \tag{5.9}$$

By convolution with a mollifier such as ζ_σ, the set of functions such as, for instance, $\bar{\beta}_\ell(r)$ can be rendered equicontinuous. Indeed, for any $\sigma > 0$ a constant $C_\sigma > 0$ exists, such

that for all possible functions $\bar{\beta}_\ell(r)$,

$$\frac{d}{dr}(\bar{\beta}_\ell * \zeta_\sigma)(r) = (\bar{\beta}_\ell * \zeta'_\sigma)(r) < C_\sigma, \tag{5.10}$$

the prime indicating taking the first derivative. Here we also employed that in the lattice framework all functions such as $\bar{\beta}_\ell(r)$ are uniformly bounded. In everything that follows we omit the convolution procedure in notations. Since numerically irrelevant, in the computations carried out in Sec. 6 no convolution procedure is applied and convergence of persistent homology observables is numerically verified, cf. Appendix A.

The average number of persistent homology classes is encoded in $\bar{\mathcal{P}}$,

$$n = \int_0^\infty dr_b \int_0^\infty dr_d\, \bar{\mathcal{P}}(r_b, r_d). \tag{5.11}$$

Various length scales may be constructed from $\bar{\mathcal{P}}$. Let $q > 0$. We define the notion of an average degree-q persistence length,

$$L_q := \left[\frac{1}{n} \int_0^\infty dr_b \int_0^\infty dr_d\, (r_d - r_b)^q\, \bar{\mathcal{P}}(r_b, r_d) \right]^{1/q}. \tag{5.12}$$

Another interesting length scale is the average maximum death radius, $\bar{r}_{d,\max}$. Following Eq. (5.53), which we will deduce later, it can be computed from the asymptotic persistence pair distribution via

$$\bar{r}_{d,\max} = \lim_{q \to \infty} \left(\int_0^\infty dr_b \int_0^\infty dr_d\, r_d^q\, \bar{\mathcal{P}}(r_b, r_d) \right)^{1/q}. \tag{5.13}$$

Analogously, the average maximum birth radius, $\bar{r}_{b,\max}$, can be defined.

These distributions and length scales all constitute additive functional summaries fulfilling the two aforementioned conditions for pointwise convergence. We thus consider them as valid persistent homology observables.

5.4 Self-similar scaling

As a prototype application, in this section we describe a self-similar scaling ansatz to the asymptotic persistence pair distribution. In Chap. 6 we will provide numerical evidence for that universal dynamics in persistent homology observables occurs and can actually be described by such a scaling ansatz.

We first describe the basic scaling approach, in order to move on by means of a heuristic argument for a packing relation among the occurring scaling exponents, which, in a later section, will be proven more rigorously under physically reasonable assumptions. We conclude this section with a discussion on why persistent homology scaling exponents

may reflect the self-similar scaling visible in correlation functions and vice versa.

5.4.1   The scaling ansatz

Let $\bar{\mathcal{P}}(t, r_b, r_d)$ be a time-dependent asymptotic persistence pair distribution. We say that $\bar{\mathcal{P}}(t, r_b, r_d)$ *scales self-similarly*, if exponents η_1, η_1' and η_2 exist, such that for all times t, t',

$$\bar{\mathcal{P}}(t, r_b, r_d) = (t/t')^{-\eta_2} \bar{\mathcal{P}}(t', (t/t')^{-\eta_1} r_b, (t/t')^{-\eta_1'} r_d). \tag{5.14}$$

Reflecting continuous "fractality", by the geometric meaning of self-similarity we would expect that $\eta_1 = \eta_1'$, such that birth and death radii blow up or shrink equally upon time-evolution. In Chap. 6 we will find numerical evidence for this.

By the time-dependence of $\bar{\mathcal{P}}$ derived geometric quantities become time-dependent, too. This we denote explicitly from now on. We find the following scaling behavior of birth and death radii distributions,

$$\bar{\mathcal{B}}(t, r_b) = (t/t')^{\eta_1' - \eta_2} \bar{\mathcal{B}}(t', (t/t')^{-\eta_1} r_b), \tag{5.15a}$$

$$\bar{\mathcal{D}}(t, r_d) = (t/t')^{\eta_1 - \eta_2} \bar{\mathcal{D}}(t', (t/t')^{-\eta_1'} r_d). \tag{5.15b}$$

Assuming $\eta_1 = \eta_1'$, the persistence distribution scales as

$$\bar{\Pi}(t, r) = (t/t')^{\eta_1 - \eta_2} \bar{\Pi}(t', (t/t')^{-\eta_1} r). \tag{5.16}$$

The total number of persistence pairs scales as follows,

$$n(t) = (t/t')^{\eta_1 + \eta_1' - \eta_2} n(t'). \tag{5.17}$$

Assuming $\eta_1 = \eta_1'$, for all $q > 0$ the average degree-q persistence length scales as

$$L_q(t) = (t/t')^{\eta_1} L_q(t'). \tag{5.18}$$

Following Prop. 8 as given below and assuming that $\eta_1 = \eta_1'$, the average maximum death radius scales as

$$\bar{r}_{d,\max}(t) = (t/t')^{\eta_1} \bar{r}_{d,\max}(t'). \tag{5.19}$$

Though not explicitly given here, the average maximum birth radius scales the same way.

This provides evidence for the geometric intuition of persistence length scales blowing up or shrinking in the course of time upon self-similar scaling, inferring the existence of a self-similarly scaling asymptotic persistence pair distribution.

Provided that $\eta_1 = \eta_1'$, the ℓ-th Betti numbers scale as

$$\beta_\ell(t, r) = (t/t')^{2\eta_1 - \eta_2} \beta_\ell(t', (t/t')^{-\eta_1} r). \tag{5.20}$$

5.4.2 A heuristic packing relation

We assume that $\eta_1 = \eta_1'$ in the given scaling ansatz. A heuristic argument can be given for that one can expect the relation $\eta_2 = (2 + d)\eta_1$ to hold, given that corresponding point clouds are restricted to a *constant* volume V. Intuitively, the argument encodes that only a finite number of persistent homology classes of a given size can be packed into V.

Let $q > 0$ and the point clouds be dominated by a time-dependent degree-q persistence length scale, $L_q(t)$. The d-dimensional volume V in which the point clouds reside is kept constant. Heuristically, a number $n_d(t)$ of d-dimensional persistent homology classes with persistence length scale $L_q(t)$ fits into V, scaling as

$$n_d(t) \sim \frac{V}{L_q(t)^d}, \tag{5.21}$$

since the volume that each d-dimensional persistent homology class occupies generically may scale as $\sim L_q(t)^d$. In the self-similar scaling ansatz, inserting Eq. (5.18) into Eq. (5.21) we find

$$n_d(t) \sim t^{-d\eta_1}. \tag{5.22}$$

On the other hand, from Eq. (5.17) we obtain

$$n_d(t) \sim t^{2\eta_1 - \eta_2}. \tag{5.23}$$

Hence,

$$\eta_2 = (2 + d)\eta_1. \tag{5.24}$$

This relation shows that persistent homology observables represent in a direct fashion the ambient space geometry. For correlation functions, contrastingly, similar relations are deduced from conserved quantities, such as $\alpha/\beta = d$ derived from the total number of quasi-particles in scalar theories being conserved, cf. Eq. (2.3).

Of course, the assignment of occupied volumes to d-dimensional homology classes is highly heuristic, bearing in mind that a homology class is an equivalence class of many cycles within a simplicial complex, rendering any such mapping ambiguous. However, one may use the Wasserstein stability theorem of persistence diagrams and elements of its proof [66] in order to deduce Eq. (5.24) more rigorously from physically reasonable assumptions. The corresponding slightly lengthy derivation is carried out in the following sections.

5.4.3 Relating persistent homology exponents to correlation function exponents

Typically, nonthermal fixed points and their properties are discussed in the framework of n-point correlation functions, both theoretically and experimentally [2,4,13,14,17,59]. The universal self-similar scaling behavior at nonthermal fixed points allows for a grouping of far-from-equilibrium quantum systems into universality classes. Universality classes cover broad classes of far-from-equilibrium initial conditions, large ranges of relevant parameters and even theories with very different degrees of freedom [4]. Being a natural surrounding for universality, properties of nonthermal fixed points including scaling exponents have been derived within the renormalization group [75,76]. To this end, length scales derived from scaling correlation functions are expected to blow up or to shrink with a unique power-law in time.

If the asymptotic persistence pair distribution shows self-similar scaling as in Eq. (5.14), then any length scale derived from it scales in time as a power-law with exponent η_1, assuming $\eta_1 = \eta_1'$. As an example consider the degree-q persistence length, defined in Eq. (5.12) and showing scaling as in Eq. (5.18). In light of this geometric analogy and the universality of scaling exponents at nonthermal fixed points, we expect that self-similar scaling behavior as extracted from correlation functions can typically be observed also in persistent homology observables. In Chap. 6 we will provide strong numerical evidence for this, in addition demonstrating that novel information can be deduced from persistent homology observables.

5.5 Lattice framework and ergodicity

With mathematical rigor we describe the lattice framework and certain properties of functional summaries for later usage. To this end, the reader may forgive us the reintroduction of for example the asymptotic persistence pair distribution in the course of this section. All of the occurring definitions originate from our own imagination.

We define the lattice framework such that point clouds are subsets of a d-dimensional uniform spatial lattice with periodic boundary conditions,

$$\Lambda_L := \{a(m_1, \ldots, m_d) \mid m_i \in \{0, \ldots, N-1\} \; \forall \, i\} \subset M, \qquad (5.25)$$

with $a := L/N$, lattice volume $\mathrm{vol}(\Lambda_L) = L^d$ and a number N^d of lattice sites. M is chosen to be the d-torus, $M = T^d$, constructed from a d-hypercube $[0, L]^d$, $L > 0$, by means of periodic boundary conditions. Birth and death radii of persistent homology classes are assumed to be small compared to L, such that constants $c, C > 0$ exist with $c/r^d \leq N(r) \leq C/r^d$. Here, $N(r)$ is defined to be the smallest triangulation with mesh

at most r as in Eq. (3.26). Points of a point cloud that lie not in general position are assumed to be slightly perturbed, in order to render $\mathrm{Del}(X)$ a simplicial complex.

Definition 8. Given the lattice framework, we say that a nested family of point clouds $(X_L)_{L>0}$, $X_L \subseteq \Lambda_L$ and $X_L \subseteq X_{L'}$ for each $L' > L > 0$, *distributes homogeneously*, if for each $\epsilon > 0$ and $\gamma \in [0,1]$ there exists an $L_{\epsilon,\gamma} > 0$, such that for all $L \geq L_{\epsilon,\gamma}$:

$$\left| \frac{\mathrm{card}(X_L \cap (a + R[0, \gamma L]^d))}{\mathrm{card}(X_L)} - \gamma^d \right| < \epsilon, \tag{5.26}$$

holds for arbitrary $a \in [0, L]^d, R \in SO(d)$ with

$$a + R[0, \gamma L]^d := \{a + Rx \mid x \in [0, \gamma L]^d\}, \tag{5.27}$$

taking periodic boundary conditions into account in order to make sense of this expression on the lattice Λ_L.

Example. Two counterexamples can provide intuition for Definition 8.

(i) For all $L > 0$, define $X_L := \{0\}$ ($0 \in \Lambda_l$ for all $L > 0$). This clearly violates the conditions of Definition 8. Point clouds that distribute homogeneously continuously occupy more and more points in a lattice of growing size.

(ii) Let $d = 1$ and define $X_L := \{n^2 \mid n \in \mathbb{N}\} \cap [0, L]$ for all $L > 0$. The points do not distribute homogeneously, since

$$\mathrm{card}(X_L \cap [0, L/2]) = \lfloor \sqrt{L/2} \rfloor, \tag{5.28a}$$

$$\mathrm{card}(X_L \cap [L/2, L]) = \lfloor \sqrt{L} \rfloor - \lfloor \sqrt{L/2} \rfloor. \tag{5.28b}$$

Let $X \subset \mathbb{R}^d$ be a point cloud. The persistence diagram of the filtration of alpha complexes of X is denoted in this section by $\mathrm{Dgm}_\ell^{(\alpha)}(X)$, $\ell = 0, \ldots, d$ and is defined, again, as the multiset of all birth-death pairs of ℓ-dimensional persistent homology classes along the filtration of alpha complexes.

Analogously to the homogeneous distribution of point clouds, we define the property of homogeneous distribution for persistence diagrams computed from a family of point clouds on the lattice.

Definition 9. Given the lattice framework, let $(X_L)_{L>0}$ be a nested family of point clouds, $X_L \subseteq \Lambda_L$ and $X_L \subseteq X_{L'}$ for each $L' > L > 0$. Define $D_L := \bigcup_{\ell=0}^d \mathrm{Dgm}_\ell^{(\alpha)}(X_L)$ for all $L > 0$. We say that the family $(D_L)_L$ *distributes homogeneously*, if for all $\gamma \in [0,1]$ and $\epsilon > 0$ there exists $L_{\gamma,\epsilon} > 0$, such that for all $L \geq L_{\gamma,\epsilon}$, $a \in [0, L]^d$ and $R \in SO(d)$,

$$\left| \frac{n(X_L \cap (a + R[0, \gamma L]^d))}{n(X_L)} - \gamma^d \right| < \epsilon. \tag{5.29}$$

Proposition 2. *Given the lattice framework, let $(X_L)_{L>0}$ be a nested family of point clouds that distributes homogeneously. Asymptotically, we assume that*

$$\text{card}(\text{Del}(X)) = \mathcal{O}(\text{card}(X)) \tag{5.30}$$

for all $X := X_{L'} \cap (a + R[0, L]^d)$ with $a \in [0, L']^d$, $R \in SO(d)$, $L' > L > 0$. Then, $(\bigcup_{\ell=0}^{d} \text{Dgm}_\ell^{(\alpha)}(X_L))_L$ distributes homogeneously.

Proof. Let $L' > L > 0$ be sufficiently large in all that follows and $a \in [0, L']^d$, $R \in SO(d)$. We assume the setting of the Proposition and note that the overall number of persistent homology classes of a point cloud $X_{L',L} := X_{L'} \cap (a + R[0, L]^d)$, $n(X)$, is bounded from above by the dimension of the chain complex interpreted as a $\mathbb{Z}_2$-vector space,

$$n(X_{L',L}) \leq \sum_{\ell=0}^{d} \dim_{\mathbb{Z}_2}(C_\ell(\text{Del}(X_{L',L})))$$
$$= \text{card}(\text{Del}(X_{L',L})). \tag{5.31}$$

From $\text{card}(\text{Del}(X_{L',L})) = \mathcal{O}(\text{card}(X_{L',L}))$ it follows that $n(X_{L',L}) = \mathcal{O}(\text{card}(X_{L',L}))$. On the other hand, since for the number of zero-dimensional persistent homology classes $n_0(X_{L',L}) = \text{card}(X_{L',L})$ holds, we obtain $\text{card}(X_{L',L}) \leq n(X_{L',L})$. To sum up, a constant $C' \geq 1$ exists, such that

$$\text{card}(X_{L',L}) \leq n(X_{L',L}) \leq C' \,\text{card}(X_{L',L}). \tag{5.32}$$

We assume that a $0 < q < 1$ and a $\tilde{C} > 0$ exists, such that $n(X) \leq \tilde{C}\text{card}(X_{L',L})^q$. Then, using Eq. (5.32) we obtain

$$\text{card}(X_{L',L})^{1-q} \leq \tilde{C}. \tag{5.33}$$

However, as we let $L, L' \to \infty$ with L'/L kept constant: $\text{card}(X_{L',L}) \to \infty$, such that the left-hand side of Eq. (5.33) blows up, resulting in a contradiction. Hence, a constant $c > 0$ exists, such that

$$\lim_{\substack{L,L' \to \infty, \\ L'/L = \text{const}}} \frac{n(X_{L',L})}{c\,\text{card}(X_{L',L})} = 1. \tag{5.34}$$

By the homogeneous distribution of point clouds, we obtain for sufficiently large $L' > L > 0$,

$$\text{card}(X_{L',L}) = (L/L')^d \,\text{card}(X_{L',L'}), \tag{5.35}$$

such that

$$\frac{n(X_{L',L})}{n(X_{L',L'})} = \left(\frac{L}{L'}\right)^d \frac{n(X_{L',L})}{c\,\text{card}(X_{L',L})} \frac{c\,\text{card}(X_{L',L'})}{n(X_{L',L'})}. \tag{5.36}$$

Letting $L, L' \to \infty$ with L'/L kept constant, we find

$$\lim_{\substack{L,L'\to\infty, \\ L'/L=\text{const}}} \frac{n(X_{L',L})}{n(X_{L',L'})} = \left(\frac{L}{L'}\right)^d. \tag{5.37}$$

This concludes the proof. □

Remark. Although not proven rigorously for point clouds that distribute homogeneously in the above sense, across the literature the property that $\text{card}(\text{Del}(X)) = \mathcal{O}(\text{card}(X))$ has been shown explicitly for different types of point clouds sampled from different spaces [77–81], motivating its usage here. Corresponding point cloud generation processes, for which this property has been shown, are similar in spirit to the homogeneous distribution defined here. A rigorous derivation might be feasible.

A key role in what follows is played, again, by functional summaries as defined in Ref. [68].

Definition 10. Given the lattice framework, we call a functional summary $F : \mathscr{D} \to \mathscr{F}$ *intensive*, if for any nested family of point clouds $(X_L)_{L>0}$ ($X_L \subseteq X_{L'} \subseteq \Lambda_{L'}$ for all $L' \geq L > 0$) which distributes homogeneously, with $D_L := \bigcup_{\ell=0}^d \text{Dgm}_\ell^{(\alpha)}(X_L)$, any $\epsilon > 0$ and any $L > 0$ sufficiently large:

$$\sup_{s\in\Omega} \left| \lim_{L'\to\infty} F(D_{L'})(s) - F(D_L)(s) \right| < \epsilon. \tag{5.38}$$

We denote the set of intensive functional summaries from $\mathscr{D}$ to $\mathscr{F}$ by $\mathscr{I}$.

The reader may recall that we say that a functional summary F is *additive*, if $F(D + E) = F(D) + F(E)$ for any two persistence diagrams $D, E \in \mathscr{D}$. Addition of persistence diagrams such as $D + E$ is defined by means of the sum of multisets, that is, the union of D and E with multiplicities of elements in both D and E added. The space of additive functional summaries from $\mathscr{D}$ to $\mathscr{F}$ is denoted by $\mathscr{A}$.

Proposition 3. *Given the lattice framework, let $(X_L)_{L>0}$ be a nested family of point clouds, distributed homogeneously with $X_L \subseteq \Lambda_L$ for each L. Assume furthermore, that $\text{card}(\text{Del}(X)) = \mathcal{O}(\text{card}(X))$ for all $X := X_{L'} \cap (a + R[0, L]^d)$ with $a \in [0, L']^d$, $R \in SO(d)$, $L' > L > 0$ sufficiently large. Let $A \in \mathscr{A}$ be an additive functional summary. Then, $A/\text{vol}(\Lambda_L)$, is almost surely an intensive functional summary for each L, if evaluated on persistence diagrams of point clouds $X_L \subseteq \Lambda_L$.*

Proof. For all $L > 0$ we denote $D_L := \bigcup_{\ell=0}^d \text{Dgm}_\ell^{(\alpha)}(X_L)$. Let $L, L' > 0$. We proceed by

estimating, letting $s \in \Omega$,

$$
\begin{aligned}
&\left| \frac{1}{\mathrm{vol}(\Lambda_{L'})} A(D_L')(s) - \frac{1}{\mathrm{vol}(\Lambda_L)} A(D_L)(s) \right| \\
&\quad = \frac{1}{\mathrm{vol}(\Lambda_L)} \left| \left(\frac{\mathrm{vol}(\Lambda_L)}{\mathrm{vol}(\Lambda_{L'})} - \frac{n(X_L)}{n(X_{L'})} \right) A(D_{L'})(s) - \left(1 - \frac{n(X_L)}{n(X_{L'})} \frac{A(D_{L'})(s)}{A(D_L)(s)} \right) A(D_L)(s) \right| \\
&\quad \leq \frac{1}{\mathrm{vol}(\Lambda_L)} \left| \frac{\mathrm{vol}(\Lambda_L)}{\mathrm{vol}(\Lambda_{L'})} - \frac{n(X_L)}{n(X_{L'})} \right| |A(D_{L'})(s)| + \frac{n(X_L)}{\mathrm{vol}(\Lambda_L)} \left| \frac{A(D_L)(s)}{n(X_L)} - \frac{A(D_{L'})(s)}{n(X_{L'})} \right|.
\end{aligned}
\tag{5.39}
$$

Since in our setting every functional summary is uniformly bounded, a constant $U < \infty$ exists, such that for any persistence diagram D_L,

$$
\sup_{s \in \Omega} |A(D_L)(s)| < U.
\tag{5.40}
$$

Let $\epsilon > 0$. Using Prop. 2, we find that $(D_L)_L$ distributes homogeneously. To this end, if L, L' are chosen sufficiently large, then

$$
\left| \frac{\mathrm{vol}(\Lambda_L)}{\mathrm{vol}(\Lambda_{L'})} - \frac{n(X_L)}{n(X_{L'})} \right| < \frac{\epsilon \, \mathrm{vol}(\Lambda_L)}{2U}.
\tag{5.41}
$$

In addition, Prop. 1 on pointwise convergence holds, since all functional summaries considered in this work are uniformly bounded and equicontinuous. Thus, provided L, L' are sufficiently large, we almost surely find

$$
\begin{aligned}
\left| \frac{A(D_L)(s)}{n(X_L)} - \frac{A(D_{L'})(s)}{n(X_{L'})} \right| &= \left| \frac{1}{n(X_L)} \sum_{x \in D_L} A(\{x\})(s) - \frac{1}{n(X_{L'})} \sum_{x \in D_{L'}} A(\{x\})(s) \right| \\
&< \frac{\epsilon \, \mathrm{vol}(\Lambda_L)}{2n(X_L)}.
\end{aligned}
\tag{5.42}
$$

Choosing L, L' sufficiently large, such that Eqs. (5.41) and (5.42) are valid, we can estimate Eq. (5.39) further,

$$
\left| \frac{1}{\mathrm{vol}(\Lambda_{L'})} A(D_L')(s) - \frac{1}{\mathrm{vol}(\Lambda_L)} A(D_L)(s) \right| < \frac{\epsilon \, |A(D_{L'})(s)|}{2U} + \frac{\epsilon}{2} < \epsilon.
\tag{5.43}
$$

Indeed, A almost surely constitutes an intensive functional summary.   □

A property to exploit later is ergodicity in the sense that for intensive functional summaries asymptotically the ensemble-average can be replaced by the infinite-volume limit.

Definition 11. Let $(X_{L,i})_{L>0, i \in \mathbb{N}}$ be a family of ensembles of point clouds. Define $D_{L,i} := \bigcup_{\ell=0}^{d} \mathrm{Dgm}_\ell^{(\alpha)}(X_{L,i})$ for all $i \in \mathbb{N}, L > 0$. Let $j \in \mathbb{N}$ be arbitrary. We say that the

family $(X_{L,i})_{L,i}$ *reflects ergodicity*, if for any $j \in \mathbb{N}$ the following conditions hold,

(i) $(X_{L,j})_L$ distributes homogeneously,

(ii) $\mathrm{card}(\mathrm{Del}(X)) = \mathcal{O}(\mathrm{card}(X))$ for all $X := X_{L'} \cap (a + R[0, L]^d)$ with $a \in [0, L']^d$, $R \in SO(d)$, $L' > L > 0$ sufficiently large,

(iii) given any $\epsilon > 0$, for each intensive functional summaries $F \in \mathscr{I}$ there exists an $L_{F,\epsilon} > 0$, such that for all $L \geq L_{F,\epsilon}$,

$$\sup_{s \in \Omega} \left| \lim_{L' \to \infty} F\Big(\bigcup_{\ell=0}^{d} D_{L',j,\ell}\Big)(s) - \lim_{n \to \infty} \frac{1}{n} \sum_{i=1}^{n} F\Big(\bigcup_{\ell=0}^{d} D_{L,i,\ell}\Big)(s) \right| < \epsilon. \qquad (5.44)$$

Remark. Following Prop. 3, given ensembles of point clouds that reflect ergodicity and given an additive functional summary $A \in \mathscr{A}$, the reflection of ergodicity almost surely yields that for any $\epsilon > 0$ an $L_{A,\epsilon} > 0$ exists, such that for all $L \geq L_{A,\epsilon}$ and all $j \in \mathbb{N}$,

$$\sup_{s \in \Omega} \left| \lim_{L' \to \infty} \frac{1}{\mathrm{vol}(\Lambda_{L'})} \sum_{\ell=0}^{d} A(D_{L',j,\ell})(s) - \lim_{n \to \infty} \frac{1}{n \, \mathrm{vol}(\Lambda_L)} \sum_{i=1}^{n} \sum_{\ell=0}^{d} A(D_{L,i,\ell})(s) \right| < \epsilon, \quad (5.45)$$

that is, asymptotically, the infinite-volume limit can be replaced by the ensemble-average of point clouds in particular for this type of functional summaries.

A crucial object in what follows is the asymptotic persistence pair distribution, which we reintroduce here in the given setting.

Definition 12. Let $(D_{i,\ell})_{i \in \mathbb{N}, \ell=0,\dots,d} \subset \mathscr{D}$ be an ensemble of persistence diagrams, one for each dimension ℓ. Using Dirac delta functions, for each diagram we define its *persistence pair distribution*,

$$\mathcal{P}_{i,\ell}(r_b', r_d') := \sum_{(r_d, r_b) \in D_{i,\ell}} \delta(r_b' - r_b)\, \delta(r_d' - r_d), \qquad\qquad \forall\, r_b', r_d' \in [0, \infty). \qquad (5.46)$$

We define the *ℓ-th asymptotic persistence pair distribution*, $\bar{\mathcal{P}}_\ell$, implicitly, requiring that for any functional summary $F : \mathscr{D} \to \mathscr{F}$,

$$\int_0^\infty dr_b' \int_0^\infty dr_d'\, F(\{(r_b', r_d')\})(s)\, \bar{\mathcal{P}}_\ell(r_b', r_d')$$

$$:= \lim_{n \to \infty} \frac{1}{n} \sum_{i=1}^{n} \int_0^\infty dr_b' \int_0^\infty dr_d'\, F(\{(r_b', r_d')\})(s)\, \mathcal{P}_{i,\ell}(r_b', r_d'), \qquad \forall\, s \in \Omega. \quad (5.47)$$

Definition 13. Let $(\bar{\mathcal{P}}_\ell(t))_{\ell=0,\ldots,d,\,t\in\mathbb{R}}$ be a family of asymptotic persistence pair distributions. We define the *average number of persistent homology classes* as

$$n(t) := \sum_{\ell=0}^{d} \int_0^\infty dr_b \int_0^\infty dr_d \,\bar{\mathcal{P}}_\ell(t)(r_b, r_d) \qquad\qquad \forall\, t \in \mathbb{R}. \qquad (5.48)$$

Let $q \geq 1$. The *average degree-q persistence length* is defined as

$$L_q(t) := \left[\frac{1}{n(t)} \sum_{\ell=0}^{\min\{\lfloor q\rfloor,d\}} \int_0^\infty dr_b \int_0^\infty dr_d \,(r_d - r_b)^q \,\bar{\mathcal{P}}_\ell(t)(r_b, r_d)\right]^{1/q}. \qquad (5.49)$$

For each ℓ and t, let $(D_{i,\ell}(t))_{i\in\mathbb{N}} \subset \mathscr{D}$ be the ensemble of persistence diagrams, from which the asymptotic persistence pair distribution $\bar{\mathcal{P}}_\ell(t)$ is computed. We define the *average maximum death radius* as

$$r_{d,\max}(t) := \lim_{n\to\infty} \frac{1}{n} \sum_{i=1}^{n} \max\left\{r_d \,\big|\, (r_b, r_d) \in D_{i,\ell}(t), \ell = 0,\ldots,d\right\}. \qquad (5.50)$$

Remark. In the lattice framework all three quantities introduced in the previous definition are well-defined functional summaries, in particular homogeneously bounded and trivially equicontinuous.

Proposition 4. *Given the lattice framework, let $(\bar{\mathcal{P}}_{L,\ell}(t))_{L>0,\ell=0,\ldots,d,\,t\in\mathbb{R}}$ be a family of asymptotic persistence pair distributions. For each $L > 0$ and $t \in \mathbb{R}$, let $(X_{L,i}(t))_{i\in\mathbb{N}} \subseteq \Lambda_L$ be an ensemble of nested point clouds, from which the asymptotic persistence pair distributions $(\bar{\mathcal{P}}_{L,\ell}(t))_\ell$ can be computed. For each $t \in \mathbb{R}$, $(X_{L,i}(t))_{L,i} \subseteq \Lambda_L$ shall reflect ergodicity. Then, almost surely the average maximum death radius is independent from the choice of an ensemble of point clouds corresponding to the asymptotic persistence pair distributions.*

Proof. Choose an arbitrary $t \in \mathbb{R}$. Define $D_{L,i,\ell}(t) := \mathrm{Dgm}_\ell^{(\alpha)}\big(X_{L,i}(t)\big)$ for all L, i, ℓ. Let $\mathcal{P}_{L,i,\ell}(t)$ be the persistence pair distribution computed from $D_{L,i,\ell}(t)$, $\mathcal{P}_{L,\ell}(t)$ its asymptotic distribution in the sense of Eq. (12). We make use of the identity

$$\max\left\{r_d \,\big|\, (r_b, r_d) \in D_{L,i,\ell}(t), \ell = 0,\ldots,d\right\} = \lim_{p\to\infty} \left(\sum_{\ell=0}^{d} \sum_{(r_b,r_d)\in D_{L,i,\ell}(t)} r_d^p\right)^{1/p}, \qquad (5.51)$$

which is a general result for p-norms in finite dimensions. In the lattice framework the

right-hand side of this equation is bounded from above. We note that for all p

$$\frac{1}{\mathrm{vol}(\Lambda_L)^{1/p}}\left(\sum_{\ell=0}^{d}\sum_{(r_b,r_d)\in D_{L,i,\ell}(t)} r_d^p\right)^{1/p} \tag{5.52}$$

is almost surely an intensive functional summary, employing Prop. 3. Let $\epsilon > 0$ and $L > 0$ be sufficiently large in the sense of Def. 11, applied twice in the following computation. Then, $\xi, \xi' \in \mathbb{R}$ with $|\xi|, |\xi'| < \epsilon$ exist, such that almost surely for any $j \in \mathbb{N}$:

$$\begin{aligned}
r_{d,\max}(t) &= \lim_{p\to\infty}\mathrm{vol}(\Lambda_L)^{1/p}\lim_{n\to\infty}\frac{1}{n}\sum_{i=1}^{n}\frac{1}{\mathrm{vol}(\Lambda_L)^{1/p}}\left(\sum_{\ell=0}^{d}\sum_{(r_b,r_d)\in D_{L,i,\ell}(t)} r_d^p\right)^{1/p} \\
&= \lim_{p\to\infty}\mathrm{vol}(\Lambda_L)^{1/p}\left(\lim_{L'\to\infty}\frac{1}{\mathrm{vol}(\Lambda_{L'})}\sum_{\ell=0}^{d}\sum_{(r_b,r_d)\in D_{L',j,\ell}(t)} r_d^p\right)^{1/p} + \xi \\
&= \lim_{p\to\infty}\left(\sum_{\ell=0}^{d}\int_0^\infty dr_b\int_0^\infty dr_d\, r_d^p\,\bar{\mathcal{P}}_{L,\ell}(t)(r_b,r_d) + \xi'\right)^{1/p} + \xi.
\end{aligned} \tag{5.53}$$

Upon increasing L, $|\xi|$ and $|\xi'|$ can be rendered arbitrarily small. Thus, given a family of asymptotic persistence pair distributions, the average maximum death radius is almost surely independent from the choice of an ensemble of point clouds corresponding to the asymptotic persistence pair distributions. $\qquad\square$

5.6 A packing relation from bounded total persistence

In this section we deduce Eq. (5.24) more rigorously under physically reasonable assumptions and mathematically reveal, that it actually encodes a bound on packing a number of homology classes of finite size into a compact volume.

Using elements of the proof of the Wasserstein stability theorem [66] as presented in Sec. 3.3.2, in a packing lemma we first establish an upper bound on the number of persistence pairs, hinted at by H. Edelsbrunner. A consequence of the bounded number of persistence pairs is then a relation between appearing scaling exponents in a self-similar scaling ansatz to the asymptotic persistence pair distribution as defined previously.

5.6.1 The packing lemma

Wasserstein stability preliminaries and terminology

Throughout, let M be a connected, triangulable, compact metric space and $d: M \times M \to \mathbb{R}$ a metric. We assume that the size of the smallest triangulation $N(r)$ grows polynomially with one over the mesh to the power of d. We assume furthermore that $M \subset \mathbb{R}^d$. If not stated otherwise, notations are those used in Sec. 3.3.2.

Notation. Given a Lipschitz function $f : M \to \mathbb{R}$, sublevel sets are denoted by $M_a := f^{-1}(-\infty, a]$ for all $a \in \mathbb{R}$. For all $a \leq b$ we denote the homomorphism between homology groups induced by the inclusion $M_a \subseteq M_b$ by $\iota_\ell^{a,b} : H_\ell(M_a) \to H_\ell(M_b)$, $\ell = 0, \dots, d$. Homology groups are assumed to have values in $\mathbb{Z}_2$. The persistence diagram of f is denoted by $\mathrm{Dgm}_\ell(f)$, $\ell = 0, \dots, d$, filtering by the nested sequence of sublevel sets and is the multiset of all birth-death pairs of ℓ-dimensional persistent homology classes appearing in course of the filtration of sublevel sets. Throughout, persistence diagrams are defined modulo zero-persistence elements.

As a lemma we rephrase the intermediate result of Ref. [82] given in Eq. (3.30).

Lemma 4 (Bounded total persistence). Let $f : M \to \mathbb{R}$ be a tame Lipschitz function. Let the size of the smallest triangulation of M, $N(r)$, grow polynomially with one over the mesh, that is, constants C and μ exist, such that $N(r) \leq C/r^\mu$ for all $r > 0$. Then, for all $\varepsilon \geq 0$ and all $\delta > 0$ the following bound on the degree-$(\mu + \delta)$ total persistence of f holds,

$$\mathrm{Pers}_{\mu+\delta}(f, \varepsilon) \leq C \,\mathrm{Lip}(f)^\mu \mathrm{Amp}(f)^\delta \frac{\mu + 2\delta}{\delta}. \tag{5.54}$$

We define a family of persistence length scales, similar to those introduced in Sec. 5.3.

Definition 14. Let $X \subset M$ be a point cloud and $q \geq 1$. We compute the number of persistence pairs via

$$n(X) := \sum_{\ell=0}^{d} \mathrm{card}(\mathrm{Dgm}_\ell^{(\alpha)}(X)). \tag{5.55}$$

The *degree-q persistence length* is defined as

$$L_q(X) := \left[\frac{1}{n(X)} \sum_{\ell=0}^{\min\{\lfloor q \rfloor, d\}} \sum_{(r_b, r_d) \in \mathrm{Dgm}_\ell^{(\alpha)}(X)} (r_d - r_b)^q \right]^{1/q}, \tag{5.56}$$

where $\lfloor q \rfloor = \max\{k \in \mathbb{N} \mid k \leq q\}$.

Geometrical notions employed in this appendix include the following.

Definition 15. Let $X \subset \mathbb{R}^d$ be a point cloud. The circumcenter of the largest empty circumsphere of a simplex $\sigma \in \mathrm{Del}(X)$ is denoted by $c(\sigma)$. Given a simplex $\sigma \in \mathrm{Del}(X)$, $\dim(\sigma) = \ell$, its *barycenter* is defined as

$$b(\sigma) := \frac{1}{\ell + 1} \sum_{i=1}^{\ell+1} x_i, \tag{5.57}$$

the x_i being the vertices spanning σ.

Remark. By construction, $b(\sigma) \in \text{Conv}(\sigma)$ for all $\sigma \in \text{Del}(X)$. This is not necessarily the case for circumcenters: for instance, the circumcenter of any obtuse triangle in $\text{Del}(X)$ does not lie in the triangle's convex hull.

The packing lemma in dimension $d = 1$

Let $M \subset \mathbb{R}$ be a compact, connected and triangulable metric space.

Proposition 5. *Let $X \subset M$ be a point cloud. Then a tame Lipschitz function $f_X : M \to \mathbb{R}_+$ with $\text{Lip}(f_X) = 1$ exists, such that*

$$\text{Dgm}_0(f_X) = \text{Dgm}_0^{(\alpha)}(X). \tag{5.58}$$

Proof. Let $X = \{x_1, \ldots, x_m\}$. Without loss of generality, the x_i be ordered such that $x_i < x_j$ whenever $i < j$. One may define a function $f_X : M \to \mathbb{R}_+$ as follows. Set $f_X(X) := 0$. For all $y \in M$ with $y < x_1$, define $f_X(y) := 0$. Similarly, for all $y \in M$ with $y > x_m$, define $f_X(y) := 0$. For $x_i < y < x_{i+1}$, $i = 1, \ldots, m - 1$, define

$$f_X(y) := \begin{cases} y - x_i & \text{for } y \in (x_i, (x_i + x_{i+1})/2] \\ x_{i+1} - y & \text{for } y \in ((x_i + x_{i+1})/2, x_{i+1}) \end{cases} \tag{5.59}$$

Constructed this way, f_X is tame and Lipschitz with $\text{Lip}(f_X) = 1$. We find that sublevel sets, M_a, and geometric realizations of the alpha shapes, $|\text{Del}_a(X)|$, are by construction homotopy-equivalent for all $a \in \mathbb{R}$. This implies equal homology groups, $H_0(M_a) = H_0(\text{Del}_a(X))$ for all $a \in \mathbb{R}_+$. Hence, $\text{Dgm}_0(f_X) = \text{Dgm}_0^{(\alpha)}(X)$. $\qquad\square$

Remark. M itself being contractible by compact- and connectedness, $H_\ell(\text{Del}_a(X)) = 0$ for all $\ell \geq 1, a \in \mathbb{R}_+$. Thus, $\text{Dgm}_\ell(f_X) = \text{Dgm}_\ell^{(\alpha)}(X) = \emptyset$ for all $\ell \geq 1$.

By proposition 5 and the previous remark a simple corollary follows.

Corollary 1. *Let $X \subset M$ be a point cloud. Then*

$$L_1(X) = \frac{1}{n(X)} \sum_{(0, r_d) \in \text{Dgm}_0^{(\alpha)}(X)} r_d = \frac{1}{n(X)} \sum_{(0, r_d) \in \text{Dgm}_0(f_X)} r_d, \tag{5.60}$$

using that in the filtration of alpha shapes all zero-dimensional persistent homology classes are born at radius zero.

Proposition 6. *Let $X \subset M$ be a point cloud. Then, $W_1(f_X, 0) = n(X)L_1(X)/2$.*

Proof. Given a persistence pair $x = (0, r_d) \in \text{Dgm}_0(f_X)$, we note that for any $y = (r, r)$, $r \in \mathbb{R}_+$, the inequality $\|x - y\|_\infty \geq r_d/2$ holds. This bound is sharp, fulfilled by $y =$

$(r_d/2, r_d/2)$. Setting $\tilde{\gamma}_0((0, r_d)) := (r_d/2, r_d/2)$ for all $(0, r_d) \in \mathrm{Dgm}_0(f_X)$, a bijection $\tilde{\gamma}_0 : \mathrm{Dgm}_0(f_X) \to \mathrm{Dgm}_0(0)$ exists, such that

$$
\begin{aligned}
W_1(f_X, 0) &= \inf_{\gamma_0} \sum_{x \in \mathrm{Dgm}_0(f_X)} ||x - \gamma_0(x)||_\infty \\
&= \sum_{x \in \mathrm{Dgm}_0(f_X)} ||x - \tilde{\gamma}_0(x)||_\infty \\
&= \sum_{(0, r_d) \in \mathrm{Dgm}_0(f_X)} \frac{r_d}{2}.
\end{aligned} \tag{5.61}
$$

Employing Corollary 1, the degree-1 Wasserstein distance to the zero-function can be computed as

$$
W_1(f_X, 0) = \frac{1}{2} \sum_{(0, r_d) \in \mathrm{Dgm}_0^{(\alpha)}(X)} r_d = \frac{1}{2} n(X) L_1(X). \tag{5.62}
$$

$\square$

The final packing lemma in $d = 1$ follows easily.

Lemma 1 (Packing lemma for $d = 1$)**.** *Let $X \subset M$ be a point cloud. Then,*

$$
n(X) \le \frac{\lambda_1(M)}{L_1(M)}, \tag{5.63}
$$

$\lambda_1(M)$ *denoting the Lebesgue measure of M.*

Proof. $M \subset \mathbb{R}$ being compact and connected, it certainly has bounded degree-1 total persistence. Specifically, $\mathrm{Pers}_1(f) \le \lambda_1(M)/2$ for every tame $f : M \to \mathbb{R}$ with $\mathrm{Lip}(f) \le 1$. Here, we made use of the absence of one-dimensional persistent homology classes. Since the bound is sharp, in Theorem 2 $C_M = \lambda_1(M)/2$. We apply Theorem 2 to the pair $f = f_X$ and $g = 0$. To this end, $C = C_M$ and we obtain

$$
W_1(f_X, 0) = \frac{n(X) L_1(X)}{2} \le \frac{\lambda_1(M)}{2}. \tag{5.64}
$$

Upon reshuffling, this gives the desired inequality. $\square$

The packing lemma in dimension $d > 1$

In general dimension $d > 1$ two obstacles appear, compared to $d = 1$. Caution needs to be exercised for that the circumcenter of a simplex does not necessarily lie in its convex hull. Second, the Wasserstein stability theorem does not yield the desired inequality. Instead, we make use of Lemma 4.

Let $M \subset \mathbb{R}^d$ be a compact, convex and triangulable metric space of dimension d.

Proposition 7. *Let $X \subset M$ be a point cloud. Then a tame Lipschitz function $f_X : M \to \mathbb{R}_+$ exists, such that*

$$\mathrm{Dgm}_\ell(f_X) = \mathrm{Dgm}_\ell^{(\alpha)}(X) \qquad \forall\, \ell \geq 0. \tag{5.65}$$

Proof. The construction of a Lipschitz function $f_X : M \to \mathbb{R}_+$ is carried out inductively on geometric realizations of the skeletons of the Delaunay complex, understood as subsets of M, $f_X^{(k)} : |\mathrm{Del}(X)^{(k)}| \to \mathbb{R}_+$.

First, set $f_X^{(0)}(X) := 0$. Now, assume that $f_X^{(k)}$ has been constructed for some $k \geq 0$. Let $\sigma \in \mathrm{Del}(X)^{(k+1)}$ with $\dim(\sigma) = k+1$. First assume that $c(\sigma) \in \mathrm{Conv}(\sigma)$ and define

$$f_X^{(k+1)}(tz + (1-t)c(\sigma)) := t f_X^{(k)}(z) + (1-t)\mathrm{Rad}(\sigma),$$
$$\forall\, t \in [0,1],\ z \in \tau,\ \tau \text{ facet of } \sigma. \tag{5.66}$$

Thus, $f_X^{(k+1)}(c(\sigma)) = \mathrm{Rad}(\sigma)$. By means of this construction,

$$\mathrm{Lip}\left(f_X^{(k+1)}\big|_{\mathrm{Conv}(\sigma)}\right)$$
$$= \max\left\{1, \max\left\{\mathrm{Lip}\left(f_X^{(k)}\big|_{\mathrm{Conv}(\tau)}\right)\Big|\, \tau \text{ facet of } \sigma\right\}\right\}, \tag{5.67}$$

that is, the Lipschitz constant of $f_X^{(k+1)}\big|_{\mathrm{Conv}(\sigma)}$ does not increase compared to $f_X^{(k)}$. We repeat this definition for all $(k+1)$-simplices $\sigma \in \mathrm{Del}(X)^{(k+1)}$ with $c(\sigma) \in \mathrm{Conv}(\sigma)$. Otherwise, if $c(\sigma) \notin \mathrm{Conv}(\sigma)$, define

$$f_X^{(k+1)}(tz + (1-t)b(\sigma)) := t f_X^{(k)}(z) + (1-t)\mathrm{Rad}(\sigma),$$
$$\forall\, t \in [0,1],\ z \in \tau,\ \tau \text{ facet of } \sigma, \tag{5.68}$$

such that $f_X^{(k+1)}(b(\sigma)) = \mathrm{Rad}(\sigma)$. Herewith,

$$\mathrm{Lip}\left(f_X^{(k+1)}\big|_{\mathrm{Conv}(\sigma)}\right) = \max\left\{\max\left\{\frac{|\mathrm{Rad}(\sigma) - f_X^{(k)}(z)|}{|b(\sigma) - z|}\,\middle|\, z \in \mathrm{Conv}(\tau),\ \tau \text{ facet of } \sigma\right\},\right.$$
$$\left.\max\left\{\mathrm{Lip}\left(f_X^{(k)}\big|_{\mathrm{Conv}(\tau)}\right)\middle|\, \tau \text{ facet of } \sigma\right\}\right\}, \tag{5.69}$$

that is, the Lipschitz constant of $f_X^{(k+1)}\big|_{\mathrm{Conv}(\sigma)}$ may exceed $\mathrm{Lip}(f_X^{(k)})$ upon this construction. We repeat this construction for all $(k+1)$-simplices $\sigma \in \mathrm{Del}(X)^{(k+1)}$ with $c(\sigma) \notin \mathrm{Conv}(\sigma)$. Having carried out the construction for both types of simplices, $f_X^{(k+1)}$ is defined on all $|\mathrm{Del}(X)^{(k+1)}|$. Finally, we set $f_X\big|_{\mathrm{Conv}(\mathrm{Del}(X))} := f_X^{(d)}$ and define $f_X(z) := \min_{y \in X} d(y,z)$ for all $z \in M - \mathrm{Conv}(\mathrm{Del}(X))$. Clearly, $\mathrm{Lip}(f_X\big|_{M-\mathrm{Conv}(\mathrm{Del}(X))}) = 1$. Note that f_X is well-defined on all M. By construction, f_X is tame and Lipschitz with

$1 \leq \mathrm{Lip}(f_X) < \infty$.

Again, sublevel sets of f_X, M_a, and geometric realizations of the alpha shapes, $|\mathrm{Del}_a(X)|$ are homotopy-equivalent for all $a \in \mathbb{R}_+$. Hence, $H_\ell(M_a) = H_\ell(\mathrm{Del}_a(X))$ for all $a \in \mathbb{R}_+$, such that $\mathrm{Dgm}_\ell(f_X) = \mathrm{Dgm}_\ell^{(\alpha)}(X)$, both for all $\ell = 0, \ldots, d$, respectively.   □

Remark. Note that in general the function constructed in proposition 7 has a Lipschitz constant different from one, unlike the equivalent proposition 5 in one dimension.

We can directly formulate the packing lemma in general $d > 1$.

Lemma 2 (Packing lemma for $d > 1$)**.** *Assume that for M a constant $C > 0$ exists, such that $N(r) \leq C/r^d$ for all $r > 0$. Let $X \subset M$ be a point cloud. Set $r_{d,\max}(X) := \max\{r_d \,|\, (r_b, r_d) \in \mathrm{Dgm}_\ell(f_X), \ell = 0, \ldots, d\}$. Then,*

$$n(X) \leq \frac{C(d + 2\delta)}{\delta} \mathrm{Lip}(f_X)^d \, \frac{(r_{d,\max}(X))^\delta}{L_{d+\delta}(X)^{d+\delta}} \qquad \forall\, \delta > 0. \tag{5.70}$$

Proof. $N(r) \leq C/r^d$ for all $r > 0$ implies that for f_X lemma 4 holds. To this end, letting $\delta > 0$, it follows that

$$\mathrm{Pers}_{d+\delta}(f_X) = \mathrm{Pers}_{d+\delta}(f_X, 0)$$
$$\leq C \, \mathrm{Lip}(f_X)^d \mathrm{Amp}(f_X)^\delta \frac{d + 2\delta}{\delta}. \tag{5.71}$$

The left-hand side of this equation evaluates to $\mathrm{Pers}_{d+\delta}(f_X) = n(X)L_{d+\delta}(X)^{d+\delta}$. Additionally, $\mathrm{Amp}(f_X) = r_{d,\max}(X)$. The desired inequality follows.   □

5.6.2   Self-similar scaling exponents from packing

We first reintroduce self-similarity for a family of asymptotic persistence pair distributions of different dimensions, $\ell = 0, \ldots, d$.

Definition 16. Let $(\bar{\mathcal{P}}_\ell(t))_{\ell=0,\ldots,d,\, t \in \mathbb{R}}$ be a family of asymptotic persistence pair distributions. We say that $(\bar{\mathcal{P}}_\ell(t))_{\ell,t}$ *scales self-similarly with exponents* η_1, η_2, if for all $t, t' \in \mathbb{R}$ and for all $\ell = 0, \ldots, d$:

$$\bar{\mathcal{P}}_\ell\big(t\big)(r_b, r_d) = (t/t')^{-\eta_2} \, \bar{\mathcal{P}}_\ell\big(t'\big)((t/t')^{-\eta_1} r_b, (t/t')^{-\eta_1} r_d). \tag{5.72}$$

Proposition 8. *Let $(\bar{\mathcal{P}}_\ell(t))_{\ell=0,\ldots,d,\, t \in \mathbb{R}}$ be a family of asymptotic persistence pair distributions that scales self-similarly with exponents η_1, η_2. Then, for all $t, t' \in \mathbb{R}$ and $q \geq 1$,*

$$n(t) = (t/t')^{2\eta_1 - \eta_2} n(t'), \qquad L_q(t) = (t/t')^{\eta_1} L_q(t'). \tag{5.73}$$

Given the lattice framework and the existence of self-similarly scaling $\bar{\mathcal{P}}_\ell(t)$ as before, but for all sufficiently large lattice sizes, if the asymptotic persistence pair distributions stem from point clouds that reflect ergodicity, then we almost surely find:

$$r_{d,\max}(t) = (t/t')^{\eta_1} r_{d,\max}(t'). \tag{5.74}$$

Proof. Let $t, t' \in \mathbb{R}$. The derivations of the first two equations are clear from corresponding definitions. To obtain the third equation, we employ Eq. (5.53). Sufficient conditions for its validity are fulfilled, in particular the lattice framework and the reflection of ergodicity. In the limit of $L \to \infty$ we can ignore possible small deviations from the reflection of ergodicity, previously denoted by ξ and ξ'. Accordingly, we set $\xi = \xi' = 0$ and almost surely find

$$
\begin{aligned}
r_{d,\max}(t) &= \lim_{p\to\infty} \left(\sum_{\ell=0}^{d} \int_0^\infty dr_b \int_0^\infty dr_d \, r_d^p \, \bar{\mathcal{P}}_\ell(t)(r_b, r_d) \right)^{1/p} \\
&= \lim_{p\to\infty} \left((t/t')^{(p+2)\eta_1 - \eta_2} \sum_{\ell=0}^{d} \int_0^\infty dr_b' \int_0^\infty dr_d' \, r_d^p \, \bar{\mathcal{P}}_\ell(t')(r_b', r_d') \right)^{1/p} \\
&= \lim_{p\to\infty} (t/t')^{(1+2/p)\eta_1 - \eta_2/p} \left(\sum_{\ell=0}^{d} \int_0^\infty dr_b' \int_0^\infty dr_d' \, r_d^p \, \bar{\mathcal{P}}_\ell(t')(r_b', r_d') \right)^{1/p} \\
&= (t/t')^{\eta_1} r_{d,\max}(t'). \tag{5.75}
\end{aligned}
$$

$\square$

In order to apply the packing lemma, we first introduce a notion to simplify the treatment of the Lipschitz constant on ensembles of time-dependent point clouds.

Definition 17. Given the lattice framework, let $(X_i(t))_{i\in\mathbb{N}, t\in\mathbb{R}}$ be a family of ensembles of point clouds. Define $D_{i,\ell}(t) := \mathrm{Dgm}_\ell^{(\alpha)}(X_i(t))$ for all i, t and $\ell = 0, \ldots, d$. We say that $(X_i(t))_{i,t}$ has *time-independent Lipschitz constant upon averaging*, if a constant $\kappa > 0$ exists, such that for any $p > 0$, any intensive functional summary $F \in \mathscr{I}$ and all times $t \in \mathbb{R}$:

$$\lim_{n\to\infty} \frac{1}{n} \sum_{i=1}^{n} \mathrm{Lip}\big(f_{X_i(t)}\big)^p F(D_{i,\ell}(t)) = \kappa^p \lim_{n\to\infty} \frac{1}{n} \sum_{i=1}^{n} F(D_{i,\ell}(t)) \qquad \forall \ell = 0, \ldots, d. \tag{5.76}$$

Note. In the lattice framework, one may motivate this notion by that due to its construction, $\mathrm{Lip}\big(f_{X_i(t)}\big)$ is very sensitive to precise geometric arrangements of the points

in X. This can render $\mathrm{Lip}\big(f_{X_i(t)}\big)$ time-independent upon averaging in the above sense. Additionally, it is bounded from above on the lattice.

Finally, using the packing lemma we deduce a relation between exponents that appear in the self-similar scaling approach to the asymptotic persistence pair distribution.

Theorem 4. *Given the lattice framework, let $(\bar{\mathcal{P}}_{L,\ell}(t))_{L>0,\ell=0,\dots,d,\,t\in\mathbb{R}}$ be a family of asymptotic persistence pair distributions in dimension $d>1$. For each $L>0$, $\ell=0,\dots,d$ and $t\in\mathbb{R}$, let $(X_{L,i}(t))_{i\in\mathbb{N}}\subset\Lambda_L$ be an ensemble of nested point clouds from which the asymptotic persistence pair distributions $\bar{\mathcal{P}}_{L,\ell}(t)$ can be computed and which reflects ergodicity. For all $L>0$, $(X_{L,i}(t))_{i\in\mathbb{N},t\in\mathbb{R}}\subset\Lambda_L$ is assumed to have time-independent Lipschitz constant upon averaging. Let the whole family of asymptotic persistence pair distributions scale self-similarly with exponents η_1,η_2. Then, almost surely*

$$\eta_2 = (2+d)\eta_1. \tag{5.77}$$

Proof. Let $L>0$ be sufficiently large, such that ergodicity applies. Let $t\in\mathbb{R}$ and $\delta>0$. For all $i\in\mathbb{N}$, Lemma 2 yields the inequality

$$n_{X_{L,i}(t)} \leq \frac{C(d+2\delta)}{\delta}\mathrm{Lip}\big(f_{X_{L,i}(t)}\big)^d\,\frac{r_{d,\max}\big(X_{L,i}(t)\big)^\delta}{L_{d+\delta}\big(X_{L,i}(t)\big)^{d+\delta}}. \tag{5.78}$$

Upon averaging and exploiting that by time-independence of the Lipschitz constant upon averaging a corresponding constant $\kappa>0$ exists, we find

$$
\begin{aligned}
n_L(t) &:= \lim_{n\to\infty}\frac{1}{n}\sum_{i=1}^n n_{X_{L,i}(t)} \;\leq\; \frac{C(d+2\delta)}{\delta}\lim_{n\to\infty}\frac{1}{n}\sum_{i=1}^n \mathrm{Lip}\big(f_{X_{L,i}(t)}\big)^d\,\frac{r_{d,\max}\big(X_{L,i}(t)\big)^\delta}{L_{d+\delta}\big(X_{L,i}(t)\big)^{d+\delta}}\\
&= \frac{C(d+2\delta)}{\delta}\kappa^d\lim_{n\to\infty}\frac{1}{n}\sum_{i=1}^n \frac{r_{d,\max}\big(X_{L,i}(t)\big)^\delta}{L_{d+\delta}\big(X_{L,i}(t)\big)^{d+\delta}}.
\end{aligned}
\tag{5.79}
$$

Choose an arbitrary $j\in\mathbb{N}$. On the right-hand side of this inequality we can make use of ergodicity, since $r_{d,\max}$ and $L_{d+\delta}$ constitute intensive functional summaries on the point clouds of interest,

$$n_L(t) \leq \frac{C(d+2\delta)}{\delta}\kappa^d\lim_{L'\to\infty}\frac{r_{d,\max}\big(X_{L',j}(t)\big)^\delta}{L_{d+\delta}\big(X_{L',j}(t)\big)^{d+\delta}} = \frac{C(d+2\delta)}{\delta}\kappa^d\,\frac{r_{d,\max}(t)^d}{L_{d+\delta}(t)^{d+\delta}}. \tag{5.80}$$

Exploiting self-similarity, we almost surely find by Prop. 8,

$$\frac{r_{d,\max}(t)^d}{L_{d+\delta}(t)^{d+\delta}} = (t/t')^{-d\eta_1}\,\frac{r_{d,\max}(t')^d}{L_{d+\delta}(t')^{d+\delta}} \qquad \forall\,t,t'\in(T_0,T_1). \tag{5.81}$$

Hence, we almost surely find by means of Eq. (4),

$$(t/t')^{2\eta_1 - \eta_2} n_L(t') \leq (t/t')^{-d\eta_1} \frac{C(d + 2\delta)}{\delta} \kappa^d \frac{r_{d,\max}(t')^d}{L_{d+\delta}(t')^{d+\delta}} \qquad \forall\, t, t' \in (T_0, T_1). \qquad (5.82)$$

In the limit $t/t' \to \infty$ this implies $2\eta_1 - \eta_2 \leq -d\eta_1$. In the limit $t/t' \to 0$ this implies $2\eta_1 - \eta_2 \geq -d\eta_1$. The desired equality follows almost surely. $\qquad \square$

Remark. Under the same assumptions as in Theorem 4, dropping the time-independence of the Lipschitz constant upon averaging, in dimension $d = 1$ the same relation (5.77) between the two scaling exponents holds.

Chapter 6

Numerical testbed: The nonrelativistic Bose gas

As a numerical proof of principle of persistent homology observables' universality manifesting itself in a self-similar scaling evolution of the asymptotic persistence pair distribution, in this chapter we primarily investigate a multitude of geometric quantities derived from the latter at infrared nonthermal fixed points in the two-dimensional nonrelativistic Bose gas.

In Sec. 6.1 we first describe the numerical setup of simulations and the computation scheme for persistent homology observables. Occupation number results and their self-similar properties are given in Sec. 6.2, forming the basis for a comparison with persistent homology observables results such as birth and death radii distributions as provided subsequently, cf. Sec 6.3. The resulting self-similar scaling evolution of persistent homology observables requires a thorough discussion, since interestingly a continuous spectrum of scaling exponents is observed, depending on a filtration parameter, cf. Sec. 6.4. We argue for this phenomenon to indicate the mixing of two universal scaling species, the two being related to the different infrared nonthermal fixed points existing in the two-dimensional nonrelativistic Bose gas: the strong wave turbulence nonthermal fixed point and the anomalous vortex kinetics nonthermal fixed point. Basis for this is to infer that sound excitations in the bulk give rise to the strong wave turbulence nonthermal fixed point, strongly supported by analytic and numerical evidence [4, 46]. On top, the exponent spectrum slightly alters in the course of time due to amplitude redistribution effects as explained in Sec. 6.5. Investigating the distribution of persistences, one finds indications for a power-law behavior scaling with persistence, cf. Sec. 6.6. We conclude this chapter with a discussion of Betti numbers in Sec. 6.7, providing a consistency check for the deduced self-similar properties.
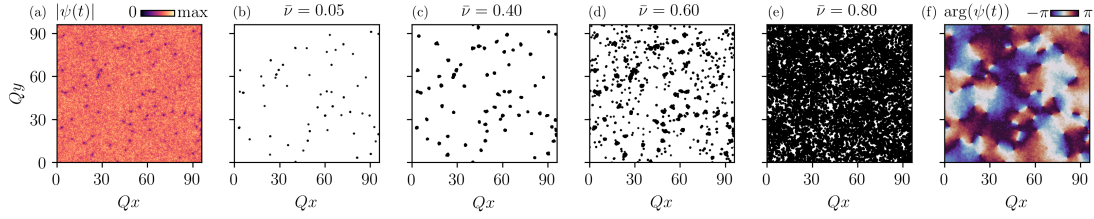
Figure 6.1: An example field configuration and corresponding point clouds in the vicinity of an IR nonthermal fixed point. Panel (a): Spatially-resolved amplitude of the field $\psi(t, \mathbf{x})$. From (b) to (e): Point clouds $X_\nu(t)$ for the different $\bar{\nu}$-values indicated. Panel (f): Spatially-resolved phase-values of the field $\psi(t, \mathbf{x})$. Simulation parameters are denoted in Sec. 6.1.1. Results are shown at simulation time $Qt = 3750$.

6.1 Numerical prerequisites

In this section we motivate numerical choices and provide details on the simulations and analyses of their results, in particular via persistent homology techniques.

6.1.1 Simulations via the Gross-Pitaevskii equation

The nonrelativistic Bose gas can be described by complex scalar fields, ψ, as discussed in detail in Sec. 2.2. We restrict applications to the overoccupied regime, in which the classical-statistical approximation as described in Sec. 2.3.3 is suitable [4]. Accordingly, at initial time an ensemble of classical field configurations with Gaussian fluctuations is generated, computing the subsequent dynamics of individual configurations via the Gross-Pitaevskii equation. Initially, for the Fourier-transformed statistical two-point correlation function an overoccupied box is chosen,

$$f(0, \mathbf{p}) = \frac{50}{2mgQ}\Theta(Q - |\mathbf{p}|), \tag{6.1}$$

with $m/Q = 8$ throughout this chapter and f as defined in Eq. (2.31). Outside the box, no 'quantum-half' is taken into account. At zero momentum, no initial condensate is set. Spatial coordinates are restricted to a square lattice, Λ, consisting of a regular grid of N^2 points within a volume L^2 with periodic boundary conditions. Throughout this work, the lattice spacing reads $Qa = 0.0625$, the number of lattice sites $N = 1536$.

As given in Eq. (5.1), point clouds $X_\nu(t) \subseteq \Lambda$ are defined as sublevel sets of amplitudes of individual field configurations to a given maximum value ν. The filtration parameter, ν, is described via the dimensionless quantity $\bar{\nu}$, defined as

$$\bar{\nu} := \nu/\langle|\psi(t = 0)|\rangle_{\text{vol}}, \tag{6.2}$$

with the volume-averaged initial amplitude

$$\langle |\psi(t=0)| \rangle_{\text{vol}} = \frac{1}{N^2} \sum_{\mathbf{x} \in \Lambda} |\psi(t=0, \mathbf{x})|. \tag{6.3}$$

In Fig. 6.1 amplitudes, a variety of corresponding point clouds and phases of a single field configuration ψ are displayed for a simulation time, at which the system is in the vicinity of a nonthermal fixed point. Clearly visible in point clouds are two components: points in the bulk and vortices. Having approximately zero amplitude at the center of their nuclei, vortices dominate the point clouds $X_\nu(t)$ for small values of ν. Increasing ν, points first accumulate around vortex nuclei but at moderately high values also occur in the bulk. The higher ν gets, the denser point clouds become, reducing the average distance between points. Due to this, evaluating alpha complexes and their persistent homology groups at different ν-values effectively probes the system on different length scales. Effects of all this will become clearly visible in Sec. 6.3.

6.1.2   Persistent homology pipeline and miscellanea

We apply GUDHI functions to point clouds generated from individual field configurations at different times as in Eq. (5.1), independently. Obtaining persistent homology outcomes at various times for each and every field configuration, ensemble-averages are taken. We average $n = 50$ configurations throughout this work. For that many configurations we have verified that the persistent homology observables $\bar{\mathcal{B}}_\ell(t, r_b)$, $\bar{\mathcal{D}}_\ell(t, r_d)$, $\bar{\Pi}_\ell(t, r)$ and $\bar{\beta}_\ell(t, r)$ as given in Sec. 5.3 converged properly. Throughout, ℓ indicates that the defining asymptotic persistence pair distribution is computed from ℓ-th persistence diagrams. Persistent homology observables without a radius-dependence such as $L_q(t)$ or $n(t)$ often require much less statistics. Due to the lack of statistics, a direct analysis of the asymptotic persistence pair distribution $\bar{\mathcal{P}}_\ell$ is unfeasible. In Appendix A we analyze in more detail the convergence behavior of persistent homology observables with an increasing number of configurations to average, n.

We numerically extract scaling exponents by taking $\bar{\mathcal{B}}_\ell(t, r_b)$ and $\bar{\mathcal{D}}_\ell(t, r_d)$ into account, simultaneously. In Appendix B.2 we describe the corresponding numerical protocol in detail.

Of course, point clouds that are subsets of a regular lattice are generically not in general position, which can result in their Delaunay complex not being a simplicial complex. GUDHI removes corresponding ambiguities by means of a built-in perturbation scheme for points out of general position. Effects of this procedure are not visible.

While simulations take periodic boundary conditions into account, alpha complexes of point clouds are computed non-periodically. This comes about since a crucial function to accomplish this for two-dimensional alpha complexes is still missing in GUDHI. Certainly,

the toroidal topology of the lattice Λ would have an effect on, for example, computed Betti numbers: The 2-torus has $\beta_0(T^2) = 0$, $\beta_1(T^2) = 2$ and $\beta_2(T^2) = 1$, which would at all times and radii add to $\bar{\beta}_\ell(t, r)$. The dynamics of point clouds and their persistent homology groups, however, would remain unaltered, which is why in our dynamical analysis the effects of taking into account the toroidal lattice topology are negligible.

The topology of a square lattice with open boundaries being trivial, no nontrivial two-dimensional homology classes can be present in the constructed alpha complexes, which is why all persistence diagrams at dimension two, $\mathrm{Dgm}_2(X_\nu(t))$, are empty.

Employing that low energies and momenta in the infrared correspond to large distances, if infrared physics is visible in persistent homology observables, it will typically show up at birth and death radii large compared to the lattice spacing. Vice versa, if ultraviolet physics is visible in persistent homology observables, then it will show up at comparably small birth and death radii. To this end, we identify the large-radii regime in birth and death radii distributions with the infrared. The same holds for Betti number distributions. Describing differences between birth and death radii of homology classes, this association is not valid for persistence distributions.

Let $O(t, r)$ be a persistent homology observable expected to rescale according to, for example,

$$O(t, r) = (t/t')^{\eta_1' - \eta_2} O(t', (t/t')^{-\eta_1} r). \tag{6.4}$$

Then, residuals for reference time Qt' are computed as

$$\mathrm{Res.}[O](t', r) := \frac{(t/t')^{\eta_2 - \eta_1'} O(t, (t/t')^{\eta_1} r) - O(t', r)}{O(t', r)}. \tag{6.5}$$

6.2 Two-point correlation function results

In this section, we study the scaling properties of the time-dependent occupation number spectrum $f(t, \mathbf{p})$ as defined in Eq. (2.31).

A scaling ansatz for the occupation number distribution, $f(t, p)$, includes two scaling exponents, α and β as described previously around Eq. (2.1),

$$f(t, |\mathbf{p}|) = (t/t')^\alpha f(t', (t/t')^\beta |\mathbf{p}|). \tag{6.6}$$

In the infrared regime, a thorough numerical analysis as described in Appendix B.1 yields the following scaling exponents,

$$\beta = 0.190 \pm 0.012, \qquad \alpha = 0.400 \pm 0.028, \tag{6.7}$$

choosing reference time $Qt' = 1250$, fitting momenta between $p/Q = 0.07$ and $p/Q = 0.7$ and times between $Qt = 1875$ and $Qt = 37500$. Thus, $\alpha/\beta = 2.11 \pm 0.20$. In Fig. 6.2
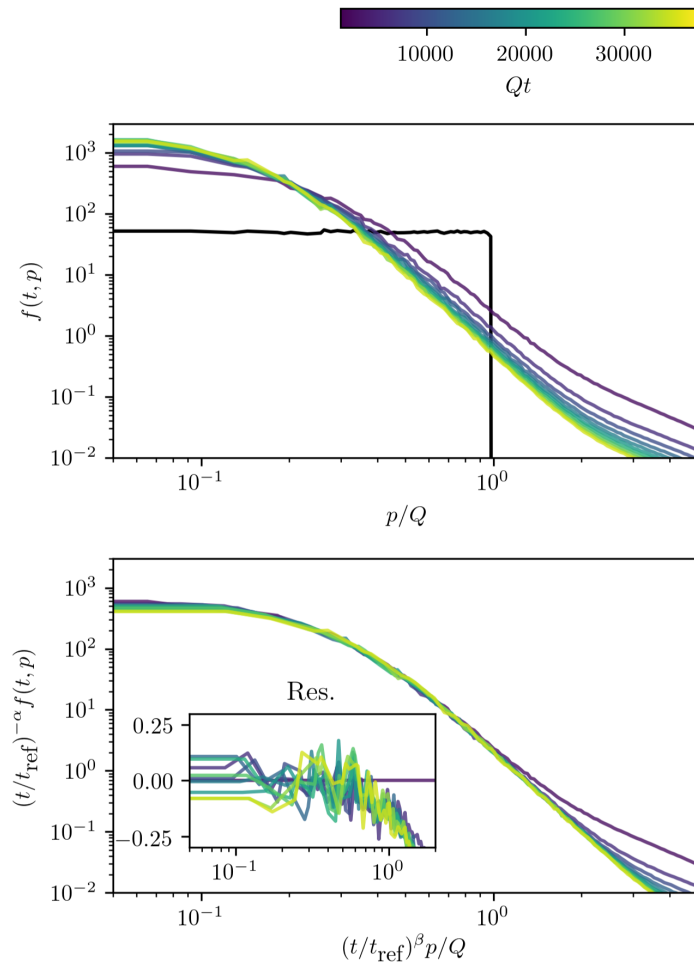
Figure 6.2: Occupation number distributions in the infrared. In black: The initial unrescaled occupation number distribution.

occupation number spectra are displayed in the infrared. By means of the residuals the correctness of the extracted scaling exponents can be easily verified.

The infrared results confirm the findings for box initial conditions in Ref. [47], in which the infrared dynamics of a two-dimensional relativistic scalar field theory has been mapped to that of nonrelativistic complex scalar fields. The extracted scaling exponent β is in very good agreement with the prediction for the anomalous vortex kinetics nonthermal fixed point in a nonrelativistic single-component Bose gas, attributed to the specific dynamics of vortex defects and related vortex interactions in Ref. [46] and discussed in Sec. 2.4.1. Additionally, $\alpha/\beta \approx 2$ indicates the transport of particle numbers to lower momenta [4].

6.3 Birth and death radii distributions

At large length scales, in Fig. 6.3 birth and death radii distributions are displayed for different filtration parameters and times between $Qt = 3750$ and $Qt = 35625$. Zero-dimensional persistent homology classes are always born at radius $Qr_b = 0$, turning the distribution of birth radii of zero-dimensional homology classes trivial. Residuals are computed as described in Eq. (6.5).

The occurring oscillations in distributions are due to statistical uncertainties, being computed from only a finite number of classical-statistical samples. Note that for smaller $\bar{\nu}$-values point clouds comprise fewer points compared to point clouds at larger $\bar{\nu}$-values. Correspondingly, outcomes for persistent homology observables at low $\bar{\nu}$-values behave by construction statistically worse compared to those at higher $\bar{\nu}$-values. The distributions displayed in Fig. 6.3 reflect this.

We first discuss unrescaled variants of the displayed distributions. It is important to note that in any of the distributions the maximum number of counts in birth and death radii distributions decreases with time. Simultaneously, the steep decline at largest radii in birth and death distributions constantly moves to higher radii. This reflects the well-known coarsening dynamics associated to the inverse cascade in the infrared [4] and visible in correlation function results for our simulations, cf. Sec. 6.2.

At the small $\bar{\nu}$-value of 0.2, one may notice that a clear peak in distributions for both dimension $\ell = 0$ and dimension $\ell = 1$ exists. Point clouds at small $\bar{\nu}$-values being vortex nuclei-dominated, we expect this distinguished length scale to provide a measure for the average inter-vortex distance. The peak is less dominant at higher $\bar{\nu}$. We assume that this is due to blurring of the inter-vortex distance by means of bulk points entering point clouds.

The overall form of the unrescaled distributions remains constant in the course of time up to statistical errors, hinting at universal self-similar behavior. The only exceptions are $\bar{\mathcal{D}}_0(t)$ for $\bar{\nu} = 0.6$ and $\bar{\nu} = 0.7$, displayed in Fig. 6.3, panels (a3) and (a4), for which the
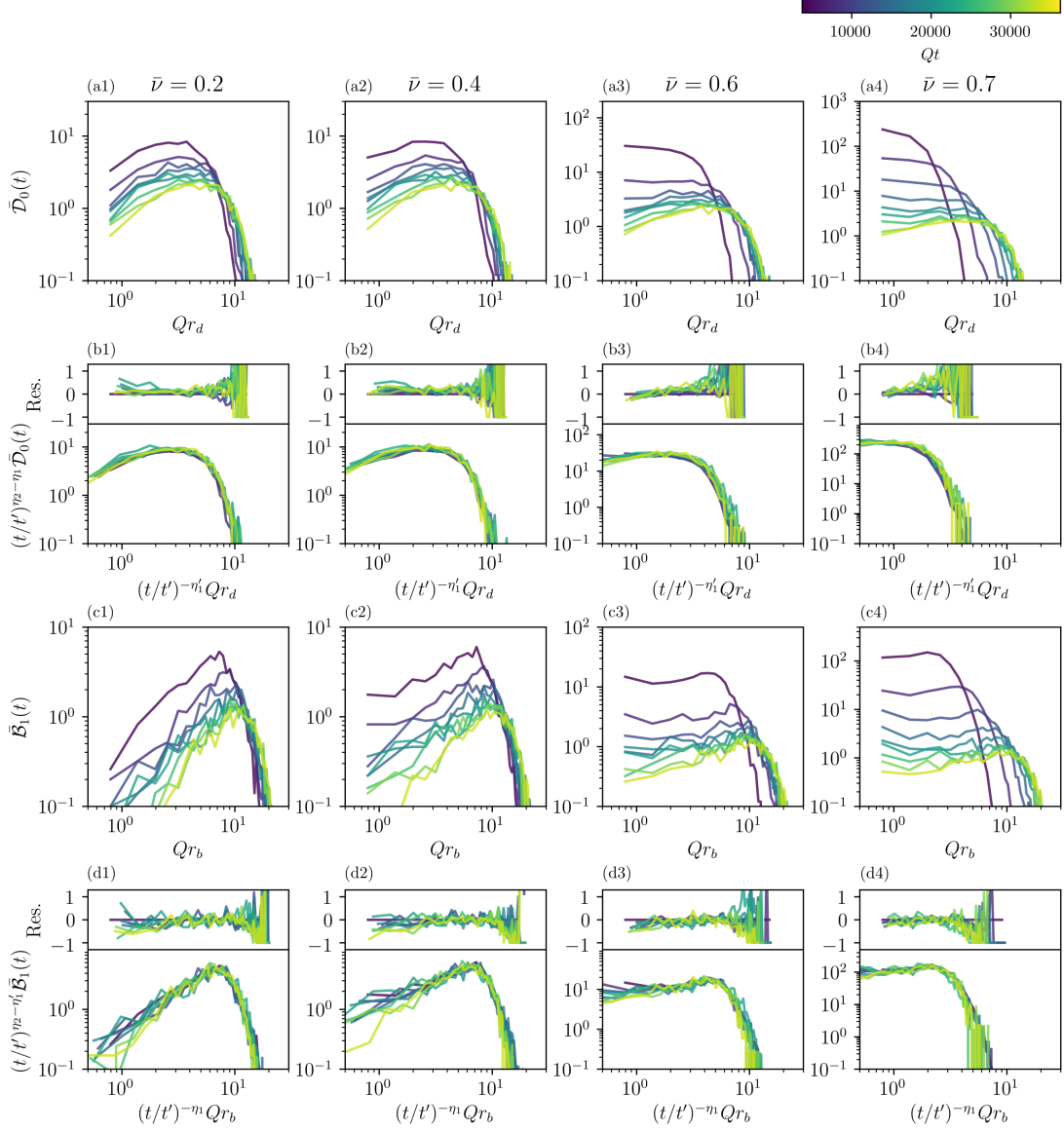
Figure 6.3: Birth and death radii distributions in the infrared. First and second row: death radii of zero-dimensional homology classes, $\bar{\mathcal{D}}_0(t)$. Third and fourth row: birth radii of one-dimensional homology classes, $\bar{\mathcal{B}}_1(t)$. Each column shows data for the indicated filtration parameter, $\bar{\nu}$. The employed time-dependent scaling exponents are displayed in Fig. 6.5.
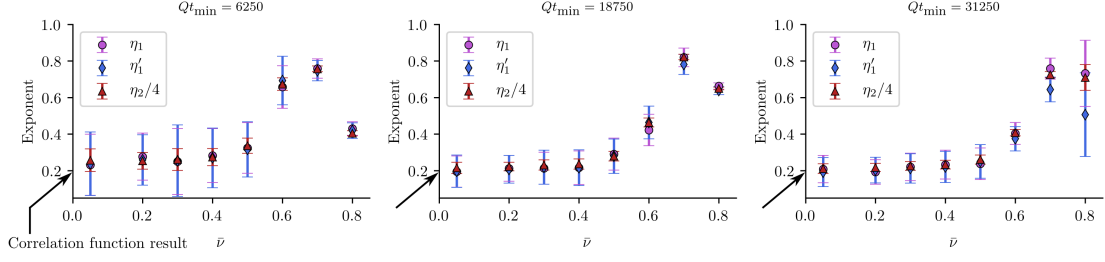
Figure 6.4: Persistent homology scaling exponents at the indicated minimum fitting times, $Qt_{\min}$, the arrow indicating the 2-point correlation function result for the scaling exponent β, as given in Eq. (6.7).
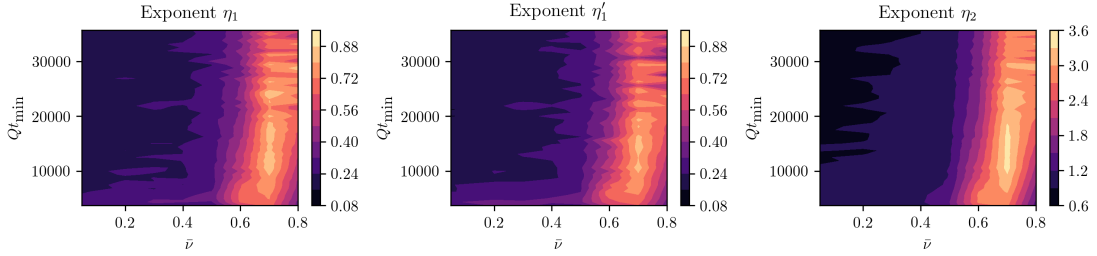
Figure 6.5: Persistent homology scaling exponents for different filtration parameters, $\bar{\nu}$, and minimum fitting times, $Qt_{\min}$.

form of the distribution changes in the course of time. Besides this, all effects discussed are the same across dimensions and types of distributions, indicating the universality of self-similar scaling behavior at infrared nonthermal fixed points across persistent homology observables constructed from the asymptotic persistence pair distribution. A posteriori, this validates that in the self-similar scaling approach to the asymptotic persistence pair distribution, Eq. (5.14), no dimension-dependence has been denoted.

Indeed, distributions can be consistently rescaled with the exponents given in Fig. 6.5. Shifts of the scaling exponents due to the redistribution of amplitudes are accounted for by means of time-varying scaling exponents. We elaborate in more detail on this effect in Sec. 6.5. We observe that for nearly all displayed filtration parameters, $\bar{\nu}$, distributions can be consistently rescaled. Residuals scatter evenly around zero, at least for a significant range of radii. Only $\bar{\mathcal{D}}_0(t)$ for $\bar{\nu} = 0.6$ and $\bar{\nu} = 0.7$, displayed in Fig. 6.3, panels (a3) and (a4), shows comparably large deviations from self-similar dynamics, since the overall shape of the corresponding distributions changes slightly with time.

6.4   A family of scaling exponents

Using the numerical protocol described in Appendix B.2, time-dependent scaling expo-
nents are extracted from the dimension $\ell = 1$ birth and death distributions. Given a time
$Qt_{\min}$, birth and death radii distributions at times $Qt_{\min}$, $Qt_{\min} + 625$ and $Qt_{\min} + 1250$
are fitted simultaneously against distributions at reference time $Qt' = 3750$. In Fig. 6.4
we show the scaling exponents for individual minimum fitting times, $Qt_{\min}$, highlighting
the size of error bars. Errors origin from a finite number of classical-statistical samples
taken into account and from fitting uncertainties.

Results are summarized in Fig. 6.5, in which exponents are displayed in the $(\bar{\nu}, Qt_{\min})$-
plane. The gradual shift of the peak in scaling exponents to higher $\bar{\nu}$-values with an
increasing time, $Qt_{\min}$, is a result of the redistribution of amplitude values with time,
discussed in Sec. 6.5. The scattering of exponent values at larger $\bar{\nu}$-values is due to
statistical uncertainties.

Within error bars η_1 equals η_1' at all $\bar{\nu}$-values investigated here. This provides numer-
ical evidence for that birth and death radii show the same coarsening dynamics in the
infrared. In addition, for all $\bar{\nu}$-values analyzed $\eta_2/\eta_1 = 4$ within the indicated error bars,
as predicted by Eq. (5.24).

By means of the aforementioned observations we restrict the following discussion to
η_1. For $\bar{\nu} \lesssim 0.4$, the exponent η_1 meets the value of $1/5$ associated to the anomalous
vortex kinetics nonthermal fixed point [46] and confirmed by the self-similar dynamics
of the occupation number spectrum in the given simulations, cf. Sec. 6.2. Point clouds,
alpha complexes and persistence pair distributions reflect the occurring vortex dynamics
for small $\bar{\nu}$, correspondingly.

The exponent $\eta_1(\nu)$ increases with $\bar{\nu}$ up to maximum values of between 0.7 and 0.9
depending on $Qt_{\min}$, cf. Fig. 6.5 — a value which is significantly different from $1/5$. We
take a small detour to provide a physical interpretation for this phenomenon.

Collectively, the vortices show anomalous kinetics and dominate point clouds at low
$\bar{\nu}$-values: $\eta_1(\bar{\nu} = 0.05) \approx 0.2$. It is well-known, however, that the two-dimensional
nonrelativistic Bose gas not only exhibits the anomalous vortex kinetics nonthermal fixed
point with $\beta = 0.2$, but also incorporates the strong wave turbulence nonthermal fixed
point characterized by $\beta = 0.5$ [4,8,46]. If the vortices were absent or coupled stronger to
sound excitations in the bulk, only self-similar scaling with $\beta = 0.5$ would be visible, as
argued for in Ref. [46]. Motivated by this, we infer that in the configurations investigated
it is sound excitations in the bulk that reflect the strong wave turbulence nonthermal
fixed point. Correspondingly, if bulk points enter point clouds, then persistent homology
observables might show scaling behavior deviating from $\eta_1 = 0.2$. As can be seen in Figs.
6.1, 6.4 and 6.5 this is the case for growing $\bar{\nu}$-values and explains the increase of η_1. We
refer to the underlying phenomenon as *scaling species mixing* appearing in corresponding
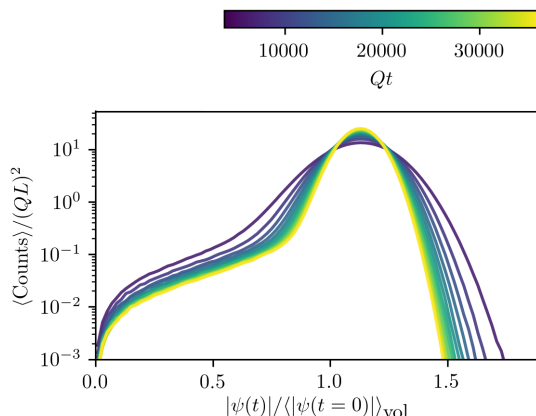
Figure 6.6: Distribution of amplitude-values at different times, averages taken across classical-statistical sampling runs.

point clouds.

Yet, the maximum value of $\eta_1(\nu)$ exceeds 0.5 significantly for all $Qt_{\min}$. A heuristic geometric argument proceeds as follows. Restrict to the dynamics of a single classical-statistical field configuration and label point clouds by $X_\nu(t)$. Let $Y_\nu(t) \subseteq X_\nu(t)$ be loosely associated to anomalous vortex kinetics and $Z_\nu(t) \subseteq X_\nu(t)$ associated to strong wave turbulence in the bulk, such that $X_\nu(t) = Y_\nu(t) \cup Z_\nu(t)$. The alpha complexes of $X_\nu(t)$, $\alpha_r(X_\nu(t))$, however, do not simply decay into $\alpha_r(Y_\nu(t))$ and $\alpha_r(Z_\nu(t))$. Instead, depending on the precise arrangements of points in $Y_\nu(t)$ and $Z_\nu(t)$, there may be a lot of simplices contained in $\alpha_r(X_\nu(t))$ which incorporate points of both $Y_\nu(t)$ and $Z_\nu(t)$. In addition, simplices that only consist of points in $Y_\nu(t)$ or $Z_\nu(t)$ can be very different from the ones in $\alpha_r(Y_\nu(t))$ and $\alpha_r(Z_\nu(t))$. Thus, the construction of alpha complexes from $Y_\nu(t)$ and $Z_\nu(t)$ is a highly nonlinear process. Persistent homology observables reflect this.

6.5 Amplitude redistribution-induced exponent shifts

The scaling exponents displayed in Figs. 6.4 and 6.5 change with time for $\bar{\nu} \gtrsim 0.6$. To discuss the origins of this effect, in Fig. 6.6 amplitude distributions are displayed for different times between $Qt = 3750$ and $Qt = 37500$. As is clearly visible, amplitudes redistribute with growing times towards the peak at around $|\psi(t)|/\langle|\psi(t=0)|\rangle_{\text{vol}} \approx 1.05$. As indicated in Fig. 6.7, point clouds $X_\nu(t)$ with $\bar{\nu} \lesssim 1.0$ become sparser with time.

As deduced earlier, at low $\bar{\nu}$-values point clouds are dominated by accumulations of points around vortex nuclei, while for $\bar{\nu} \gtrsim 0.4$ points in the bulk enter point clouds. With point clouds getting sparser in the course of time it is first bulk points to disappear from point clouds. Accumulations of points around vortex nuclei remain, as can be seen from
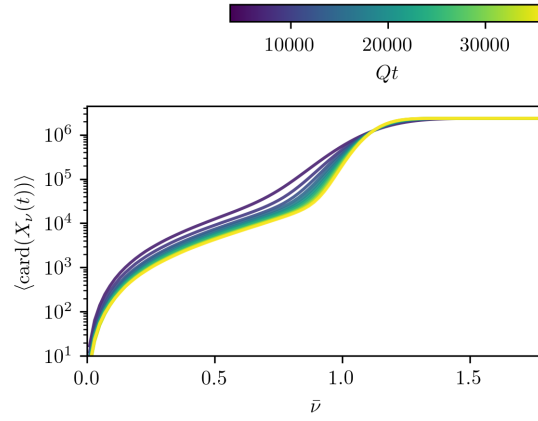
Figure 6.7: The average cardinality of point clouds varying with $\bar{\nu}$ at different times, averages taken across classical-statistical sampling runs.
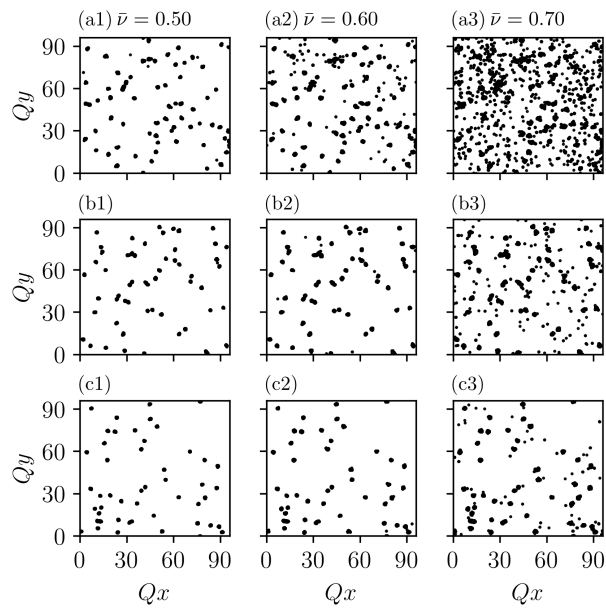

Figure 6.8: Example point clouds $X_\nu(t)$ for different $\bar{\nu}$-values as indicated. Row (a): time $Qt = 3750$. Row (b): $Qt = 7500$. Row (c): $Qt = 11250$.
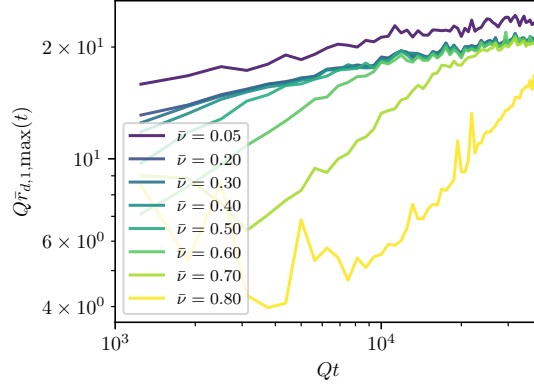
Figure 6.9: The average maximum death radius of 1-dimensional persistent homology classes varying with time, displayed for $\bar{\nu}$-values as indicated.

Fig. 6.8, in which point clouds are displayed for different filtration parameters and times. Given the example point cloud for $\bar{\nu} = 0.5$ at time $Qt = 3750$, we observe that it is made up from accumulations of points (around vertices) mixed with random points in between, while at time $Qt = 11250$ the point cloud consists of nothing but the accumulations. The behavior of point clouds at $\bar{\nu} = 0.6$ is similar, although the point cloud at $Qt = 11250$ still contains random points associated to sound excitations between accumulations. Point clouds at $\bar{\nu} = 0.70$ only get sparser but still contain many bulk points.

The average maximum death radius of 1-dimensional persistent homology classes, $\bar{r}_{d,1,\max}(t)$, is displayed for different $\bar{\nu}$-values in Fig. 6.9. Comparably large fluctuations and outliners occur, since $\bar{r}_{d,1,\max}(t)$ is very sensitive to particular geometric arrangements of points in point clouds of individual classical-statistical samples. According to Eq. (5.19), if the system's asymptotic persistence pair distribution scales self-similarly in time and $\eta_1 = \eta_1'$, then $\bar{r}_{d,1,\max}(t) \sim t^{\eta_1}$. Indeed, $\bar{r}_{d,1,\max}(t)$ shows power-law behavior within individual periods of time and confirms the shifts in scaling exponents as indicated by the results displayed in Fig. 6.5, which have been deduced from birth and death radii distributions. For instance, for $\bar{\nu} = 0.6$ a shift occurs between times $Qt \approx 9000$ and $Qt \approx 13000$.

Recently, the phenomenon of prescaling has been discovered, that is, the rapid establishment of a universal scaling form of distributions long before the universal values of corresponding scaling exponents are realized [83, 84]. Although we also study time-dependent scaling exponents of constant-form distributions, we want to stress that in our case this is not a manifestation of prescaling. Instead, it is an artifact of the sharp cutoff at the filtration parameter to generate point clouds, rendering point clouds themselves and their persistent homology sensitive to amplitude redistribution effects.
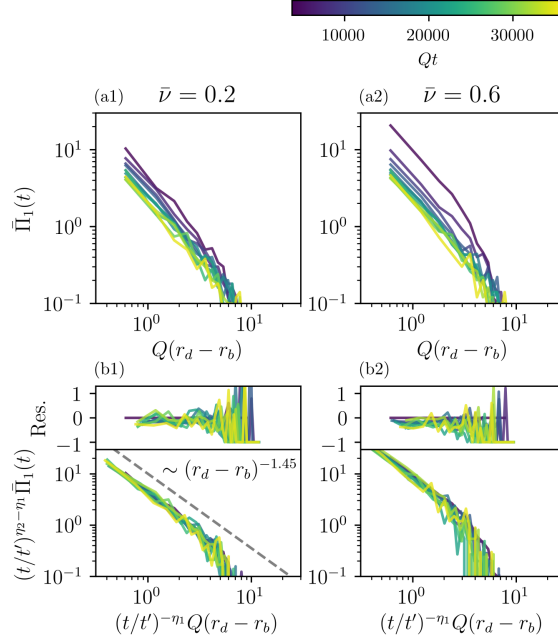
Figure 6.10: Persistence distributions in the infrared. Each column shows data for the indicated filtration parameter, $\bar{\nu}$. The employed time-dependent scaling exponents are displayed in Fig. 6.5.

6.6   Power-law in persistence

In Fig. 6.10 persistence distributions for different filtration parameters, $\bar{\nu}$, are displayed. Again, fluctuations are due to statistical uncertainties. Distributions can be consistently rescaled using time-dependent scaling exponents as in Fig. 6.5. To this end, we attribute the observed physics to the inverse cascade. We want to emphasize that the persistence distributions for a low filtration parameter such as $\bar{\nu} = 0.2$ distinctly show power-law behavior with persistence at all times, the corresponding persistence regime shrinking with increasing filtration parameters. A power-law fit of the rescaled distributions reveals a scaling with persistence as $\sim (r_d - r_b)^{-\zeta}$ with

$$\zeta = 1.450 \pm 0.027. \qquad (6.8)$$

The power-law fit is first carried out for persistence values between $Q(r_d - r_b)_{\min} = 0.3125$ and $Q(r_d - r_b)_{\max} = 5.0$ at each of the times $Qt_i = 3750, 4375, \ldots, 37500$, individually, to obtain values for $\zeta(t_i)$ and its fitting error at time t_i, $\Delta\zeta(t_i)$, $i = 1, \ldots, N_i$. Subsequently, the value of ζ is defined to be the average of the obtained exponents. Its error squared, $\Delta\zeta^2$, is computed by means of standard error propagation as the sum of the temporal error squared and the sum of all $\Delta\zeta(t_i)^2/N_i^2$.

6.7 Betti numbers

In Sec. 5.4 we derived that if the asymptotic persistence pair distribution scales self-similarly, then Betti number distributions do so as well in the way described by Eq. (5.20). Having extracted scaling exponents from birth and death radii distributions in Sec. 6.4, we investigate Betti number distributions as a consistency check.

In Fig. 6.11 Betti number distributions for both zero- and one-dimensional homology classes are displayed. For all $\bar{\nu}$ and t, $\bar{\beta}_0(t, r)$ is a monotonically decreasing function, since zero-dimensional persistent homology classes are always born at zero radius and $\bar{\beta}_0(t, r)$ captures their death, that is, separated connection components in the alpha complexes merging. We find a peak in unrescaled $\bar{\beta}_1(t, r)$, which, again, decreases in magnitude and shifts to higher radii as an indication of coarsening dynamics associated to the inverse cascade.

Approximately, Betti numbers display self-similar scaling behavior. However, residuals of the rescaled $\bar{\beta}_0(t)$ increase at large radii and $\bar{\beta}_1(t)$ shows comparably large fluctuations. Nonetheless, rescaled Betti number distributions confirm previously extracted exponents.
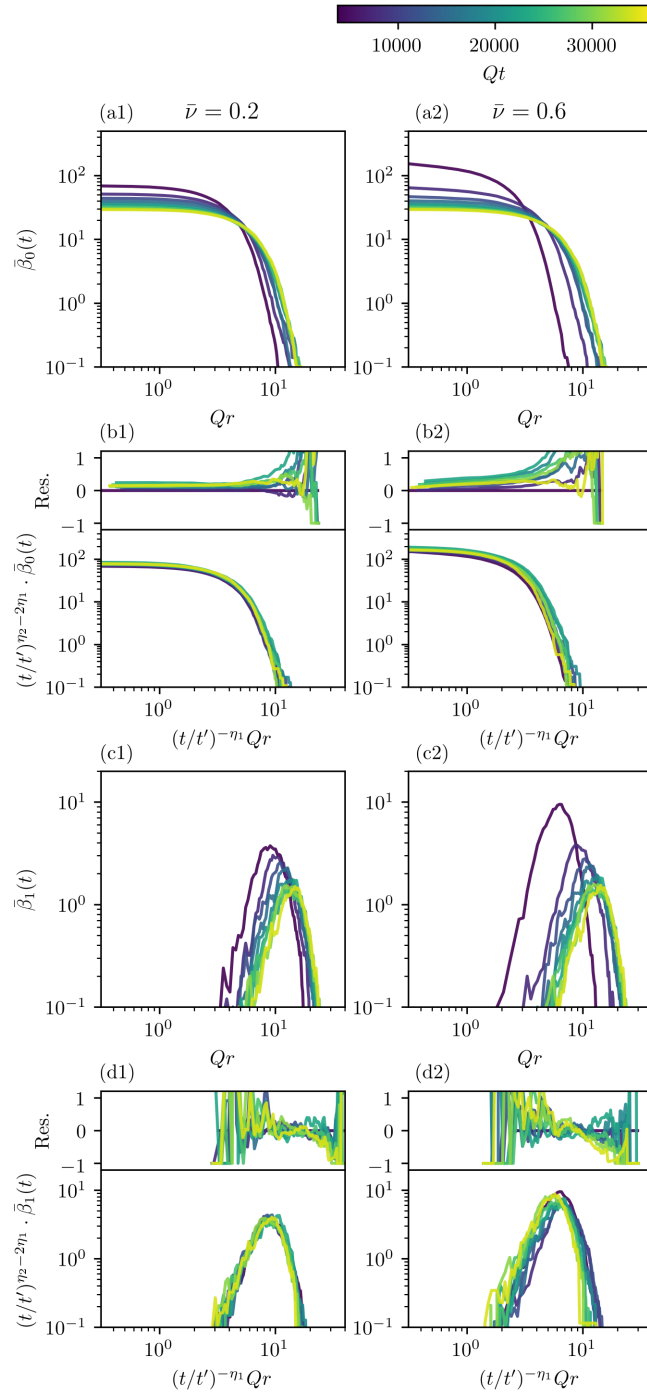
Figure 6.11: Betti number distributions are shown for dimensions ℓ and filtration parameters $\bar{\nu}$ as indicated. Scaling exponents are set to the time-dependent values indicated in the caption of Fig. 6.3, setting $\eta_1' := \eta_1$.

Chapter 7

Further explorations

In this chapter we report about further explorations undertaken in the course of this work. In particular, in Sec. 7.1 we discuss and present results for a more general approach to the construction of point clouds via interlevel sets. In Sec. 7.2 we derive a computation framework for relative homology groups and provide corresponding results, studying Betti numbers *modulo* vortex nuclei subcomplexes. A discussion of the essential analysis of experimental spinor Bose gas data [13], the first tries of which have been carried out in the scope of this Master project, will be provided elsewhere in the near future.

The motivation for these investigations is primarily to separate anomalous vortex dynamics and its self-similar scaling behavior from the strong wave turbulence nonthermal fixed point dynamics in a cleaner fashion compared to the indications found in Sec. 6.4 in factor of scaling species mixing.

7.1 Point clouds via interlevel sets

In this section we discuss the construction of point clouds as interlevel sets of the classical field amplitudes. By means of an additional lower threshold for amplitudes the basic idea is to cut out vortex nuclei and their surroundings, which by value typically have very small amplitudes, from point clouds. The latter than comprise mainly points associated to bulk fluctuations. However, it is certainly possible that the holes within point clouds around vortex nuclei, that arise from a sharp lower cutoff in amplitudes, have a tremendous effect on the dynamics visible in persistent homology observables.

7.1.1 The approach

As mentioned, we construct point clouds as interlevel sets of the amplitude. To this end, let $\nu_1, \nu_2 \in [0, \infty)$ with $\nu_1 \leq \nu_2$. Point clouds are defined as

$$X_{\nu_1,\nu_2}(t) := |\psi(t,\cdot)|^{-1}[\nu_1, \nu_2] = \{\mathbf{x} \in \Lambda \,|\, \nu_1 \leq |\psi(t,\mathbf{x})| \leq \nu_2\}, \qquad (7.1)$$

$\psi : \mathbb{R} \times \Lambda \to \mathbb{C}$ being a single field configuration as it appears in classical-statistical simulations of the nonrelativistic Bose gas. Given fixed ν_1, ν_2-values, we compute the sequence of alpha complexes and study persistent homology observables hereof. Setting $\nu_1 = 0$, we recover the approach taken in Chap. 6. Comparing outcomes for different ν_1, ν_2, we may gain additional insights into the specific dynamics of the Bose gas.

Again, we provide values of ν_1, ν_2 in terms of the dimensionless quantities $\bar{\nu}_i$, defined as in Eq. (6.2). Throughout this section, simulation parameters are those denoted in Sec. 6.1.1.

7.1.2   Numerical results

In Fig. 7.1 we display birth and death radii distributions for various interlevel set parameters, $\bar{\nu}_1$ and $\bar{\nu}_2$. Based on the discussion in Sec. 6.3, using lower bounds of $\bar{\nu}_1 = 0.2, 0.4, 0.5, 0.6$, vortex nuclei and their surrounding have been cut out from the corresponding point clouds, leaving behind associated holes in the point clouds. At the indicated values of $\bar{\nu}_2 = 0.6, 0.7$ point clouds comprise mainly points associated to bulk fluctuations. To this end, the interlevel set filtration parameters chosen in Fig. 7.1 seems ideal to investigate, whether cutting out vortex nuclei by means of a lower threshold on amplitudes alters the self-similar scaling behavior, potentially such that solely known strong wave turbulence results are visible.

Clearly, the data displayed in Fig. 7.1 reveals that persistent homology observables of interlevel sets also show self-similar scaling, being successfully rescalable using persistent homology scaling exponents as displayed in Fig. 7.2. All aspects of the shown distributions have been discussed beforehand in Sec. 6.3, which is why we do not provide redundant information here. We note that altering the lower filtration parameter, $\bar{\nu}_1$, does not have a notable impact on corresponding point clouds. In addition, scaling exponents are by values the same as extracted previously for sublevel sets of amplitudes, cf. Fig. 6.5.

Thus, by means of interlevel sets, cutting out vortex nuclei, we see that the remaining holes in point clouds around the latter also have an effect on the resulting persistent homology observables. They are by value still larger than to be expected, if only strong wave turbulence was present and driving the dynamics of point clouds. Following the discussion of Sec. 6.4 and Ref. [4], we would at least for $\bar{\nu}_1 = 0.6, \bar{\nu}_2 = 0.7$ expect that $\eta_1(\bar{\nu}_1, \bar{\nu}_2) \approx 1/2$. In addition, vortices are nonlocal excitations with their energy content spread through the whole physical system, cf. Sec. 2.2.3. Hence, even aside from holes in point clouds around their nuclei they might have a dynamical impact on the system. This can also be a reason for that via interlevel sets we cannot clearly discriminate between the strong wave turbulence scaling species and the anomalous vortex kinetics scaling species.

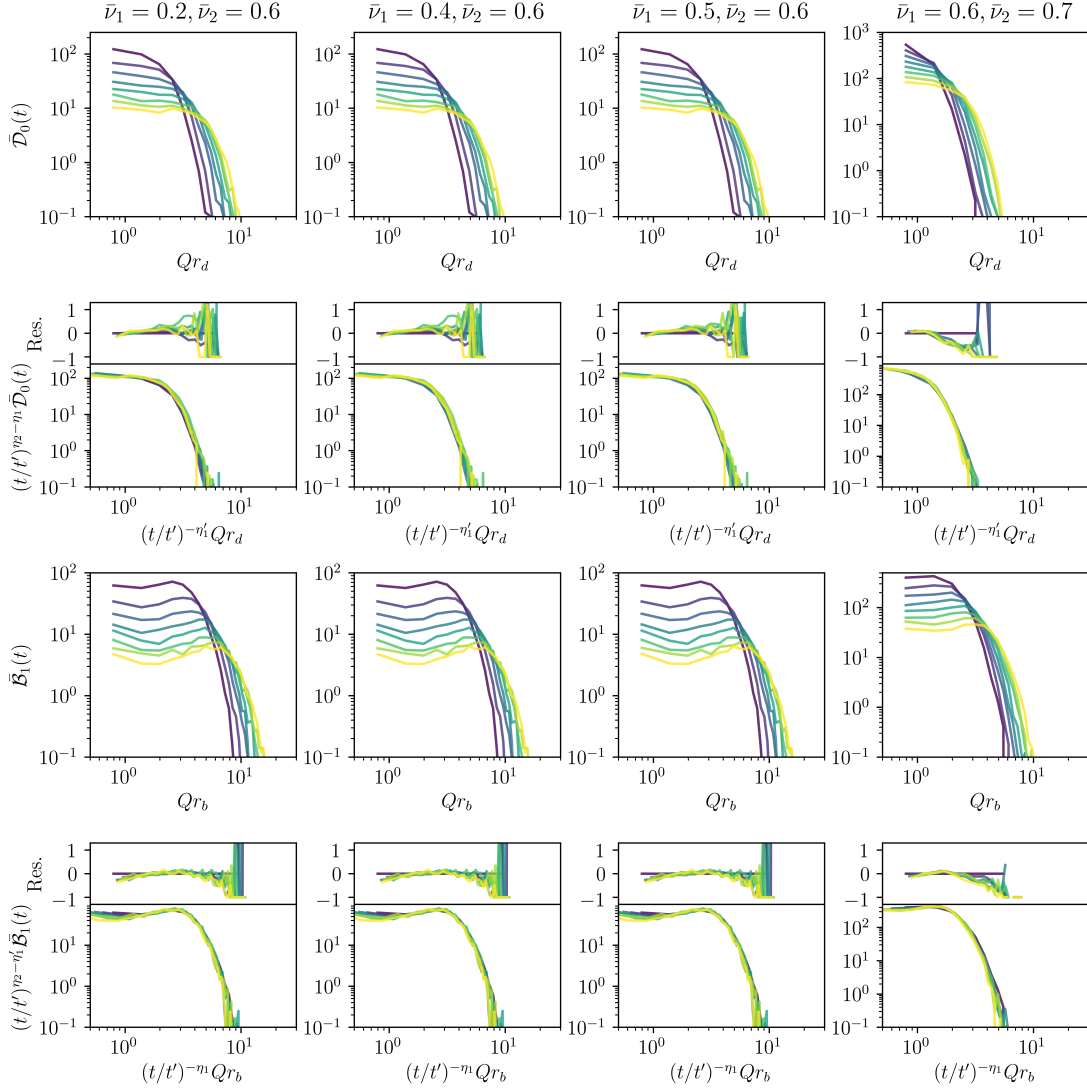The increase in exponent values visible in Fig. 7.1 in particular for $\bar{\nu}_1 = 0.6, \bar{\nu}_2 = 0.7$

Figure 7.1: Birth and death radii distributions from amplitude interlevel sets in the infrared. First and second row: death radii of zero-dimensional homology classes, $\bar{\mathcal{D}}_0(t)$. Third and fourth row: birth radii of one-dimensional homology classes, $\bar{\mathcal{B}}_1(t)$. Each column shows data for the indicated filtration parameters, $\bar{\nu}_1$ and $\bar{\nu}_2$. The employed time-dependent scaling exponents are displayed in Fig. 7.2. Purple to yellow: Results at equidistant simulation times between $Qt = 1875$ and $Qt = 6250$.
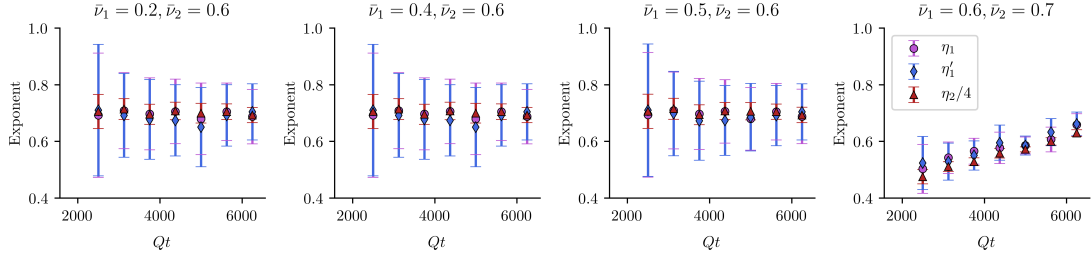
Figure 7.2: Persistent homology scaling exponents from amplitude interlevel sets for different filtration parameters, $\bar{\nu}_1$ and $\bar{\nu}_2$, and fitting times, Qt.

is due to amplitude redistribution-induced exponent shifts as observable in Fig. 7.2 and discussed in Sec. 6.5. Note that this effect plays a minor role for the interlevel sets investigated here compared to the shifts visible in Fig. 7.2, since we investigate a smaller range of times here, rendering the effect tinier.

7.2   Relative homology groups

Inspired by Ref. [33], this section is devoted to numerically exploring relative homology groups and their Betti numbers in order to unravel and understand the spectrum of scaling exponents observed and discussed in Sec. 6.4. The construction is motivated similarly to the one of interlevel sets in the previous section. Solely, here we do not cut out vortex nuclei and their surroundings, but try to understand homology groups *modulo* the nuclei and their surroundings. By this means, we hope to eliminate the dynamical dependence on the holes in the arising point clouds.

To cut a long story short, to date numerical investigations need to be considered too preliminary to draw reliable conclusions. The required careful and detailed analysis lies outside the scope of this master project and is postponed to the near future.

7.2.1   Computing relative homology Betti numbers

As constructed in Sec. 3.2.2, relative homology groups are defined for a nested pair of simplicial complexes. In the following we define such a nested pair, tailored to discriminate between the dynamics of vortices and that of bulk points. The setting is the two-dimensional nonrelativistic Bose gas simulations introduced and investigated in Chap. 6, though the construction is carried out here for an arbitrary spatial dimension, d.

Let $\nu_{\mathrm{vor}} > 0$ be small, such that $V := X_{\nu_{\mathrm{vor}}}(t) \subset \mathbb{R}^d$ mainly comprises vortex nuclei and points in their surroundings. Let $\nu > \nu_{\mathrm{vor}}$ be another filtration parameter, such that point clouds $X_\nu(t)$ also comprise bulk points to a significant extent. Let $\epsilon > 0$ and $r \geq 0$.

We define the *vortex subcomplex* $v_{\epsilon,r}(X, V)$ of the alpha complex of $X := X_\nu(t)$ to the radius r, $\alpha_r(X_\nu(t))$, via

$$v_{\epsilon,r}(X, V) := \left\{ [x_1, \ldots, x_{\ell+1}] = \sigma \in \alpha_r(X) \,\middle|\, \forall i : x_i \in \bigcup_{w \in V} B_\epsilon(w) \cap X, \, \ell \in \{0, \ldots, d\} \right\},$$
(7.2)

$B_\epsilon(w)$ denoting the d-ball of radius ϵ around the point w. Indeed, we easily see that $v_{\epsilon,r}(X, V)$ is a simplicial subcomplex of $\alpha_r(X)$. Physically speaking, if the points in X lie sufficiently dense in the vicinities of vortex nuclei and inbetween, then $v_{\epsilon,r}(X, V)$ will be a good approximation of the vortex nuclei and their surroundings.

For fixed $\nu_{\mathrm{vor}}, \epsilon, t$ and again setting $X := X_\nu(t)$, we define an altered version of the Delaunay radius function Rad as defined in Sec. 3.1.2, namely $\widetilde{\mathrm{Rad}} : \mathrm{Del}(X) \to \mathbb{R}$ set to

$$\widetilde{\mathrm{Rad}}(\sigma) := \begin{cases} -1 & \text{if } \sigma \in v_{\epsilon,r}(X, V), \\ \mathrm{Rad}(\sigma) & \text{if } \sigma \notin v_{\epsilon,r}(X, V). \end{cases}$$
(7.3)

Using the map $\widetilde{\mathrm{Rad}}$, we define altered alpha complexes as sublevel sets of it,

$$\widetilde{\alpha}_r(X) := \widetilde{\mathrm{Rad}}^{-1}[-1, r],$$
(7.4)

r taking now values in $[-1, \infty)$. Again, we find that they form a nested sequence of simplicial complexes, implying the existence of an inclusion map $\iota^{r,s} : \widetilde{\alpha}_r(X) \hookrightarrow \widetilde{\alpha}_s(X)$ for all $s \geq r$. Thus, one can study persistent homology groups of the arising persistence module, $\mathcal{M} := ((H_*(\widetilde{\alpha}_r(X)))_r, (\iota_*^{r,s})_{r \leq s})$. The persistence diagram of $\mathcal{M}$ we denote by $\widetilde{\mathrm{Dgm}}_\ell^{(\alpha)}(X)$.

In fact, one can easily compute Betti numbers, $\widetilde{\beta}_\ell(t, r)$, of the relative homology groups of the nested pair of simplicial complexes, $(\alpha_r(X), v_{\epsilon,r}(X, V))$, from $\mathcal{M}$ and the persistence diagrams $\widetilde{\mathrm{Dgm}}_\ell^{(\alpha)}(X)$,

$$\widetilde{\beta}_0(t, r) := \mathrm{card}\left\{ (b, d) \in \widetilde{\mathrm{Dgm}}_0^{(\alpha)}(X) \,\middle|\, 0 \leq b \leq r < d \right\},$$
(7.5a)

$$\widetilde{\beta}_\ell(t, r) := \mathrm{card}\left\{ (b, d) \in \widetilde{\mathrm{Dgm}}_{\ell-1}^{(\alpha)}(X) \,\middle|\, -1 = b < d \leq r \right\}$$
$$+ \mathrm{card}\left\{ (b, d) \in \widetilde{\mathrm{Dgm}}_\ell^{(\alpha)}(X) \,\middle|\, 0 \leq b \leq r < d \right\},$$
(7.5b)

for any $\ell \geq 1$. To understand these relations, one may first notice that in zero-dimensional homology relative to the vortex subcomplex a persistent homology class for which a representing cycle fully resides in the vortex subcomplex is excluded from the counting of connection components, explaining Eq. (7.5a). The interpretation of Eq. (7.5b) proceeds

similarly. Restrict to $\ell = 1$. Loops in the altered alpha complexes can arise in two ways. First, as in standard alpha complexes, explaining the second term in Eq. (7.5b). Second, via a cycle that is contained in $v_{\epsilon,r}(X, V)$ but dies at a radius larger than or equal to zero, yielding the first contribution to $\widetilde{\beta}_1(t, r)$ in Eq. (7.5b). This explanation similarly applies in higher dimensions, $\ell > 1$. The relative contribution to $\widetilde{\beta}_\ell(t, r)$ corresponds to homology classes that get born in the vortex subcomplex but whose interiors get filled with simplices for which at least one of them lies outside the vortex subcomplex. If in this case there was no simplex in the interior of a representing cycle of a relative homology class that lies outside of the vortex subcomplex, in relative homology the cycle would shrink to a point.

We want to stress that upon this procedure the bare persistence diagrams $\widetilde{\mathrm{Dgm}}_\ell^{(\alpha)}(X)$ cannot be interpreted as representing relative persistent homology classes, directly. By means of Eqs. (7.5a) and (7.5b), it is only relative Betti numbers that can be reproduced correctly.

Note that on the numerically implemented $d = 2$ lattice, which in the employed topological analysis routine is assumed to be a square lattice with open boundaries, that is, having zero homology groups across all dimensions, $\widetilde{\beta}_2(t, r)$ is only made up from contributions of the first term in Eq. (7.5b). This way, it is a monotonically increasing function with r.

In Fig. 7.3 we display the 1-skeleta of vortex subcomplexes for $\bar{\nu}_{\mathrm{vor}} = 0.2$ and $\bar{\nu} = 0.6$, $\bar{\nu} = 0.7$. Note that the more points are present in the bulk between vortices, the more accurate the vortex subcomplexes describe the occurring accumulations of points around nuclei.

7.2.2   Prospective numerics

Equations (7.5a) and (7.5b) provide a numerically amenable way to numerically compute Betti numbers of homology groups relative to a vortex subcomplex. Manually setting Delaunay radii of simplices in a vortex subcomplex to -1, we implemented a computation procedure for the altered alpha complexes, $\widetilde{\alpha}_r(X_\nu(t))$, and their persistent homology groups. Eqs. (7.5a) and (7.5b) have been built in by hand in order to compute relative Betti numbers.

In Fig. 7.4 we display relative Betti number distributions at different times for two filtration parameters $\bar{\nu} = 0.6$ and $\bar{\nu} = 0.7$. The radius to construct vortex subcomplexes is set fixed to $Q\epsilon = 3.75$. First, one may notice that while for $\bar{\nu} = 0.6$ the time-dependence of the displayed relative Betti numbers seems quite irregular, for $\bar{\nu} = 0.7$ it appears much smoother. Clearly, this provides evidence for that at a higher filtration parameter vortex subcomplexes become less random structures and actually capture vortex nuclei better, evoked through the higher number of bulk points in corresponding point clouds.
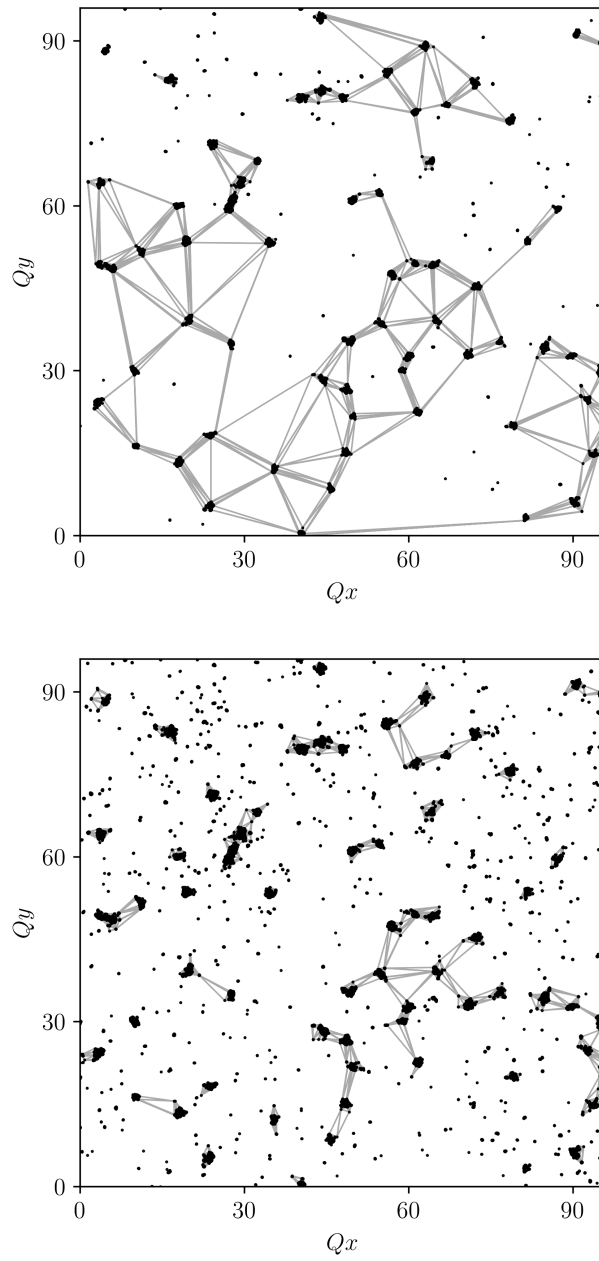
Figure 7.3: 1-skeleta of vortex subcomplexes for $\bar{\nu}_{\mathrm{vor}} = 0.2$, $Q\epsilon = 2.5$, displayed in grey. The black dots correspond to the point clouds $X_\nu(t)$. Left panel: $\bar{\nu} = 0.6$. Right panel: $\bar{\nu} = 0.7$.
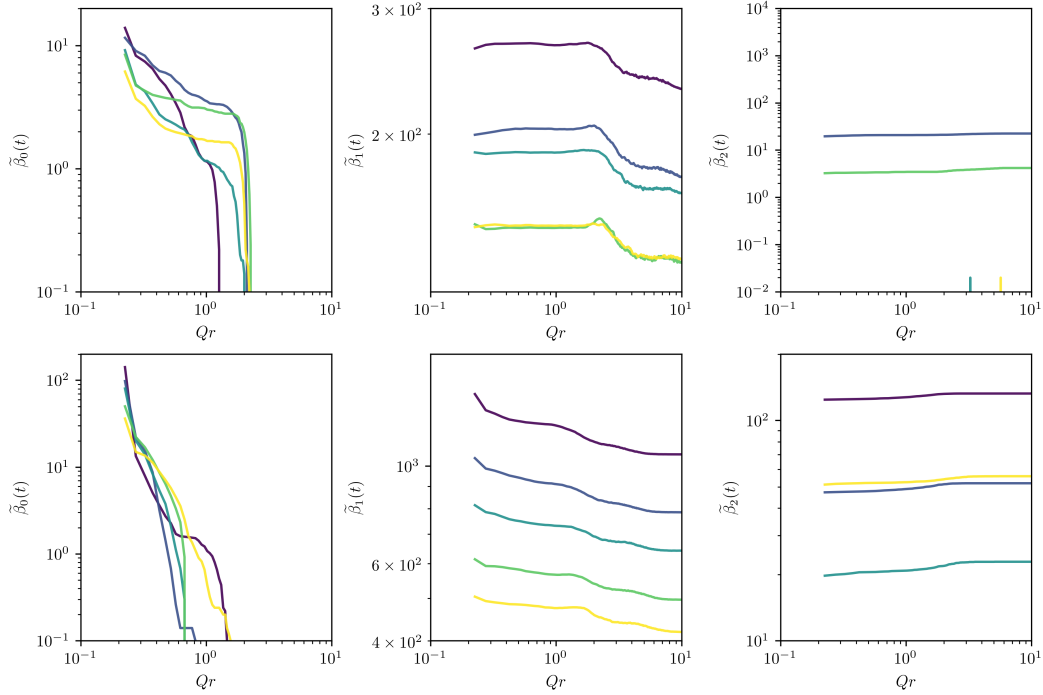
Figure 7.4: Relative Betti number distributions for homology classes of the indicated dimensions $\ell = 0, 1, 2$ and $\bar{\nu}_{\mathrm{vor}} = 0.2$, $Q\epsilon = 3.75$. Top row: $\bar{\nu} = 0.6$. Bottom row: $\bar{\nu} = 0.7$. From purple to yellow: Equidistant times between $Qt = 3750$ and $Qt = 6250$.

The structure of zeroth Betti number distributions appears very irregular. Similarly, the overall shape of $\widetilde{\beta}_1(t, r)$ is hard to interpret. Focussing on $\bar{\nu} = 0.6$, appearing structures in the curves seem to significantly vary in time. This might indicate that the infinite-volume limit is not reached properly, yet, at the investigated system size of $N = 1536$. Increasing the filtration parameter, much more points enter the bulk between the vortices, thus improving vortex subcomplexes in the sense that the become a better proxy for vortex nuclei and their surroundings, cf. Fig. 7.3. For $\bar{\nu} = 0.7$, $\widetilde{\beta}_1(t, r)$ this results in a much regular structure of the displayed curves. Nonetheless, upon comparing these distributions at different times, even they seem not consistently rescalable. Second relative Betti numbers display heavily irregular behavior across investigated times.

This leads us to the conclusion that in order to reliably draw conclusions from the numerical results a much more thorough and detailed investigation is necessary, including, for instance, a careful analysis of the dependence on the system volume. This lies outside the scope of this work and is postponed to the near future.

Chapter 8

Conclusions

Inspired by topological data analysis techniques and their recent advances, in the present work we investigated possible uses of the persistent homology machinery in the quantum field-theoretic surrounding. We proposed a novel class of observables, persistent homology observables, in order to globally detect occurring connectivity and clustering structures, focussing here on the classical-statistical regime. Employing functional summaries [68], a guiding principle in this proposal has been to carry out constructions on the basis of mathematical theorems, which guarantee, for instance, that averages are well-defined within the considered spaces of functional outcomes. Within the classical-statistical approximation we provided a general computation scheme for expectation values of persistent homology observables, inferring the existence of a corresponding quantum field-theoretic operator. Containing different types of information on occurring homological features, we defined various geometric quantities from a fairly general integral kernel appearing, the asymptotic persistence pair distribution, see Eq. (5.5).

As a prototype application, in this work we considered the investigation of universal structures far from equilibrium in the vicinity of nonthermal fixed points and their manifestions in persistent homology observables. Of particular interest was the self-similar dynamical behavior, encoded in a corresponding scaling approach to the asymptotic persistence pair distribution, see Eq. (5.14). Comparing to notions of self-similarity across the literature, where typically a respective scaling ansatz is made for correlation functions in momentum space [4, 13, 85], our ansatz captures the geometric, essential meaning of self-similarity more intuitively, providing a position space means of understanding continuous "fractality". A packing relation between scaling exponents appearing in the ansatz revealed that the scaling behavior visible in the asymptotic persistence pair distribution and derived geometric quantities is inherently linked to the geometry of the system at hand, see Eq. (5.24). We provided both a simple heuristic argument in favor of the relation, as well as a more rigorous deduction of the latter, demonstrating that it can be based on a mathematical footing. Intuitively, the packing relation describes a bound on

the number of homology classes of a given size, which can be wrapped into a constant finite volume.

Serving as a numerical proof-of-principle, we studied persistent homology observables at large length scales in classical-statistical lattice simulations of the two-dimensional nonrelativistic Bose gas. Our approach to the study of persistent homology has been to first construct point clouds as sublevel sets of amplitudes of individual classical-statistical field realizations living on a spatial lattice and to then compute their sequence of alpha complexes and the corresponding persistent homology groups. Confirming the existence of a self-similarly scaling asymptotic persistence pair distribution, we numerically demonstrated that, indeed, self-similarity in the vicinity of a nonthermal fixed point is a concept that is not restricted to n-point correlation functions. To astonishing accuracy, the packing relation could be confirmed. Crucially, for the scaling ansatz to the asymptotic persistence pair distribution to consistently describe the numerical data, filtration parameter- and time-dependent scaling exponents have been necessary. Our work thus showed for the first time the existence of a continuous spectrum of scaling exponents.

The two-dimensional nonrelativistic Bose gas exhibits different types of collective phenomena leading to universal behavior far from equilibrium: strong wave turbulence and anomalous vortex kinetics. Indications for both have been visible in previous studies [4, 46]. In particular, the two have been shown to display different universal scaling exponents. We conjecture that the occurring scaling exponent spectrum is a result of mixing points in point clouds which can be loosely associated to the two different types of dynamical components. Nonetheless, with regard to evidence for this mixing of scaling species our findings have the drawback of merely providing indications for the presence of strong wave turbulence by means of the growth of persistent homology scaling exponents, explicitly showing only the presence of the anomalous vortex kinetics scaling behavior by means of the distinct plateau visible in Fig. 6.5.

Further exploratory investigations carried out in this work, which still need to be considered preliminary, had the explicit goal to provide clear evidence for the simultaneous presence of both strong wave turbulence and anomalous vortex kinetics. The study of interlevel sets of the amplitudes of individual classical-statistical field realizations did not lead to more transparent indications for the presence of strong wave turbulence and the associated scaling behavior. Instead, persistent homology observables for the interlevel sets displayed the very same dynamics as has been observed for sublevel sets. A second, more intricate approach described in this work is to study homology groups relative to vortex nuclei. Having constructed simplicial vortex subcomplexes, via a modified version of the Delaunay radius function simple formulae for relative Betti numbers could be given, making corresponding numerical investigations feasible. However, we revealed that a thorough and detailed investigation of numerical results is required, unfortunately

lying outside the scope of this work. Clearly, this proposal has the potential to clarify the character of nonequilibrium universal behavior in the two-dimensional Bose gas.

With the present work we seeked to provide a first prototype study in favor of the usage of persistent homology observables in QFT. As has become clear in the course of this work, dozens of possible future research trajectories deserve attention. Clearly, further evidence for the phenomenon of scaling species mixing would be desirable. Methodologically, central to this work is the construction of point clouds via amplitude sublevel sets of the complex-valued scalar fields, see Eq. (5.1). In fact, an immense freedom of choice exists to generate point clouds from fields. For the example of the nonrelativistic Bose gas, as a manifestation of the global $U(1)$-symmetry of the system persistent homology results for phase interlevel sets should be invariant under global phase shifts. Is there anything new to learn from using higher-order correlation functions on the level of individual classical-statistical realizations to obtain point clouds? What can be learned from other approaches to generate point clouds?

In recent years, universal aspects of nonequilibrium dynamics in isolated quantum dynamics have been verified experimentally [13–15]. Would it be possible to find indications for self-similar scaling behavior of the asymptotic persistence pair distribution in corresponding experimental data?

Studying correlation functions, extending from equal-time to unequal-time arguments revealed novel characteristics of far-from-equilibrium dynamics [12,16,59]. Our approach is based on the construction of equal-time point clouds, their equal-time alpha complexes and equal-time persistent homology groups. Can we meaningfully extend this to unequal-time alpha complexes, shifting dynamical aspects of persistent homology observables more to the center? To accomplish this, appropriate simplicial complexes are required. Various approaches are conceivable. A possibly physically natural family of simplicial complexes is formed by the weighted alpha complexes [28], replacing the standard metric on Euclidean space as it is used in the construction of alpha complexes by a more general quantity, in which field-values and a Minkowski metric could be encoded. In principle, one does not even need a lattice in order to construct point clouds. Even for fields living on arbitrary smooth and triangulable manifolds, persistent homology groups could be constructed, for instance, using singular homology of sublevel sets [82]. This opens up countless possibilities for further studies.

In non-Abelian gauge theories, extended objects such as Wilson loops are of particular importance. In addition, topological structures in gauge theories such as θ-vacua, various anomalies and knot invariants have been extensively investigated [86,87]. Is it sensible to extend the field of topological structures in gauge theories to include persistent homology — what novelties do the persistence-related aspects hold ready? Is an approach to the construction of point-clouds similar to the one provided in this work even possible in a

gauge-invariant fashion?

In any case central to the approach presented in this work and to the further exploration of persistent homology observables in QFT is the existence of quantum field-theoretic operators corresponding to persistent homology observables. In full generality, is such a construction possible from local operators? Can the relation between gauge and knot theory [88] or derivations of mathematical theorems linking local and global quantities such as the Gauss-Bonnet theorem or the Atiyah-Singer index theorem provide insights into this direction and be exploited?

Certainly, paths to illuminate also include analytic prediction for persistent homology observables in a given QFT. Across the literature, different works may provide useful starting points in this direction. Inter alia, for different types of random fields statistical statements could be made [89, 90], and predictions for alpha complexes of a class of random point clouds have been derived by means of integral geometry techniques [61].

In persistent homology theory the description of multidimensional persistence is currently of key interest and amply studied, though not easy to handle. Useful invariants yielding a full classification of corresponding persistence modules do not exist [22, 91, 92]. In the present work we fixed a filtration parameter to generate point clouds and then studied the one-parameter family of alpha complexes of different radii. Actually, this forms a natural surrounding for a two-parameter filtration of complexes. Can corresponding weak invariants such as the rank invariant [22] be employed meaningfully in the given setting?

With the present work we believe to have found a promising machinery to understand emergent homological structures far from equilibrium beyond the language of correlation functions. Certainly, this work only provides a very first step on the route of introducing persistent homology observables to QFT. Where does the interplay between these novel geometric methods and quantum physics lead to?

Acknowledgments

Appendices

Appendix A

Numerical convergence of persistent homology observables

In this appendix we provide results for how the different persistent homology observables of interest in the main text converge with the number of classical-statistical samples, n, increasing. We noted in Sec. 6.3 that depending on the filtration parameter $\bar{\nu}$ birth and death radii distributions converge differently fast with n. Confirming this observation, in Fig. A.1 we display birth and death radii distributions as well as persistence distributions for two values of $\bar{\nu}$, at different times within the persistent homology observables' self-similar scaling regime and for different values of n. It is clearly visible that occurring fluctuations decrease with n increasing.

In Fig. A.2 we display Betti numbers. In particular, $\bar{\beta}_0$ converged very well for $n = 50$. $\bar{\beta}_1$ converges later with the number of samples taken into account, since distributions are computed from fewer persistent homology classes with corresponding properties. Yet, additional samples do not alter the overall shape of $\bar{\beta}_1$ anymore, solely reducing occurring statistical fluctuations.

As observed in Sec. 6.5, the average maximum death radius, $\bar{r}_{d,\max}$, is a quantity that is very sensitive to particular geometric arrangements of points in analyzed point clouds. Resembling this effect, in Fig. A.3 we display $\bar{r}_{d,\max}$ for different n. Clearly, occurring oscillations drastically reduce with n increasing. Regions of approximate power-law behavior certainly converged properly for $n = 50$ as studied in the main text.

To sum up, different persistent homology observables converge differently fast with the number of classical-statistical samples, n, taken into account in averaging. Corresponding differences among their convergence behavior can be easily understood geometrically.
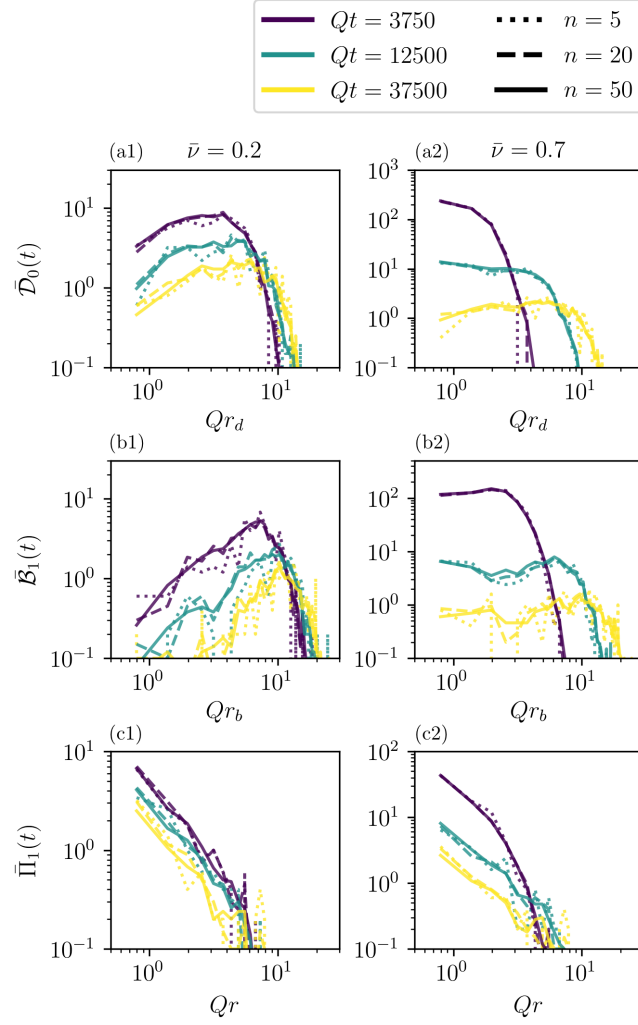
Figure A.1: Birth and death radii distributions and persistence distributions in the infrared varying with time, displayed for $\bar{\nu}$-values and numbers of classical-statistical samples to average, n, as indicated.
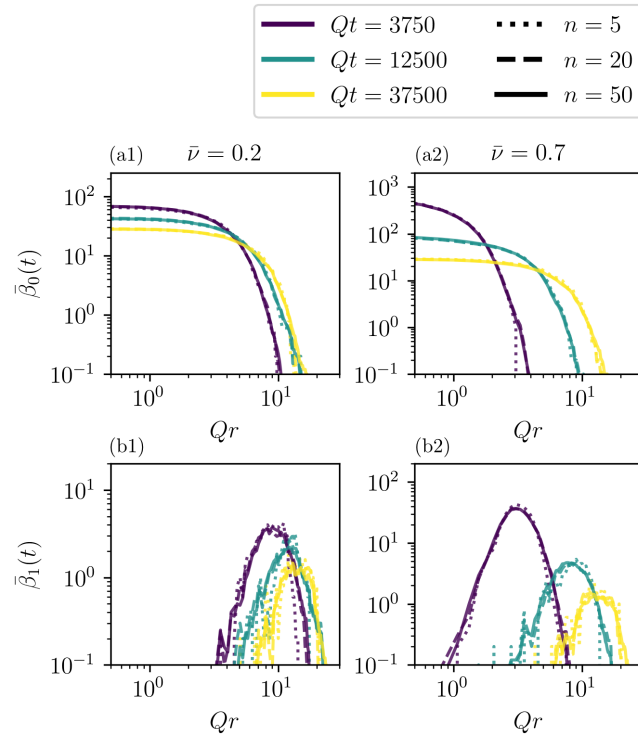
Figure A.2: Betti number distributions in the infrared varying with time, displayed for $\bar{\nu}$-values and numbers of classical-statistical samples to average, n, as indicated.
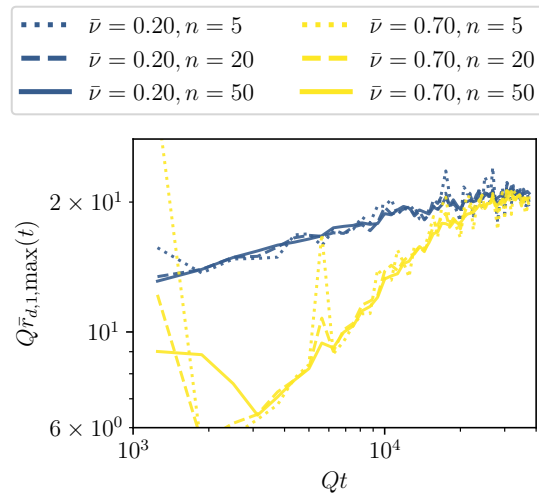

Figure A.3: The average maximum death radius of 1-dimensional persistent homology classes varying with time, displayed for $\bar{\nu}$-values and numbers of classical-statistical samples to average, n, as indicated.

Appendix B

Extracting scaling exponents

This appendix introduces extraction protocols for self-similar scaling exponents in a twofold fashion. In Sec. B.1 we provide the procedure for correlation functions, in Sec. B.2 we provide a similar procedure for persistent homology observables, making use of both of them in the numerics carried out in the course of the present work.

B.1   Scaling exponents from correlation functions

In Sec. 6.2 we studied the self-similar evolution of the occupation number spectrum $f(t, \mathbf{p})$, that is, of a particular type of two-point correlation function. Central to this analysis is the extraction of correlation function scaling exponents. Our procedure is the same as the one used in Ref. [4]. We cite the most important aspects of it here.

First, the occupation number spectrum $f(t, \mathbf{p})$ is rescaled according to the self-similar scaling ansatz,

$$f_{\mathrm{resc}}(t, \mathbf{p}) = (t/t')^{-\alpha} f(t, (t/t')^{-\beta}\mathbf{p}). \tag{B.1}$$

The occupation number spectrum at N_{com} times within the self-similar scaling regime is compared to an earliest reference time t', chosen to be the time at which the self-similar scaling evolution begins, approximately. We quantify deviations from a perfect rescaling by means of

$$\Delta f(t, \mathbf{p}) = f_{\mathrm{resc}}(t, \mathbf{p}) - f(t', \mathbf{p}), \tag{B.2}$$

$$\chi^2(\alpha, \beta) = \frac{1}{N_{\mathrm{com}}} \sum_{k=1}^{N_{\mathrm{com}}} \frac{\int d(\log(\mathbf{p}))(\Delta f(t_k, \mathbf{p})/f(t', \mathbf{p}))^2}{\int d(\log(\mathbf{p}))}, \tag{B.3}$$

borrowing notation from Ref. [4].

$\chi^2(\alpha, \beta)$ is minimized for the best-fitting pair of exponents $(\bar{\alpha}, \bar{\beta})$. We define a likeli-

hood function by means of

$$W(\alpha, \beta) = \frac{1}{\mathcal{N}} \exp\left(-\frac{\chi^2(\alpha, \beta)}{2\chi^2(\bar{\alpha}, \bar{\beta})}\right), \tag{B.4}$$

$\mathcal{N}$ being a normalization constant defined by $\int d\alpha \, d\beta \, W = 1$. Fitting marginal likelihood functions such as $W(\alpha) = \int d\beta \, W(\alpha, \beta)$ with Gaussian distributions, we estimate standard deviations such as σ_α for the best-fitting pair of scaling exponents. The final pair of extracted scaling exponents is given by

$$\alpha = \bar{\alpha} \pm \sigma_\alpha, \qquad \beta = \bar{\beta} \pm \sigma_\beta. \tag{B.5}$$

B.2 Scaling exponents from persistent homology

Key to the analysis of results in our nonrelativistic Bose gas testbed in Chap. 6 is the extraction of persistent homology scaling exponents from approximately self-similar birth and death radii distributions. This appendix serves as a description of the applied protocol to accomplish this task, similar in spirit to the protocol employed to extract correlation function scaling exponents.

We first define rescaled variants of the birth and death radii distributions,

$$\bar{\mathcal{B}}_\ell^{\mathrm{resc}}(t, r_b) = (t/t')^{\eta_2 - \eta_1'} \bar{\mathcal{B}}_\ell(t, (t/t')^{-\eta_1} r_b), \tag{B.6a}$$

$$\bar{\mathcal{D}}_\ell^{\mathrm{resc}}(t, r_d) = (t/t')^{\eta_2 - \eta_1} \bar{\mathcal{D}}_\ell(t, (t/t')^{-\eta_1'} r_d). \tag{B.6b}$$

Distributions at later times are compared with those at the reference time t', chosen to be the time at which the self-similar evolution sets in. However, we could equally well have chosen any other reference time within the self-similar scaling regime. Denote by $t_k > t'$, $k = 1, \ldots, N_{\mathrm{com}}$, all corresponding comparison times. If birth and death radii distributions were evolving perfectly self-similar according to Eqs. (5.6a) and (5.6b), we would find

$$\Delta\bar{\mathcal{B}}_\ell(t, r_b) = \bar{\mathcal{B}}_\ell^{\mathrm{resc}}(t, r_b) - \bar{\mathcal{B}}_\ell(t', r_b) = 0, \tag{B.7a}$$

$$\Delta\bar{\mathcal{D}}_\ell(t, r_d) = \bar{\mathcal{D}}_\ell^{\mathrm{resc}}(t, r_d) - \bar{\mathcal{D}}_\ell(t', r_d) = 0. \tag{B.7b}$$

Numerically, even for the correct triple of exponents $(\eta_1, \eta_1', \eta_2)$ this is only approximately true due to statistical uncertainties as well as systematic errors entering since systems typically only enter the vicinity of a nonthermal fixed point. We optimize scaling expo-

nents by means of minimizing occurring deviations, quantified by

$$\chi^2(\eta_1, \eta_1', \eta_2) = \chi_b^2(\eta_1, \eta_1', \eta_2) + \chi_d^2(\eta_1, \eta_1', \eta_2), \tag{B.8a}$$

$$\chi_b^2(\eta_1, \eta_1', \eta_2) = \frac{1}{N_{\text{com}}} \sum_{k=1}^{N_{\text{com}}} \frac{\int_{r_{\min}}^{r_{\max}} dr_b \, \Delta\bar{\mathcal{B}}_\ell(t_k, r_b)^2}{\int_{r_{\min}}^{r_{\max}} dr_b \, \bar{\mathcal{B}}_\ell(t', r_b)^2}, \tag{B.8b}$$

$$\chi_d^2(\eta_1, \eta_1', \eta_2) = \frac{1}{N_{\text{com}}} \sum_{k=1}^{N_{\text{com}}} \frac{\int_{r_{\min}}^{r_{\max}} dr_d \, \Delta\bar{\mathcal{D}}_\ell(t_k, r_d)^2}{\int_{r_{\min}}^{r_{\max}} dr_d \, \bar{\mathcal{D}}_\ell(t', r_d)^2}. \tag{B.8c}$$

Lower and upper limits of integration in the appearing expressions depend on whether the infrared or, for instance, the ultraviolet cascade is investigated, setting for the infrared cascade $Qr_{\min} = 1.5$ and $Qr_{\max} = 25.0$ for all $\bar{\nu} \leq 0.7$ and $Qr_{\min} = 1.0$ and $Qr_{\max} = 10.0$ for $\bar{\nu} = 0.8$. A priori, the given expressions for $\chi_{b/d}^2(\eta_1, \eta_1', \eta_2)$, are equally sensitive to the behavior at all scales of radii, increasing the weight of data points whose deviations are large. Linear interpolations are employed to obtain birth and death radii distributions at rescaled birth and death radii, respectively.

Minimizing deviations as measured by $\chi^2(\eta_1, \eta_1', \eta_2)$, the optimal triple $(\tilde{\eta}_1, \tilde{\eta}_1', \tilde{\eta}_2)$ is obtained. Analogously to Refs. [3,4], a likelihood function is defined as

$$W(\eta_1, \eta_1', \eta_2) = \frac{1}{\mathcal{N}} \exp\left(-\frac{\chi^2(\eta_1, \eta_1', \eta_2)}{2\chi^2(\tilde{\eta}_1, \tilde{\eta}_1', \tilde{\eta}_2)} \right), \tag{B.9}$$

$\mathcal{N}$ being a normalization constant such that

$$\int d\eta_1 \, d\eta_1' \, d\eta_2 \, W(\eta_1, \eta_1', \eta_2) = 1. \tag{B.10}$$

Marginal likelihood functions are obtained upon integrating over two of the exponents, for instance,

$$W(\eta_1) = \int d\eta_1' \, d\eta_2 \, W(\eta_1, \eta_1', \eta_2). \tag{B.11}$$

We fit marginal likelihood functions with Gaussian distributions to estimate corresponding standard deviations, $\sigma_{\eta_1}, \sigma_{\eta_1'}$ and σ_{η_2}, the means still being given by $\tilde{\eta}_1, \tilde{\eta}_1'$ and $\tilde{\eta}_2$.

To derive time-dependent persistent homology scaling exponents, we apply the described fitting procedure with a fixed reference time Qt' for $N_{\text{com}} = 3$ times, simultaneously: $Qt_{\min}$ as indicated in the main text as well as $Qt_{\min} + 625$ and $Qt_{\min} + 1250$. Repeating this procedure for different $Qt_{\min}$, we obtain time-dependent scaling exponents.

Bibliography

[1] N. Wolchover, "The universal law that aims time's arrow," *Quanta Magazine*, August 2019.

[2] J. Berges, "Nonequilibrium Quantum Fields: From Cold Atoms to Cosmology," 2015.

[3] J. Berges, K. Boguslavski, S. Schlichting, and R. Venugopalan, "Universal attractor in a highly occupied non-abelian plasma," *Phys. Rev. D*, vol. 89, p. 114007, Jun 2014.

[4] A. Piñeiro Orioli, K. Boguslavski, and J. Berges, "Universal self-similar dynamics of relativistic and nonrelativistic field theories near nonthermal fixed points," *Phys. Rev.*, vol. D92, no. 2, p. 025041, 2015.

[5] J. Berges, K. Boguslavski, S. Schlichting, and R. Venugopalan, "Universality far from equilibrium: From superfluid Bose gases to heavy-ion collisions," *Phys. Rev. Lett.*, vol. 114, no. 6, p. 061601, 2015.

[6] J. Berges, K. Boguslavski, S. Schlichting, and R. Venugopalan, "Nonequilibrium fixed points in longitudinally expanding scalar theories: Infrared cascade, bose condensation, and a challenge for kinetic theory," *Phys. Rev. D*, vol. 92, p. 096006, Nov 2015.

[7] R. Micha and I. I. Tkachev, "Turbulent thermalization," *Phys. Rev. D*, vol. 70, p. 043538, Aug 2004.

[8] J. Berges and D. Sexty, "Strong versus weak wave-turbulence in relativistic field theory," *Phys. Rev.*, vol. D83, p. 085004, 2011.

[9] J. Berges, K. Boguslavski, S. Schlichting, and R. Venugopalan, "Turbulent thermalization process in heavy-ion collisions at ultrarelativistic energies," *Phys. Rev. D*, vol. 89, p. 074011, Apr 2014.

[10] J. Berges and D. Sexty, "Bose-einstein condensation in relativistic field theories far from equilibrium," *Phys. Rev. Lett.*, vol. 108, p. 161601, Apr 2012.

[11] R. Micha and I. I. Tkachev, "Relativistic turbulence: A long way from preheating to equilibrium," *Phys. Rev. Lett.*, vol. 90, p. 121301, Mar 2003.

[12] K. Boguslavski and A. Piñeiro Orioli, "Unraveling the nature of universal dynamics in $O(N)$ theories," 2019.

[13] M. Prüfer, P. Kunkel, H. Strobel, S. Lannig, D. Linnemann, C.-M. Schmied, J. Berges, T. Gasenzer, and M. K. Oberthaler, "Observation of universal dynamics in a spinor Bose gas far from equilibrium," *Nature*, vol. 563, no. 7730, pp. 217–220, 2018.

[14] S. Erne, R. Bücker, T. Gasenzer, J. Berges, and J. Schmiedmayer, "Universal dynamics in an isolated one-dimensional Bose gas far from equilibrium," *Nature*, vol. 563, no. 7730, pp. 225–229, 2018.

[15] M. Prüfer, T. V. Zache, P. Kunkel, S. Lannig, A. Bonnin, H. Strobel, J. Berges, and M. K. Oberthaler, "Experimental extraction of the quantum effective action for a non-equilibrium many-body system," 2019.

[16] A. Piñeiro Orioli and J. Berges, "Breaking the fluctuation-dissipation relation by universal transport processes," *Phys. Rev. Lett.*, vol. 122, no. 15, p. 150401, 2019.

[17] J. Berges, M. Mace, and S. Schlichting, "Universal self-similar scaling of spatial Wilson loops out of equilibrium," *Phys. Rev. Lett.*, vol. 118, no. 19, p. 192005, 2017.

[18] T. Schweigler, V. Kasper, S. Erne, I. Mazets, B. Rauer, F. Cataldini, T. Langen, T. Gasenzer, J. Berges, and J. Schmiedmayer, "Experimental characterization of a quantum many-body system via higher-order correlations," *Nature*, vol. 545, no. 7654, p. 323, 2017.

[19] D. Spitz and J. Berges, "Schwinger pair production and string breaking in non-abelian gauge theory from real-time lattice improved hamiltonians," *Phys. Rev. D*, vol. 99, p. 036020, Feb 2019.

[20] T. V. Zache, T. Schweigler, S. Erne, J. Schmiedmayer, and J. Berges, "Extracting the field theory description of a quantum many-body system from experimental data," 2019.

[21] J. Berges, K. Boguslavski, M. Mace, and J. M. Pawlowski, "Gauge-invariant condensation in the nonequilibrium quark-gluon plasma," 2019.

[22] G. Carlsson, "Topology and data," *Bulletin of the American Mathematical Society*, vol. 46, no. 2, pp. 255–308, 2009.

[23] N. Otter, M. A. Porter, U. Tillmann, P. Grindrod, and H. A. Harrington, "A roadmap for the computation of persistent homology," *EPJ Data Science*, vol. 6, no. 1, p. 17, 2017.

[24] J. Munkres, *Elements of algebraic topology.* Advanced book program, Addison-Wesley, 1984.

[25] H. Edelsbrunner, D. Letscher, and A. Zomorodian, "Topological persistence and simplification," in *Proceedings 41st Annual Symposium on Foundations of Computer Science*, pp. 454–463, IEEE, 2000.

[26] A. Zomorodian and G. Carlsson, "Computing persistent homology," *Discrete & Computational Geometry*, vol. 33, pp. 249–274, Feb 2005.

[27] H. Edelsbrunner and J. Harer, *Computational topology : an introduction.* American Mathematical Society, 2010.

[28] H. Edelsbrunner, *Weighted alpha shapes*, vol. 92. University of Illinois at Urbana-Champaign, Department of Computer Science, 1992.

[29] H. Edelsbrunner and E. P. Mücke, "Three-dimensional alpha shapes," *ACM Transactions on Graphics (TOG)*, vol. 13, no. 1, pp. 43–72, 1994.

[30] T. Sousbie, "The persistent cosmic web and its filamentary structure–i. theory and implementation," *Monthly Notices of the Royal Astronomical Society*, vol. 414, no. 1, pp. 350–383, 2011.

[31] R. Van de Weygaert, G. Vegter, H. Edelsbrunner, B. J. Jones, P. Pranav, C. Park, W. A. Hellwing, B. Eldering, N. Kruithof, E. Bos, *et al.*, "Alpha, betti and the megaparsec universe: on the topology of the cosmic web," in *Transactions on computational science XIV*, pp. 60–101, Springer-Verlag, 2011.

[32] P. Pranav, H. Edelsbrunner, R. Van de Weygaert, G. Vegter, M. Kerber, B. J. Jones, and M. Wintraecken, "The topology of the cosmic web in terms of persistent betti numbers," *Monthly Notices of the Royal Astronomical Society*, vol. 465, no. 4, pp. 4281–4310, 2016.

[33] P. Pranav, R. J. Adler, T. Buchert, H. Edelsbrunner, B. J. Jones, A. Schwartzman, H. Wagner, and R. Van de Weygaert, "Unexpected topology of the temperature fluctuations in the cosmic microwave background," *Astronomy & Astrophysics*, vol. 627, p. A163, 2019.

[34] L. Duponchel, "Exploring hyperspectral imaging data sets with topological data analysis," *Analytica Chimica Acta*, vol. 1000, pp. 123 – 131, 2018.

[35] T. Nakamura, Y. Hiraoka, A. Hirata, E. G. Escolar, and Y. Nishiura, "Persistent homology and many-body atomic structure for medium-range order in the glass," *Nanotechnology*, vol. 26, p. 304001, jul 2015.

[36] R. Dridi and H. Alghassi, "Homology computation of large point clouds using quantum annealing," *arXiv preprint arXiv:1512.09328*, 2015.

[37] S. Lloyd, S. Garnerone, and P. Zanardi, "Quantum algorithms for topological and geometric analysis of data," *Nature communications*, vol. 7, p. 10138, 2016.

[38] H.-L. Huang, X.-L. Wang, P. P. Rohde, Y.-H. Luo, Y.-W. Zhao, C. Liu, L. Li, N.-L. Liu, C.-Y. Lu, and J.-W. Pan, "Demonstration of topological data analysis on a quantum processor," *Optica*, vol. 5, pp. 193–198, Feb 2018.

[39] J. J. Berwald, J. M. Gottlieb, and E. Munch, "Computing wasserstein distance for persistence diagrams on a quantum computer," *arXiv preprint arXiv:1809.06433*, 2018.

[40] S. Gunn and N. Kornerup, "Review of a quantum algorithm for betti numbers," *arXiv preprint arXiv:1906.07673*, 2019.

[41] L. Polterovich, "Inferring topology of quantum phase space," *Journal of Applied and Computational Topology*, vol. 2, pp. 61–82, Oct 2018.

[42] N. G. Berloff and B. V. Svistunov, "Scenario of strongly nonequilibrated bose-einstein condensation," *Phys. Rev. A*, vol. 66, p. 013603, Jul 2002.

[43] B. Nowak, J. Schole, D. Sexty, and T. Gasenzer, "Nonthermal fixed points, vortex statistics, and superfluid turbulence in an ultracold bose gas," *Phys. Rev. A*, vol. 85, p. 043627, Apr 2012.

[44] J. Schole, B. Nowak, and T. Gasenzer, "Critical dynamics of a two-dimensional superfluid near a nonthermal fixed point," *Phys. Rev. A*, vol. 86, p. 013624, Jul 2012.

[45] R. Walz, K. Boguslavski, and J. Berges, "Large-n kinetic theory for highly occupied systems," *Phys. Rev. D*, vol. 97, p. 116011, Jun 2018.

[46] M. Karl and T. Gasenzer, "Strongly anomalous non-thermal fixed point in a quenched two-dimensional Bose gas," *New J. Phys.*, vol. 19, no. 9, p. 093014, 2017.

[47] J. Deng, S. Schlichting, R. Venugopalan, and Q. Wang, "Off-equilibrium infrared structure of self-interacting scalar fields: Universal scaling, Vortex-antivortex superfluid dynamics and Bose-Einstein condensation," *Phys. Rev.*, vol. A97, no. 5, p. 053606, 2018.

[48] T. Simula, M. J. Davis, and K. Helmerson, "Emergence of order from turbulence in an isolated planar superfluid," *Phys. Rev. Lett.*, vol. 113, p. 165302, Oct 2014.

[49] A. J. Groszek, M. J. Davis, and T. P. Simula, "Decaying quantum turbulence in a two-dimensional Bose-Einstein condensate at finite temperature," *arXiv e-prints*, p. arXiv:1903.05528, Mar 2019.

[50] J. Berges, A. Rothkopf, and J. Schmidt, "Nonthermal fixed points: Effective weak coupling for strongly correlated systems far from equilibrium," *Phys. Rev. Lett.*, vol. 101, p. 041603, Jul 2008.

[51] J. Berges, K. Boguslavski, S. Schlichting, and R. Venugopalan, "Basin of attraction for turbulent thermalization and the range of validity of classical-statistical simulations," *JHEP*, vol. 05, p. 054, 2014.

[52] Z. Hadzibabic, P. Krüger, M. Cheneau, S. P. Rath, and J. Dalibard, "The trapped two-dimensional bose gas: from bose–einstein condensation to berezinskii–kosterlitz–thouless physics," *New Journal of Physics*, vol. 10, p. 045006, apr 2008.

[53] C. J. Pethick and H. Smith, *Bose–Einstein Condensation in Dilute Gases*. Cambridge University Press, 2 ed., 2008.

[54] D. T. Son, "Classical preheating and decoherence," 1996.

[55] G. Aarts and J. Berges, "Classical aspects of quantum fields far from equilibrium," *Phys. Rev. Lett.*, vol. 88, p. 041603, Jan 2002.

[56] A. Arrizabalaga, J. Smit, and A. Tranberg, "Tachyonic preheating using 2pi-1/n dynamics and the classical approximation," *Journal of High Energy Physics*, vol. 2004, pp. 017–017, oct 2004.

[57] J. Berges and T. Gasenzer, "Quantum versus classical statistical dynamics of an ultracold bose gas," *Phys. Rev. A*, vol. 76, p. 033604, Sep 2007.

[58] S. Y. Khlebnikov and I. I. Tkachev, "Classical decay of the inflaton," *Phys. Rev. Lett.*, vol. 77, pp. 219–222, Jul 1996.

[59] A. Schachner, A. Piñeiro Orioli, and J. Berges, "Universal scaling of unequal-time correlation functions in ultracold Bose gases far from equilibrium," *Phys. Rev.*, vol. A95, no. 5, p. 053605, 2017.

[60] B. Nowak, J. Schole, D. Sexty, and T. Gasenzer, "Nonthermal fixed points, vortex statistics, and superfluid turbulence in an ultracold Bose gas," *Phys. Rev.*, vol. A85, p. 043627, 2012.

[61] H. Edelsbrunner, A. Nikitenko, and M. Reitzner, "Expected sizes of poisson–delaunay mosaics and their discrete morse functions," *Advances in Applied Probability*, vol. 49, no. 3, p. 745–767, 2017.

[62] B. Delaunay, "Sur la sphere vide," *Bulletin of the Academy of Sciences of the USSR*, vol. 7, pp. 793–800, 1934.

[63] R. Forman, "Morse theory for cell complexes," *Advances in Mathematics*, vol. 134, no. 1, pp. 90 – 145, 1998.

[64] A. Hatcher, *Algebraic topology.* Cambridge: Cambridge Univ. Press, 2000.

[65] D. Cohen-Steiner, H. Edelsbrunner, and J. Harer, "Stability of persistence diagrams," *Discrete & Computational Geometry*, vol. 37, no. 1, pp. 103–120, 2007.

[66] D. Cohen-Steiner, H. Edelsbrunner, J. Harer, and Y. Mileyko, "Lipschitz functions have l p-stable persistence," *Foundations of computational mathematics*, vol. 10, no. 2, pp. 127–139, 2010.

[67] P. Bubenik, "Statistical topological data analysis using persistence landscapes," *The Journal of Machine Learning Research*, vol. 16, no. 1, pp. 77–102, 2015.

[68] E. Berry, Y.-C. Chen, J. Cisewski-Kehe, and B. T. Fasy, "Functional Summaries of Persistence Diagrams," *arXiv e-prints*, p. arXiv:1804.01618, Apr 2018.

[69] C. Maria, J.-D. Boissonnat, M. Glisse, and M. Yvinec, "The gudhi library: Simplicial complexes and persistent homology," in *Mathematical Software – ICMS 2014*, (Berlin, Heidelberg), pp. 167–174, Springer Berlin Heidelberg, 2014.

[70] J.-D. Boissonnat and C. Maria, "The simplex tree: An efficient data structure for general simplicial complexes," *Algorithmica*, vol. 70, pp. 406–427, Nov 2014.

[71] A. Fabri, G.-J. Giezeman, L. Kettner, S. Schirra, and S. Schönherr, "On the design of cgal a computational geometry algorithms library," *Software: Practice and Experience*, vol. 30, no. 11, pp. 1167–1202, 2000.

[72] H. Edelsbrunner, A. Nikitenko, K. Ölsböck, and P. Synak, "Radius functions on poisson–delaunay mosaics and related complexes experimentally," in *Proc. Abel Conference*, 2018.

[73] R. M. Soneira and P. J. E. Peebles, ""a computer model universe: simulation of the nature of the galaxy distribution in the lick catalog."," *Astronomical Journal*, vol. 83, pp. 845–860, Jul 1978.

[74] Y. Mileyko, S. Mukherjee, and J. Harer, "Probability measures on the space of persistence diagrams," *Inverse Problems*, vol. 27, p. 124007, Nov 2011.

[75] A. Bray, "Theory of phase-ordering kinetics," *Advances in Physics*, vol. 43, no. 3, pp. 357–459, 1994.

[76] J. Berges and G. Hoffmeister, "Nonthermal fixed points and the functional renormalization group," *Nucl. Phys.*, vol. B813, pp. 383–407, 2009.

[77] R. A. Dwyer, "Higher-dimensional voronoi diagrams in linear expected time," *Discrete & Computational Geometry*, vol. 6, pp. 343–367, Sep 1991.

[78] A. Dwyer, Rex, "The expected number of k-faces of a voronoi diagram," *Computes Math. Applic.*, vol. 26, no. 5, pp. 13–19, 1993.

[79] M. J. Golin and H.-S. Na, "On the average complexity of 3d-voronoi diagrams of random points on convex polytopes," *Comput. Geom. Theory Appl.*, vol. 25, pp. 197–231, July 2003.

[80] D. Attali and J.-D. Boissonnat, "A linear bound on the complexity of the delaunay triangulationof points on polyhedral surfaces," *Discrete & Computational Geometry*, vol. 31, pp. 369–384, Feb 2004.

[81] N. Amenta, D. Attali, and O. Devillers, "A tight bound for the delaunay triangulation of points on a polyhedron," *Discrete & Computational Geometry*, vol. 48, pp. 19–38, Jul 2012.

[82] D. Cohen-Steiner, H. Edelsbrunner, J. Harer, and Y. Mileyko, "Lipschitz functions have lp-stable persistence," *Foundations of Computational Mathematics*, vol. 10, pp. 127–139, Apr 2010.

[83] A. Mazeliauskas and J. Berges, "Prescaling and far-from-equilibrium hydrodynamics in the quark-gluon plasma," *Phys. Rev. Lett.*, vol. 122, no. 12, p. 122301, 2019.

[84] C.-M. Schmied, A. N. Mikheev, and T. Gasenzer, "Prescaling in a far-from-equilibrium Bose gas," *Phys. Rev. Lett.*, vol. 122, no. 17, p. 170404, 2019.

[85] J. Berges, K. Boguslavski, S. Schlichting, and R. Venugopalan, "Universality far from equilibrium: From superfluid bose gases to heavy-ion collisions," *Phys. Rev. Lett.*, vol. 114, p. 061601, Feb 2015.

[86] J. Baez, J. Muniain, and P. Javier, *Gauge Fields, Knots, and Gravity*. K & E series on knots and everything, World Scientific, 1994.

[87] F. Lenz, *Topological Concepts in Gauge Theories*, pp. 7–98. Berlin, Heidelberg: Springer Berlin Heidelberg, 2005.

[88] E. Witten, "Quantum field theory and the jones polynomial," *Comm. Math. Phys.*, vol. 121, no. 3, pp. 351–399, 1989.

[89] O. Bobrowski and M. Strom Borman, "Euler Integration of Gaussian Random Fields and Persistent Homology," *arXiv e-prints*, p. arXiv:1003.5175, Mar 2010.

[90] R. J. Adler, O. Bobrowski, M. S. Borman, E. Subag, and S. Weinberger, *Persistent homology for random fields and complexes*, vol. Volume 6 of *Collections*, pp. 124–143. Beachwood, Ohio, USA: Institute of Mathematical Statistics, 2010.

[91] F. Chazal, W. Crawley-Boevey, and V. de Silva, "The observable structure of persistence modules," *arXiv e-prints*, p. arXiv:1405.5644, May 2014.

[92] E. Miller, "Data structures for real multiparameter persistence modules," *arXiv e-prints*, p. arXiv:1709.08155, Sep 2017.

Erklärung zur Urheberschaft

Ich versichere, dass ich diese Arbeit selbstständig verfasst habe und keine anderen als die angegebenen Quellen und Hilfsmittel benutzt habe.

Heidelberg, den 3. Dezember 2019 . . . .